KU LEUVEN

ARENBERG DOCTORAL SCHOOL
Faculty of Engineering Science

Study of wind farm ABL interaction based on wind tunnel experiments

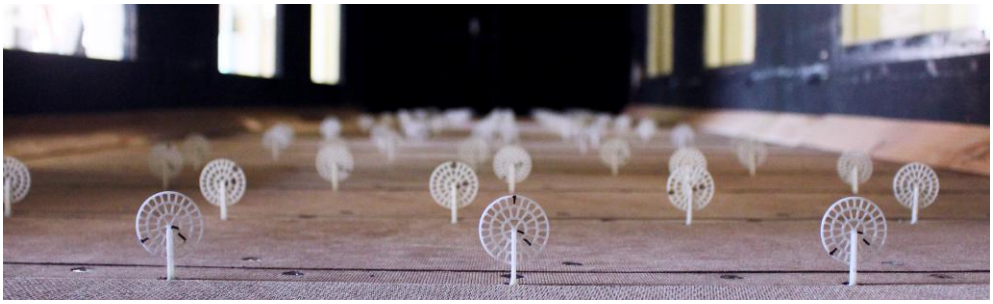

Juliaan Bossuyt

Supervisors:
Prof. dr. ir. Johan Meyers
Prof. dr. Charles Meneveau

Dissertation presented in partial fulfillment of the requirements for the degree of Doctor of Engineering Science (PhD): Mechanical Engineering

September 2017

Study of wind farm ABL interaction based on wind tunnel experiments

Juliaan BOSSUYT

Examination committee:
Prof. dr. ir. Omer Van der Biest, chair
Prof. dr. ir. Johan Meyers, supervisor
Prof. dr. Charles Meneveau, supervisor
Prof. dr. ir. Bert Blocken
Prof. dr. Maria Rosaria Vetrano
Prof. dr. Jeroen van Beeck
(von Karman Institute)
Prof. dr. Bharathram Ganapathisubramani
(University of Southampton)

Dissertation presented in partial fulfillment of the requirements for the degree of Doctor of Engineering Science (PhD): Mechanical Engineering

September 2017

© 2017 KU Leuven – Faculty of Engineering Science
Uitgegeven in eigen beheer, Juliaan Bossuyt, Celestijnenlaan 300 box 2402, B-3001 Leuven (Belgium)

Alle rechten voorbehouden. Niets uit deze uitgave mag worden vermenigvuldigd en/of openbaar gemaakt worden door middel van druk, fotokopie, microfilm, elektronisch of op welke andere wijze ook zonder voorafgaande schriftelijke toestemming van de uitgever.

All rights reserved. No part of the publication may be reproduced in any form by print, photoprint, microfilm, electronic or any other means without written permission from the publisher.

Preface

Four years ago, Johan offered me the opportunity to pursue a PhD. in his research group. The research project would include a three-year visit to Johns Hopkins University for wind tunnel experiments. Excited by the chance to immerse myself in the field of turbulence, wind energy, and wind tunnel experiments, and to visit a university in a different country, I decided to take on this challenge, even though I was also a little nervous to begin the journey. There were many ups and downs along the way, and of course a lot of hard work, but it turned out to be an incredibly rewarding experience, and, possibly, my best decision yet. None of this would have been possible without the help and support of many people.

I would like to express my sincere thanks to my advisors, Professors Johan Meyers and Charles Meneveau, for providing me the opportunity to pursue this PhD. Throughout my research, I could always count on their guidance and support. I appreciate the many insightful discussions, and their reasonable, honest, and critical opinions, which undoubtedly improved the quality of my work. It was an honor to work with these advisors who are both at the top of the field; I have learned a lot from them.

I would like to thank the examination committee for their careful analysis of my dissertation and for providing many interesting questions and comments. Their feedback contributed to the quality of this work.

When I arrived in Baltimore and started working in the Corrsin wind tunnel lab, Adrien taught me how to run the wind tunnel, how to perform hot-wire measurements, and taught me the complex and delicate process of soldering the hot-wire sensors. I learned a lot from Adrien and he became a very good friend.

I would also like to thank Mike who worked as an undergraduate student in the lab, and completed the elaborate job of manufacturing all one-hundred porous disk models. Mike's help with the experiments was greatly valued.

In Baltimore, I had the pleasure of gaining many great friends and colleagues. I would like to thank all members of Meneveau's turbulence research group for the many interesting group meetings and helpful discussions. Special thanks to Adrien, Carl, Zoe, Tony, Joel, Sean, Radhika, Richard, Michael, Claire, Adam, Dan, Michelle, Eshwan, Anna, Yan, Kenneth, Anouk, Nicolas, Ishmail and Perry for the lively discussions over lunch, the occasional frisbee break, happy-hour, MEGA-social, or weekend bike ride. Thanks also to Ted and Nicolas for the day-trips to Assateague, when I had to clear my mind and switch turbulence for waves. Ted, I also sincerely appreciate your help with Vray for Sketchup, which was useful for some of the visualizations of my measurement data.

In België kon ik rekenen op David, Ruben, Miet, Mathias, Emma, Jochen, Véronique, Sigmund, Silke, Christof, Elke, Jeroen, Judit, Thomas, Charlotte, Dries, Joliende, Andreas, Yens en Sébastien. Dank jullie wel voor de vaste afspraak telkens ik opnieuw in België was! Dank jullie ook Mathias, Ruben, Miet en Nelson om mij in Baltimore te bezoeken! Ik heb jullie bezoek erg gewaardeerd, het was leuk!

My thanks also to all members of the Turbulent Flow Simulation & Optimization group at KU Leuven for the many insightful technical discussions, and to everyone at TME for the daily chats and Alma-lunches. Thanks also to Wim, Thanos, Thomas, Vahid, Dries and Geert for the occasional break from work, with or without a beer.

I am grateful for the help I received from the staff at the Mechanical Engineering Department at KU Leuven and Johns Hopkins University. At KU Leuven I would like to thank especially Valérie, Carine, Regine and Marina for always being ready to help me with paperwork or reimbursements. At Johns Hopkins University I would like to thank Deana, Barb and Mike for helping me with paperwork or the many orders for the lab. Thanks also to Niel for his help with lab safety, 3D printing and the laser cutter.

I would like to thank Terri and Carly for always being interested and supportive of my work. Marcy, you inspire me everyday. Successfully completing this dissertation in the limited amount of time that was available would not have been possible without your support. Thank you so much for always supporting me in everything I do, and especially for being you.

Dit alles zou natuurlijk niet mogelijk geweest zijn zonder de steun van mijn ouders, Liesbeth De Vriese en Jan Bossuyt, en mijn zus, Siska. Dank jullie wel om altijd in mij te geloven en onvoorwaardelijk te steunen, ook al was dit soms aan de andere kant van de oceaan. Bedankt ook om mij tijdens dit doctoraat te bezoeken in Baltimore, het was zeer leuk om het daar eens allemaal aan jullie te tonen. Siska en Benjamin, ook heel erg bedankt om dit proefschrift in detail

te controleren op schrijffoutjes. Ik wil graag mijn familie bedanken, en in het bijzonder Denise, Francine en Paul, Sylvie en Joost, Sylvie en Rik, Anneke, Caroline en Bruno, Frederik, Felix, en alle neven en nichten voor de interesse en steun die jullie altijd getoond hebben.

Finally, I would like to thank the funding sources that supported the work for this dissertation: ERC (grant no. 306471, the ActiveWindFarms project) and NSF (grants CBET-113380 and OISE-1243482, the WINDINSPIRE project).

September 8, 2017

Juliaan Bossuyt

Abstract

As wind farms rapidly increase in size and quantity, a better understanding of their interaction with the atmospheric boundary layer, and its relation to farm efficiency, becomes important. High-fidelity simulations, such as Large Eddy Simulations, have not yet explored many different farm layouts because of the high computational-cost. Furthermore, modeling approaches need validation to quantify the effects of their approximations. Wind tunnel experiments in a highly controlled environment can provide detailed data for such validation studies. However, due to scaling difficulties, wind tunnel studies have been limited to smaller farms with 30 turbines or less, only a few layouts, and have mainly focused on flow measurements instead of power. The main goal of this dissertation is to provide experimental data of power from large wind farms and for many layouts.

In this dissertation we design a scaled wind tunnel model of a farm with one hundred turbine models, by using a porous disk approach. The models are designed to have a realistic thrust coefficient and far-wake properties. Each porous disk is instrumented with strain gages to measure the instantaneous thrust force. With momentum theory it is possible to deduce the spatially averaged incoming velocity and a surrogate for the power output from the force signals. The frequency response of these measurements reaches up to the structural natural frequency of the model or a reduced frequency of $fD/U \approx 0.6$, normalized by the local velocity and disk diameter.

The measurement capabilities of the experimental apparatus are verified by comparing with field and simulation results in the literature, and hot-wire measurements in the wind tunnel. It is concluded that within the measurement uncertainty, the setup can be used to study the main effects of wind farm layout on individual power outputs and the spatio-temporal correlation of the signals.

We perform a parametric study of wind farm power and unsteady loading, covering fifty-six layouts. Three layout-series are considered: layouts with a

uniform streamwise and spanwise spacing, layouts with a moderate uneven streamwise spacing, and layouts with an extreme uneven streamwise spacing. The largest improvements in power are observed for the entrance region of the farm, e.g. the first 10–15 rows, which is in agreement with results in the literature. For uniform spacing, the effect of layout on power at the end of the farm is negligible. However, for certain layouts with an uneven streamwise spacing, strong wake effects can reduce the power considerably over the entire farm. When staggered, the layout series with extreme uneven streamwise spacing shows the highest surrogate power output. It is concluded that strongly non-uniform layouts show potential for increasing the overall farm efficiency.

The unique spatio-temporal acquisition capabilities of the experimental setup is also used to study the spectrum of the surrogate power. The experimental results show that the frequency spectrum of the total wind farm power follows a power-law with a slope between $-5/3$ and -2, and up to lower frequencies than seen for any individual turbine model. In agreement with previous studies in the literature, peaks in the spectrum are observed at frequencies corresponding to the mean flow convection time between consecutive turbines. In the current work, we interpret the sum of power extraction from an array of turbines as a discrete spatial sampling of a turbulent boundary layer and derive the associated transfer function. We apply it to an existing model for the wavenumber–frequency spectrum of turbulent boundary layers. This approach allows us to verify the individual roles of Doppler shift and broadening of frequencies on the resulting spatially sampled frequency spectrum. Comparison with the wind tunnel data confirms that the approach captures and explains the main features in the spectrum, indicating the crucial role of the interaction between the spatial sampling and the space–time correlations inherently present in the flow. The frequency spectrum of the aggregated power from a wind farm thus depends on both the spectrum of the incoming turbulence and its modulation by the spatial distribution of turbines in the boundary layer flow.

Beknopte samenvatting

Het aantal en de grootte van windturbineparken neemt snel toe. Een betere kennis en begrip van de energie-wisseling met de atmosferische grenslaag, en het effect op het rendement van het turbinepark, wordt daarom alsmaar belangrijker. Waarheidsgetrouwe numerieke simulaties, zoals Large Eddy Simulaties (NL: *simulaties van grote wervelingen*), hebben een hoge rekenkost, waardoor parametrische studies van vele verschillende lay-outs beperkt zijn. Bovendien is het nodig om de inherente vereenvoudigingen in simulaties en modellen te valideren met experimentele metingen, zoals windtunnel experimenten in een gecontroleerde omgeving. Wegens het grote schaalverschil, en de daaruit volgende experimentele uitdagingen, hebben windtunnel experimenten tot nog toe enkel kleinere turbineparken bestudeerd, voor een klein aantal lay-outs, en meestal zonder metingen van het turbine vermogen. Het doel van dit doctoraat is om experimentele metingen beschikbaar te maken van grote windturbineparken, en voor vele verschillende lay-outs.

In dit proefschrift ontwerpen we een geschaald model van een windturbinepark met honderd turbines, door de turbines te modelleren met poreuze schijven. Deze statische modellen zijn ontworpen zodat ze een realistische weerstandscoëfficiënt hebben en een zog produceren dat in het ontwikkelde deel gelijkaardig is aan dat van een grootschalige windturbine. Elk model is geïnstrumenteerd met rekstrookjes om de tijdsafhankelijke kracht op de schijf te meten. Met deze meting is het mogelijk om de inkomende snelheid, gemiddeld over de schijf, en het overeenkomende turbine vermogen te reconstrueren. De frequentierespons van de metingen rijkt tot de eigenfrequentie van het model, wat overeenkomt met een gereduceerde frequentie van $fD/U \approx 0.6$, door te normaliseren met de inkomende snelheid en de diameter.

De meetmogelijkheden van de experimentele opstelling worden vergeleken met resultaten in de literatuur van Large Eddy Simulaties en meetcampagnes, alsook met hete-draad metingen in de windtunnel. Er wordt besloten dat binnen de meetnauwkeurigheid, de opstelling bruikbaar is om het effect van de lay-out op

het turbinevermogen en de ruimtelijke, en tijdsafhankelijke, correlaties tussen turbines te bestuderen.

Een parametrische studie van zessenvijftig verschillende turbinepark lay-outs wordt uitgevoerd in functie van het totaal vermogen en de wisselende belasting van de turbines. Er worden drie verschillende lay-out series beschouwd: lay-outs met een uniforme turbineafstand in de stroomzin en dwarsstroomzin, lay-outs met een wisselende tussenafstand in de stroomzin, en lay-outs met een extreem wisselende tussenafstand in de stroomzin. De grootste verbeteringen van het equivalent vermogen worden gemeten voor de eerste tien tot vijftien turbinerijen, in overeenkomst met bevindingen in de literatuur. Voor een uniforme turbineafstand is het effect van lay-out op het vermogen na vijftien turbinerijen bijna verwaarloosbaar. Maar voor sommige lay-outs met een wisselende turbineafstand zorgen sterke zogverliezen voor een lager vermogen over het volledige turbinepark. De lay-outs met een extreem wisselende tussenruimte in de stroomzin en waarvoor de rijen een versprongen profiel volgen, resulteren in het grootste totale vermogen. Er wordt besloten dat sterk onregelmatige lay-outs potentieel hebben om het rendement van windturbineparken te verhogen.

De unieke meet-mogelijkheid om het equivalent vermogen van elk model simultaan te meten wordt gebruikt om het spectrum van het totale parkvermogen te bestuderen. De metingen tonen aan dat het frequentiespectrum een machtsfunctie met een exponent tussen $-5/3$ en -2 volgt, tot lagere frequenties dan voor enig afzonderlijk model. In overeenkomst met observaties in de literatuur, wordt ook een piek op een frequentie gemeten die gerelateerd is aan de convectietijd tussen twee opeenvolgende turbinerijen. In dit werk interpreteren we de sommatie van turbinevermogens als een discrete bemonstering van de turbulente grenslaag en leiden we de overeenkomende overdrachtsfunctie af. We passen deze functie toe op een bestaand model voor de spatio-temporele structuur van een turbulente grenslaag om het frequentiespectrum van een turbinepark te berekenen. Deze techniek laat ons toe om de afzonderlijke invloeden van convectie en decorrelatie op het spectrum te bestuderen. Een vergelijking met de windtunnel experimenten toont aan dat het model de spectrale kenmerken kan schatten en verklaren, en dat de inherent aanwezige spatio-temporele correlatie van de grenslaag een belangrijke rol kan spelen in de compositie van het frequentiespectrum van het totale turbinepark vermogen.

Nomenclature

Acronyms

ABL	Atmospheric Boundary Layer
HIT	Homogeneous Isotropic Turbulence
LCOE	Levelized Cost Of Electricity
LES	Large Eddy Simulation
LIDAR	Laser Imaging Detection And Ranging
PIV	Particle Image Velocimetry
PSD	Power Spectral Density
TSR	Tip Speed Ratio

Greek symbols

β	porous disk solidity
$\Gamma(x)$	Gamma function
$\delta(x)$	Diracdelta function
Δ	lengthscale for the spatial filter in equation 2.12
Δ_y	spanwise shift for wind farm layout
δ_{99}	boundary layer height based on the location where the mean velocity is 99% of the free stream velocity
ϵ	turbulent dissipation
ζ	damping constant of a porous disk model
θ	momentum thickness of the boundary layer
κ	von Kármán constant, $\kappa \approx 0.4$
ρ	density of air
σ_u	standard deviation of the streamwise velocity component u
$\Phi_{11}(k_1, k_2, \omega)$	wavenumber-frequency spectral density, see equation 5.4
ω	angular velocity

Roman symbols

A	area
$A(k_r)$	spatial filter, see equation 2.12
a	induction coefficient
C_K	Kolmogorov constant, $C_K \approx 1.6$
C_P	power coefficient of a wind turbine
C_T	thurst coefficient of a wind turbine
D	wind turbine, or porous disk diameter
$e(k)$	energy spectrum function
$E(\mathbf{k}, \omega)$	wavenumber-frequency spectral density, see equation A.2
$E_\omega(\omega)$	frequency spectrum, see equation A.6
$E_k(\mathbf{k})$	wavenumber spectrum, see equation A.1
$E_{k\omega}(k_1, \omega)$	streamwise wavenumber - frequency spectrum, see equation A.7
$E_{kk}(k_1, k_2)$	horizontal wavenumber spectrum, see equation A.5
$E_{11}(k_1)$	streamwise wavenumber spectrum, see equation 2.10
F	force
f	frequency
f_n	natural frequency
$g(x, y)$	wind farm spatial sampling function
$H(x)$	Heaviside function
k_s	spring constant of a porous disk model
$\mathbf{k} = (k_1, k_2, k_3)$	wavevector of streamwise, spanwise and vertical wavenumbers
k	total wavenumber
k_r	radial wavenumber
L_u^x	integral length scale of the streamwise velocity in the streamwise direction
M	bending moment
N	number of turbines
N_R	number of rows in a wind farm layout
P_i	power output of wind turbine i, or surrogate power of porous disk i
P_{WF}	total power from a wind farm
$q(\mathbf{x})$	force distribution
r_{ij}	correlation between two signal
$R_{11}(\mathbf{r}, \tau)$	two-point and two-time velocity covariance tensor of the streamwise velocity
Re	reynolds number
St	strouhal number
S_x	streamwise spacing between wind turbines
S_y	spanwise spacing between wind turbines
t	time
TI	turbulence intensity

U_0	freestream velocity
U_d	local disk velocity, according to actuator disk theory
U_h	hub-height velocity
u_τ	friction velocity
$\mathbf{v}$	random sweeping velocity
x, y, z	streamwise, spanwise and vertical coordinate
z_0	surface roughness length

Miscellaneous symbols

$\langle \cdot \rangle$	spatial average
$\bar{\cdot}$	temporal average
$\widetilde{\cdot}$	spatially sampled
$\cdot^<$	low-pass filtered, or the low-frequency part of a signal
$\cdot^>$	high-pass filtered, or the high-frequency part of a signal

Contents

List of Figures

List of Tables

Chapter 1

Introduction

With a continuing increase in global electricity demand (IEA, 2016), and drastic efforts to limit global warming by reducing the exhaust of greenhouse gases (United Nations, 2015), a cheap and renewable energy technology, like wind power, is essential.

Today, horizontal axis wind turbines are the centerpiece of large scale wind energy technology. Modern offshore wind turbines have a rated power as large as 8 MW (e.g. the Siemens offshore direct drive SWT-8.0-154 wind turbine), and a significantly improved design and efficiency compared to the first large turbines. For example, the Smith-Putnam wind turbine was produced in 1941, and was the first with a megawatt-size capacity. However, with only 1100 hours of operation, it broke down in 1945 due to critical fatigue loading (Vestergaard et al., 2004). Presently, thousands of multiple-megawatt wind turbines operate in on- and offshore conditions with a lifetime in the order of twenty years. The up-scaling of turbine size and capacity and other technological advancements in recent decades have led to a significant decrease in the levelized cost of electricity (LCOE) from wind, and a cost competitiveness with conventional fossil-fuel based electricity (figure 1.1). Furthermore, also motivated by the need to limit our carbon footprint, the world-wide installed capacity of wind energy has increased rapidly (figure 1.2), reaching in 2016 a value of more than 496 GW. Due to the relative low power density of wind, such a high capacity has been realized, among others, through large projects in which many turbines are installed as a group to form wind farms. In Europe today, new offshore farms have an average capacity of more than 500 MW (WindEurope, 2016) and can extend up to lengths that are an order of magnitude larger than the height of the atmospheric boundary layer (ABL). For instance the boundary layer height

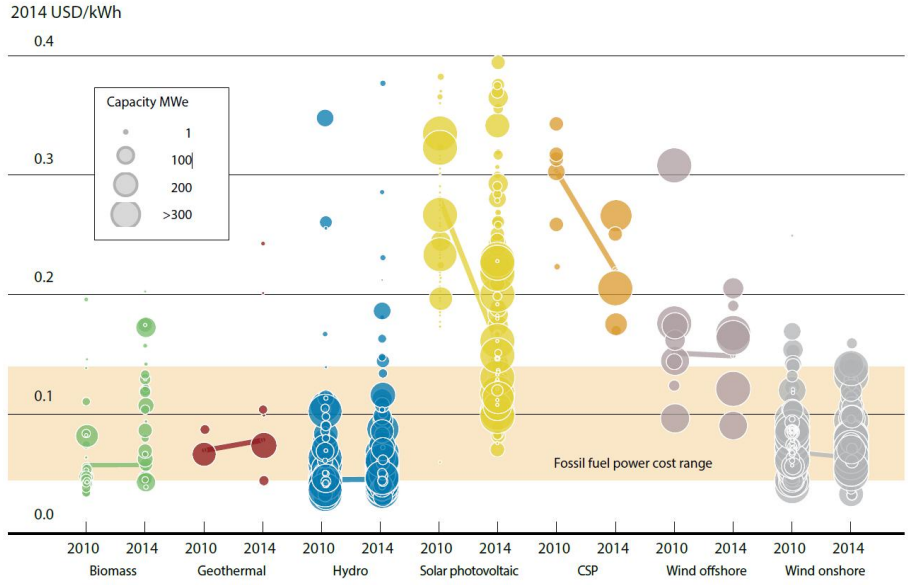

Figure 1.1: The levelised cost of electricity from utility-scale renewable technologies, in 2010 and 2014. The size of the circles represent the size of the project, and the center denotes the value of the cost. This figure is reproduced from IRENA (2015), Renewable power generation costs in 2014.

can vary from 500 m to several kilometers, while a wind farm with 15 rows can have a length of 10 km. The increase in farm size and capacity introduces new challenges, as the large-scale interaction with the ABL influences farm efficiency, and large amounts of an intermittent energy source are injected into the electricity grid. It is crucial to understand these new challenges to support further wind farm growth, and stimulate an additional decrease in the LCOE.

An essential aspect of wind energy is the flow interaction between wind turbines and the ABL. This complex and non-linear interplay is typically referred to as wind-farm boundary-layer interaction. Fog formation in the wakes of the turbines at the offshore Horns Rev wind farm in Denmark visualize this interaction in figure 1.3. As wind turbines extract energy from a turbulent flow, unsteady loading and power output variability are inevitable. These effects can reduce the turbine lifetime and make it difficult to forecast energy supply. Furthermore, as shown in figure 1.3, turbines produce a wake that is convected downstream and is characterized by a lower velocity and increased turbulence. Wakes reduce the potential available energy for a downstream turbine and increase the unsteady loading on the blades. While being advected downstream, wakes recover and

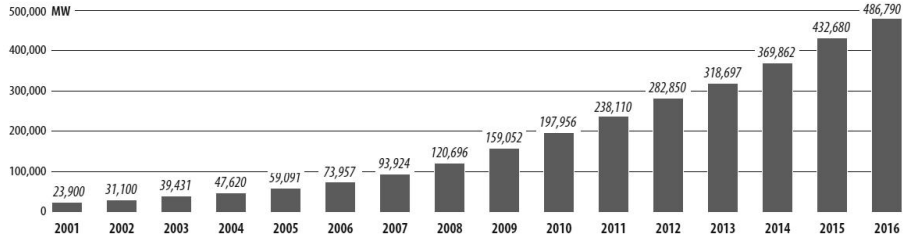

Figure 1.2: Global cumulative installed wind capacity 2001 - 2016. Figure is reproduced from GWEC, Global Wind Report - Annual market update 2016.

spread due to turbulent mixing and entrainment of high momentum fluid from the ambient flow. However, the spacing between wind turbines is typically not large enough for a complete wake recovery (Meyers and Meneveau, 2012). In a wind farm, wake losses can reduce turbine power with up to 50%, compared to a single lone-standing wind turbine (Hansen et al., 2012). Especially for large arrays, as indicated by the Horns Rev photograph, wakes can encompass the entire farm region, such that wake recovery is then driven mainly by vertical transport of mean kinetic energy from the high momentum flow above. In this fully developed regime, the vertical interaction with the boundary layer plays a key role in determining the turbine output, as the wind farm presents a large scale roughness to the flow (Calaf et al., 2010). While wake characteristics and recovery rate are highly dependent on ambient flow properties (Hansen et al., 2012), the boundary layer is on its turn influenced by the presence of the wind turbines. The wind farm ABL interaction thus contains a complex two-way coupling, which plays an important role in determining the overall farm efficiency.

The goal of this dissertation is to study the interaction between wind farms and the ABL experimentally in a controlled wind tunnel environment, focusing on farm efficiency, unsteady loading and the relation between the variable power outputs and turbulent characteristics of the boundary layer for very large wind farms. In the next section the scientific motivation for this work is elaborated based on a literature summary.

Figure 1.3: The turbulent wakes of wind turbines in the Horns Rev 1 wind farm are visualized by unique fog formation on February 12, 2008. The wind speed was near cut-in, such that most turbines produced only a low amount of power. The figure is reproduced from Hasager, C. B., Rasmussen, L., Peña, A., ensen, L. E. and Réthoré, P., "Wind Farm Wake: The Horns Rev Photo Case", Energies, 6(2):696-716, 2013.

1.1 Current insights in wind farm boundary layer interaction

Wind farm power output, and its connection to wind farm boundary layer interactions, can be studied with experiments and a broad spectrum of modeling approaches (see (Crespo et al., 1999; Sanderse et al., 2011; Vermeer et al., 2003; Mehta et al., 2014; Stevens and Meneveau, 2017) for an overview). Experiments provide data to improve our knowledge of governing physics and to validate models and theories. On the other hand, models are necessary for, among others, optimization and control purposes. Layout optimization studies have focused mainly on analytical models (Lackner and Elkinton, 2007; Chowdhury et al., 2012; Chen et al., 2013) that consider wake superposition (see e.g. the earliest approaches by Lissaman, 1979; Katic et al., 1986), as the low computational cost makes it possible to run thousands of cases. However, due to the simplified physics, the accuracy of these models is limited (Barthelmie et al., 2010; Walker et al., 2016), and case-specific tuning of the model parameters is required (Sorensen and Nielsen, 2006; Nygaard, 2014), such that it cannot be guaranteed that an optimal solution will be found in for instance an optimization study. Large Eddy Simulations (LES) can be found on the other end of the modeling

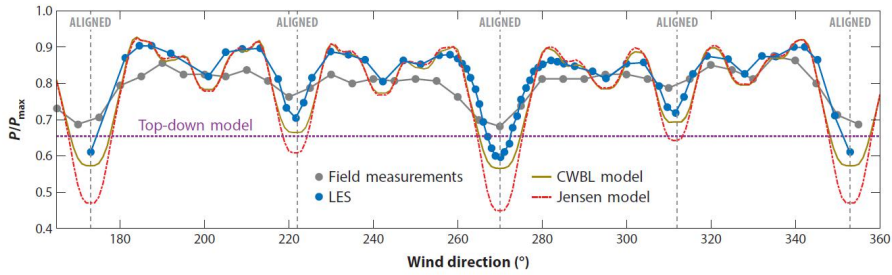

Figure 1.4: The normalized total power of the Horns Rev wind farm, as a function of wind direction, from field measurements (Pena et al., 2013), LES (Porté-Agel et al., 2013), and two engineering models (Stevens et al., 2016a). The power is normalized by the power of a non-wake-affected turbine times the number of turbines in the wind farm. Figure is reproduced from Stevens, R. J. A. M. and Meneveau, C., "Flow Structure and Turbulence in Wind Farms", Annual Review of Fluid Mechanics, 49:311-339, 2017.

spectrum. By solving the spatially-filtered Navier-Stokes equations to simulate the unsteady turbulent flow, LES is today one of the most detailed modeling approaches that is practical for studies of large wind farms. The higher fidelity of LES comes with a high computational cost, making LES impractical for layout-optimization or large parametric studies. Bokharaie et al. (2016) used therefore a hybrid Jensen-LES approach, by re-tuning the Jensen wake model on a regular basis with a LES simulation during the optimization process. However, also LES requires modeling assumptions; for instance, a subgrid-scale model to include the filtered turbulent stresses and simplified models to represent the wind turbine forces on relatively coarse grids (see e.g. Mikkelsen, 2003; Calaf et al., 2010 for the actuator disk approach or Shen and Sørensen, 2002; Martínez-Tossas et al., 2017 for the actuator line approach). Furthermore, LES results can be sensitive to specific numerics, as indicated by several studies that compared the detailed wake properties of a single turbine in laminar or boundary layer inflow conditions (Porté-Agel et al., 2011; Martínez-Tossas et al., 2015). Validation with experimental or field data is thus important to improve the accuracy of available modeling approaches.

Validation with field measurements of wind farms introduces several challenges. For instance, variable weather conditions result in large scale variations in wind direction, strength and thermal stratification, making it difficult to obtain converged statistics and requires averaging of measurements over a small sector of wind directions, e.g. ± 10 deg, ± 5 deg or ± 2.5 deg. As indicated by Barthelmie et al. (2011), the width of this sector can significantly influence the estimated row power. Furthermore, wind farms are operated commercially, such that the

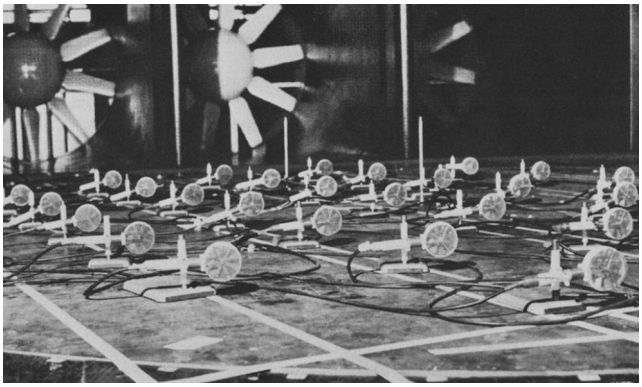

Figure 1.5: An experimental study of a wind farm in a wind tunnel, figure reproduced from Milborrow, D.J., "The performance of arrays of wind turbines", Journal of Wind Engineering and Industrial Aerodynamics, 5(3-4):403-430, 1980.

amount of available data from operating wind farms is relatively limited (see Stevens and Meneveau, 2017 for a recent overview of published data). Due to the occasional downtime of turbines, and the limited flow measurements by one or more measurement masts (Dahlberg, 2009; Barthelmie et al., 2011; Nygaard, 2014; Gaumond et al., 2014), clean comparisons with field experiments are challenging. Figure 1.4 shows a recent comparison of field measurements from the Horns Rev wind farm with LES and two engineering models. While all results predict similar trends, there is a clear mismatch with the field data, which follows more moderate changes of the power as a function of wind direction. This difference indicates the effect of atmospheric variability and the lack of detailed flow measurements of the inflow conditions, next to modeling differences.

The need for validation with well defined cases has motivated experimental studies in a controlled wind tunnel environment. For an overview of wind tunnel experiments of the performance and wake properties of a single turbine, see Vermeer et al. (2003), and more recently, e.g. the detailed wake measurements by Chamorro and Porté-Agel (2010); Krogstad and Adaramola (2012); Zhang et al. (2012); Lignarolo et al. (2016). Wind tunnel studies of large wind farms, on the other hand, are more limited because of the challenges related to fitting many small turbine models in a wind tunnel. Milborrow (1980) performed pioneering experiments of a turbine array by using a set of anemometers, see figure 1.5. As it can be seen from this figure, significant interactions of the supports may be expected. More recently, Corten et al. (2004) designed a scaled, two-bladed, turbine model with a diameter of 0.25 m and a specially designed blade geometry, to reach a better agreement with the performance of a full-scale

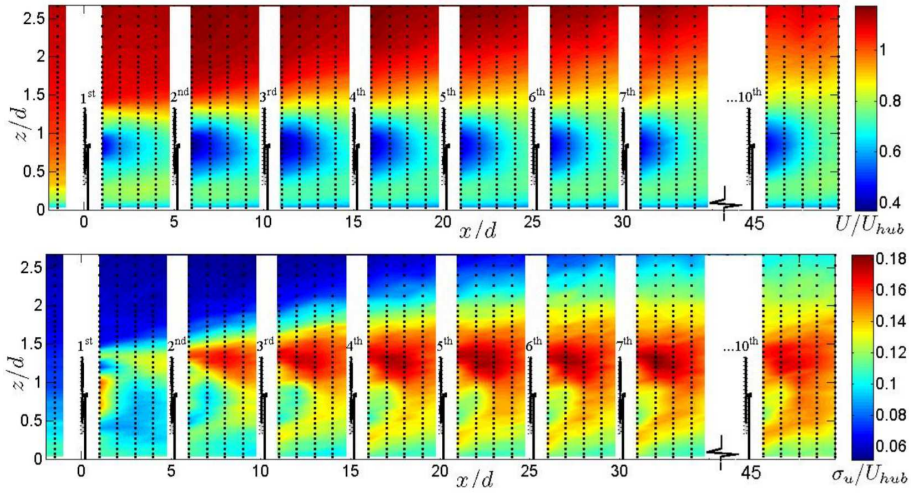

Figure 1.6: Hot-wire measurements of the flow in an aligned wind farm with $S_x/D = 5$. The wakes are visualized by the non-dimensional distribution of the mean velocity (Top) and the streamwise turbulence intensity $TI = \sigma_u/U_{hub}$ (bottom). Figure is reproduced from Chamorro, L. P. and Porté-Agel, "Turbulent Flow Inside and Above a Wind Farm: A Wind-Tunnel Study", Energies, 4(11):1916, 2011.

wind turbine. The measured optimum power coefficient was $C_P = 0.3$, in comparison to a value of $C_P = 0.45..0.5$ for a typical full-scale commercial wind turbine. The power was measured for an array of 28 scaled models, configured in a 14×2 aligned or 9×3 staggered configuration. However, due to the challenges of using scaled models for representative power measurements (see section 1.2 for a detailed discussion) wind farm studies have mainly focused on detailed measurements of the velocity field and its statistics. Hot-wire measurements were performed for a wind farm with 30 scaled wind turbines and 10 rows in an aligned (Chamorro and Porté-Agel, 2011) and staggered (Chamorro et al., 2011) configuration (see figure 1.6). However, more recent offshore farm designs (Nygaard, 2014) and optimization studies (Du Pont and Cagan, 2012; Bokharaie et al., 2016; Pillai et al., 2017) are exploring irregular layouts to improve the power output. Wind tunnel data for such layouts and for large farms are missing.

The study of wind farm power output and its relation to layout has therefore relied mostly on engineering models and LES studies (see Stevens and Meneveau, 2017 for a recent overview). Archer et al. (2013) studied five layout variations of the Lillgrund wind farm with LES and found the best results for a staggered

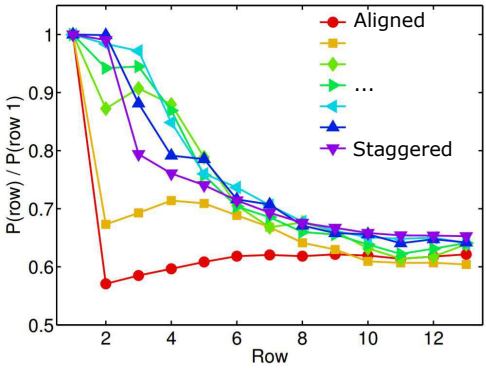

Figure 1.7: LES results for the mean row power of a wind farm with 13 rows. A variety of layouts are considered by changing the alignment of the wind turbine rows with the wind direction, from an aligned to a staggered configuration. The wind turbine spacing is $S_x/D = 7.85$ and $S_y/D = 5.23$. Figure is reproduced from Stevens, R. J. A. M., Gayme, D. and Meneveau, C., "Effect of turbine alignment on the average power output of wind-farms", J. Renewable and Sustainable Energy, 6(2):023105, 2014.

layout. These observations are in agreement with the wind tunnel results by Chamorro and Porté-Agel (2011); Chamorro et al. (2011). These experiments highlighted the effect of layout on flow properties, by showing lower turbulence levels and a slower development of an internal boundary and equilibrium layer for the staggered layout. Porté-Agel et al. (2013) performed LES of the Horns Rev wind farm, with 80 turbines in a slightly skewed grid layout for 67 different wind angles (see figure 1.4), and more recently, Munters et al. (2016b) applied an inflow with a time varying wind direction to a LES of the Horns Rev wind farm. Allaerts and Meyers (2017) studied a LES of 180 turbines placed in an aligned grid, and in a conventionally neutral boundary layer. Stevens et al. (2014); Stevens and Meneveau (2014); Stevens et al. (2016b) also performed LES for a series of wind farm layouts configured in an aligned or staggered array, with different wind turbine densities, and for different intermediate alignment angles with the wind direction. Yet, published LES data for irregular, non-homogeneous, or optimized layouts are still sparse.

Field measurements (Barthelmie et al., 2011) and LES studies (e.g. see figure 1.7 for results by Stevens et al., 2014) indicate that changing the layout can increase the power in the first rows of a wind farm significantly. For instance, (Stevens et al., 2014) found an increase of 25% in the average power of the first six rows by using a staggered compared to an aligned layout, and an increase

of more than 30% for an intermediate alignment angle. However, as shown in figure 1.7, the improvement in power after ten rows is significantly smaller, or even negligible for a small spanwise spacing (e.g. $S_y/D = 3.49$ in their study). As the mean row power reaches a constant value after approximately ten rows, the approach of a fully developed regime is indicated. In the fully developed wind farm regime, a balance takes place between wake recovery, mostly driven by vertical transfer of mean kinetic energy, and the power extracted by the wind turbines (Calaf et al., 2010). Interestingly, the influence of layout on power output in this regime is significantly smaller, and less obvious. Due to the limited size of wind farms in wind tunnel studies, experimental data for this regime is lacking, while data from LES has only focused on a small number of regular grid layout patterns.

1.2 Experiments of wind farms

Experimental studies can provide observations to support our understanding of the physical mechanisms and furthermore provide data to validate analytical or numerical models. These objectives have motivated efforts for wake measurements since the early days of wind energy research (Muraca and Guillotte, 1976; Vermeulen, 1978; Milborrow, 1980). Figure 1.5 shows an example of one of those early experiments. As with many applications, field measurements of full-scale wind turbines are not always practical and can be very expensive. The unsteady characteristics of the atmospheric boundary layer over many different time scales, such as large scale changes of wind direction or wind speed, make it difficult to obtain converged statistics during measurements. Furthermore, modern wind turbines can have a height of more than 200 m, which complicates the measurements of wakes. Very high measurement masts are necessary, which can only provide measurements at one location. Recent developments of Laser Imaging Detection And Ranging (LIDAR) technology are revolutionizing the measurement capabilities in wind farms (Banta et al., 2015; Herges et al., 2017; Fleming et al., 2017a). However, even LIDAR technology has its limitations, as it is still subject to ABL variability, and only measures the line of sight velocity along the LIDAR beam, spatially averaged over a volume. Alternatively, researchers have focused on wind tunnel experiments of scaled models to study wind turbines and wind farms under highly controllable conditions with precise measurement techniques such as hot-wire anemometry and Particle Image Velocimetry (PIV).

Performing wind tunnel experiments also introduces a number of challenges. It is of main importance that the scaled experiment contains the main flow-mechanisms that dominate the full-scale situation, which is also referred to as

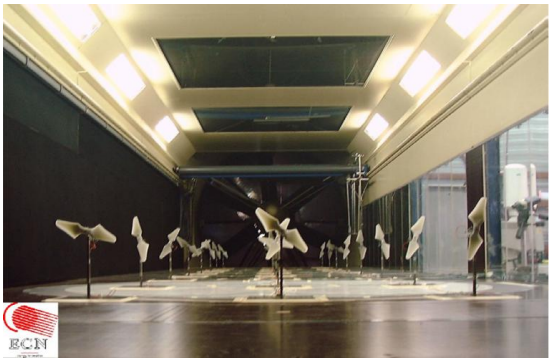

Figure 1.8: An experimental study of a 8×3 wind farm on a scale of $1:400$ in a wind tunnel. Figure reproduced from Corten G. P., Schaak, P. and Hegberg, T., "Turbine interaction in large offshore wind farms: Wind tunnel measurements", ECN-C-04-048, technical report, 2004.

flow similarity. Geometric similarity requires that all dimensions are scaled linearly with the scaling constant, e.g. $1:1000$ corresponds to a model which is scaled 1000 times smaller. Another important criterion is the balance of inertial to viscous forces, as denoted by the Reynolds number.

The Reynolds number associated with turbulence in the ABL at a height of 100 m is $Re \approx 10^8$. Wind farms thus operate in a highly turbulent atmospheric boundary layer which should be scaled correctly in a wind tunnel experiment. Atmospheric boundary layers are subject to the interaction with skin friction, buoyancy forces, Coriolis forces and e.g. effects from complex topographies. Thermal stratification can have a significant impact on the turbulent structure of a boundary layer or the wake of a turbine, as shown by Chamorro and Porté-Agel (2010); Zhang et al. (2013); Farr and Hancock (2014), through wind tunnel experiments in a neutral, stable and convective boundary layer. However, simulating thermal stratification in a wind tunnel requires precise temperature control, such that most studies focus on the neutral boundary layer for which the roughness effects dominate the turbulent structure. A neutral boundary layer is for instance relevant for offshore conditions with a strong wind and sufficient cloud cover. Modeling the Coriolis force correctly requires a rotating wind tunnel, and is typically not pursued for studies of wind farms. Based on a recent LES study, Allaerts and Meyers (2017) showed that wind veer from Coriolis forces can be in the order of 2 deg in a large wind farm and for a conventionally neutral boundary layer. Relaxing the effects of wind veer is generally accepted as a good first approximation, typically used in both LES (Calaf et al., 2010; Stevens et al., 2016b) and wind tunnel studies, and furthermore allows for a

better defined comparison with models and numerical simulations.

Although turbulent boundary layers in wind tunnels can reach relatively high Reynolds numbers, they generally can't match the high values of an ABL. It is thus important to verify if the flow characteristics in a wind tunnel boundary layer scale correctly. Especially for wind turbines, the shear of the mean velocity profile, the turbulence levels and the integral length scale of the flow are important for wake interactions. A turbulent boundary layer with a lower Reynolds number has a larger viscous length scale and consequently a thicker viscous wall region. However, as measured for a Reynolds number range of $1430 < Re_\theta < 31000$ (based on the momentum thickness θ), outside of the wall region, the log-law holds consistently for the velocity profile (De Graaff and Eaton, 2000). The Reynolds stresses in the log and outer region, where turbines operate, scale also reasonably well with the boundary layer height and friction velocity for this Reynolds number range (De Graaff and Eaton, 2000). Furthermore, although the inertial range of the spectrum will reach to smaller scales for a higher Reynolds number, the energy containing or low-wavenumber part of the spectrum will scale approximately similar with the outer-layer variables (i.e. the boundary layer height) for high enough Reynolds numbers (Kaimal et al., 1972; Hutchins and Marusic, 2007). By carefully and naturally developing a turbulent boundary layer in a wind tunnel it is thus possible to approximate the main properties and structure of a high Reynolds number ABL, however, the differences need to be verified and kept in mind. The scaling ratio of the boundary layer is defined through the boundary layer height, the roughness length that corresponds to the velocity profile and integral length scale, which should all scale correctly compared to the full-scale situation (Cook, 1978).

The flow over a single turbine blade, operating in the ABL is also characterized by very large Reynolds numbers, e.g. a characteristic velocity of 10 m/s and a length scale of 1 m for the blade chord corresponds to $Re \approx 10^6$. At Princeton University, Miller et al. (2016) are currently making pioneering efforts to perform experiments of a scaled wind turbine at such a high Reynolds number, by making use of a pressurized wind tunnel. Without a pressurized wind tunnel, flow similarity is impossible for small models (e.g. with a rotor diameter the order of 0.1 m, which is necessary to fit a wind farm in a normal sized wind tunnel) due to the too large scale difference and limitations by compressibility effects. As a result, scaled wind turbine models, operating at a lower Reynolds number cannot reach the performance of full-scale equivalents. Researchers have therefore designed turbine rotors that perform better at lower Reynolds numbers (Corten et al., 2004; Cal et al., 2010; Barlas et al., 2016; Bastankhah and Porté-Agel, 2017), but as a result, geometric similarity is not followed anymore (see figure 1.8 for an example). Consequently, such small scale turbines

typically have a higher blade loading (e.g. large relative blade chords) and operate at a lower tip speed ratio (TSR) (Medici and Alfredsson, 2006). The wake of a scaled wind turbine can also become Reynolds number dependent, as the overall thrust force is a result of the detailed airflow over the blades and as the lift and drag coefficients are sensitive to viscous effects at low speeds. Chamorro et al. (2012) measured Reynolds dependent flow properties in the near wake for $Re < 9 \times 10^4$, but found that the far wake is only weakly dependent above $Re > 4.8 \times 10^4$ (based on the rotor diameter and hub velocity). It is clear that despite the considerable designing efforts, scaled turbines might not produce the exact same wake properties as a full-scale equivalent. Several researchers therefore focused instead on the detailed wake structure of a single, or a small number, of larger wind turbine models (Schreck, 2002; Krogstad and Adaramola, 2012), for which the size is limited by a maximum allowable blockage ratio compared to the size of the wind tunnel test section.

Another important aspect of wind turbines is the operational control in function of the incoming flow. Geometric scaling also influences the flow time-scales, such that a control system for a scaled wind turbine with a scaling of $1:100$ needs to respond 100 times faster if the velocity is kept the same. In a study by Bottasso et al. (2014), experiments were performed for a model wind turbine with a diameter of 2 m and a realistic control system in the wind tunnel of the Politecnico di Milano, which has a cross section of 13.8×3.8 m and a test-section length of 36 m. However, for smaller turbine models, a realistic control is very challenging. In wind tunnel experiments of a wind farm with scaled turbines, the control of each model is therefore typically done by changing the loading of the generator through manual adjustments of an electrical resistor (Corten et al., 2004; Cal et al., 2010).

The challenges and cost to study scaled models of wind turbines in a wind tunnel have motivated the development of porous disk models, analogous to the numerical equivalent of an actuator disk model. Porous disk models focus on creating an equivalent far wake by mimicking the flow-through behavior of a wind turbine, with a porous mesh. The mesh is designed such that the thrust coefficient is the same as for a full-scale wind turbine. Several studies have validated the use of porous disk models to simulate the wake of a wind turbine (Builtjes, 1979; España et al., 2011; Aubrun et al., 2012, 2013; Lignarolo et al., 2014b; Theunissen et al., 2015; Camp and Cal, 2016). A detailed analysis, based on PIV, furthermore found that outside the near wake, also the vertical transport of mean kinetic energy can be represented fairly well, making porous disk models suitable for studies of large wind farms, and their interaction with the boundary layer (Camp and Cal, 2016).

Porous disk models are drag based and can thus be expected to be less Reynolds dependent, as the local flow separation points on the grid are fixed by sharp

edges. Due to the significant flow through, porous disk models don't exhibit bluff-body vortex shedding (as shown for a porosity higher than 0.4 by Castro, 1971), in agreement with a typical wind turbine wake, such that wind tunnel measurements in turbulent boundary layers are possible with Reynolds numbers as low as $(2-3)\times 10^4$ (Lim et al., 2007).

Theunissen et al. (2015) used porous disk models with a diameter of 0.025 m and at a Reynolds number (based on the disk diameter) of $Re \approx 3.9\times 10^4$, to perform a wind tunnel study of the Horns Rev layout with 80 models. The total farm drag was measured as a function of layout. However, to study the detailed interaction between the boundary layer and the wind turbines, instantaneous measurements from each model are necessary.

1.3 Objectives

As wind farms are rapidly increasing in size and quantity, a better understanding of the interaction with the boundary layer, and its relation to farm efficiency become important. In general, high-fidelity simulation, such as LES, have not yet explored many different farm layouts because of cost limitations. Furthermore modeling approaches need validation to quantify the effects of their model approximations. Experiments of wind farms play a crucial role in providing data for validation, but have been limited to smaller farms (e.g. 30 turbines or less), have only considered a few layouts (aligned or staggered), and have mainly focused on flow measurements instead of power.

The main goal of this dissertation is to contribute experimental data of more layouts and larger wind farms. In this way we aim at providing a large data-set which can be used for validation, and to further improve our understanding of the flow interactions. This objective requires the design of an experimental apparatus such that many different farm layouts can easily be measured. A large part of this dissertation is thus devoted to the design of a novel experimental setup of a wind farm in the Corrsin Wind Tunnel at the Johns Hopkins University. In order for the flow to approach a fully developed wind farm regime, we envision a setup with at least 100 models of turbines. The corresponding size of a wind turbine model, such that the farm fits in the wind tunnel, is a diameter of approximately 0.03 m. The main challenges for this design are the large scale differences with a full-scale wind farm (e.g. a scale difference of 1:3333 compared to a wind turbine with a diameter of 100 m) and to measure the individual power or force on each model with a high frequency response, such that the detailed flow interactions can be studied. Furthermore, a turbulent boundary layer needs to be developed in the wind tunnel, which is representative for a

scaled ABL. After a careful validation of the experimental apparatus, the aim is to use this setup for extensive wind farm measurements of many different layouts, as part of a power output optimization study. Furthermore, we aim at using the spatio-temporal sampling resolution of the setup to study the relation between the wind farm power output fluctuations and the structure of the turbulent boundary layer.

The main objectives can be summarized as follows:

1. Design and construction of a scaled wind farm model in the Corrsin Wind Tunnel which can be used to study both the entrance region of the farm and the fully developed region. We therefore envision a setup with at least 100 wind turbine models, and for which the layout is easily changeable. The individual models will be instrumented such that the power, or a representative quantity, to be denoted "surrogate power", can be measured.

2. Perform a careful validation of the experimental setup, and its frequency response. It will be verified if the porous disk models can be used to study the effect of wind farm layout on power output and unsteady loading. Furthermore, data from the instrumented wind turbine models will be verified with reference hot-wire measurements.

3. Perform an extensive measurement campaign in which the surrogate power and unsteady loading are measured for many different farm layouts, as part of a power output optimization study, and to produce a large dataset for model validation purposes.

4. Study the fluctuations of the power outputs and their relation to the characteristics of turbulent boundary layers by making use of the spatio–temporal wind farm measurements.

1.4 Outline

Each chapter in this dissertation discusses one of the objectives defined in the previous section, and is briefly summarized below.

The first chapter documents in detail the design of a scaled wind farm, with 100 instrumented porous disk models in the Corrsin Wind Tunnel. The chapter starts with a description of the wind tunnel setup, provides a detailed motivation for the specific design choices, a description for the instrumentation and elaborates on the methodology to reconstruct the signals of interest: a surrogate for the

power output and the spatially averaged incoming velocity. Furthermore, the frequency response of the measurements is verified, the calibration of each porous disk model is explained and the spatial filtering by the porous disk is quantified and discussed.

The second chapter presents a detailed validation of the experimental setup based on measurements of the surrogate power and unsteady loading, the spatio-temporal correlations in the power outputs, and velocity measurements with a hot-wire anemometer.

In the third chapter, the micro wind farm model is employed to perform a large series of measurements for different layouts. Three main series are considered: layouts with a uniform streamwise spacing, with a moderate uneven streamwise spacing, and with an extreme uneven streamwise spacing. The measurements of surrogate power and unsteady loading as a function of row number and layout are analyzed to find an optimal layout. The chapter concludes with an analysis of the advantages of non-uniform wind farm layouts on both the power in the entrance region of the wind farm, and in the fully developed region of the farm.

In chapter 5, the spatio-temporal measurement capabilities are used to study the spectrum of the surrogate power. Based on the experimental observations, the chapter presents a new model which relates the frequency spectrum of the farm power to the turbulent characteristics of a boundary layer. The chapter concludes with a validation of the model with measurements of the micro wind farm.

The final chapter presents a summary of the main conclusions and provides suggestions for future research.

Chapter 2

Design of a scaled wind farm

An experimental setup of a wind farm with a large number of turbines in a wind tunnel environment requires the design of a small-scale wind turbine model. Such a model needs to produce a realistic wake and enable the measurement of the power output, or a representative quantity, with a high temporal resolution. The significant scale differences with full scale wind turbines or farms makes it impossible to achieve flow similarity or match the performance by simple geometric scaling. In the current chapter a porous disk model is designed that fulfills the scale requirements, reproduces a realistic far wake by matching the thrust coefficient of a real wind turbine, and makes it possible to measure the instantaneous thrust force with a high frequency response.

Figure 2.1: Photograph of the micro wind farm setup in the wind tunnel.

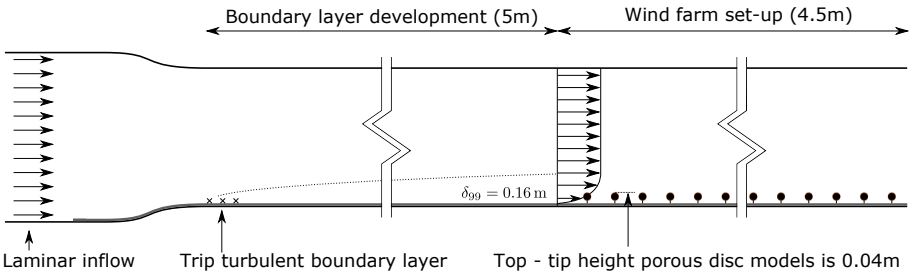

Figure 2.2: Schematic representation of the measurement setup in the Corrsin Wind Tunnel.

In the current work, we aim at fitting 100 of the porous disk models in the Corrsin Wind Tunnel, with realistic spacings. The intended wind farm setup, is illustrated in figures 2.1, 2.2 and 2.3. In the design of the setup, special care was taken to allow fast and easy adaptation of the turbine arrangements (cf. figure 2.3), which is exploited in chapter 4 to study power output and unsteady loading for a large set of different wind farm layouts.

In section 2.1, the flow characteristics of the developed boundary layer in the wind tunnel are discussed. The design of the scaled wind turbine model is motivated and described in section 2.2. The wake properties of the designed model are validated in section 2.3, by comparing the mean velocity and turbulence intensity with results in the literature. Then, the instrumentation of the porous disk with strain gages, to measure the thrust force, is explained in section 2.4, and the frequency response of these measurements is analyzed in the subsequent section 2.5. The calibration of each porous disk model, for the reconstruction of the thrust force, is documented in section 2.6. In the final section 2.7, the spatial filtering effect of the porous disk model, equivalent to the action of full scale wind turbines, is discussed and quantified. The content in this chapter is adapted from Bossuyt, J., Howland, M. F., Meneveau, C. and Meyers, J., "Measurement of unsteady loading and power output variability in a micro wind farm model in a wind tunnel", Experiments in Fluids, 58(1):1, 2017.

2.1 Wind tunnel setup

In this study we make use of the Corrsin Wind Tunnel at the Johns Hopkins University. This closed loop facility has a test section of 0.9m $\times$ 1.2m and an approximate length of 10m. The cross-section increases downstream to compensate for boundary layer development along the walls. A primary

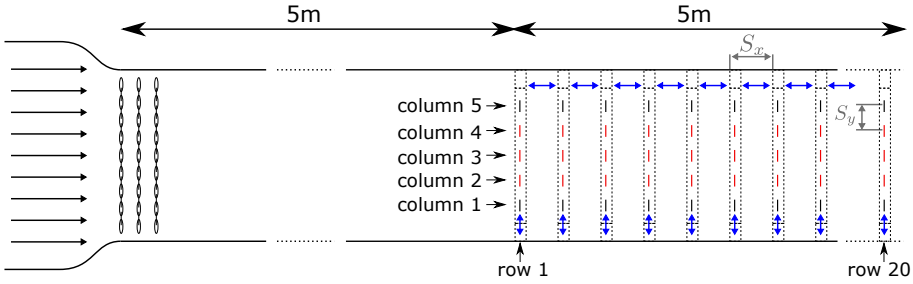

Figure 2.3: Top view of the wind tunnel test section, with a schematic representation of the wind farm layout, consisting of 5 columns in the streamwise direction and 20 rows in the spanwise direction. The blue arrows indicate the changeable layout parameters. Strain signals are recorded from the porous disk models in the central three columns, as indicated in red.

contraction-ratio of 25:1 and a secondary of 1.27:1 result in a smooth inflow at the beginning of the test section with a background turbulence intensity of $TI_u \approx 0.12\%$. Either an active grid, passive grid or a developed turbulent boundary layer are used to generate the desired flow conditions (cf. further discussion in next sections).

A schematic overview of the wind farm measurement setup is shown in figure 2.2 and 2.3. The first half of the wind tunnel is used to develop the boundary layer naturally, after being tripped by chains at the entrance of the test section. The boundary layer has a height of $\delta_{99} = 0.16$m when it reaches the model wind farm, which corresponds to 4 times the porous disk top-height (see section 2.2). Figure 2.4 shows the measured flow characteristics of the boundary layer when it reaches the wind farm. The roughness length is determined by extrapolating the log-law velocity profile to the zero velocity at the wall. The measured roughness length is $z_0 = 0.9 \times 10^{-2}$mm, which with a scaling of 1:3333 corresponds to a full scale value of $z_0 = 0.03$m. This corresponds to a moderately rough boundary layer (VDI-guideline 3783/12, 2000; ESDU, 1985; Counihan, 1975), or short grass in the Davenport-Wieringa roughness classification (Wieringa, 1992). The measured friction velocity, calculated from the slope of the log-law velocity profile and a von Kármán constant of κ=0.4, is found to be $u_\tau = 0.6$ m/s. Scaled to full scale, the representative boundary layer height of this experiment is approximately 500m, for a scaling ratio of 1:3333. This falls in the lower part of the range that can be expected for a neutrally moderately rough boundary layer: approximately 400m to 1500m (Tjernström and Smedman, 1993; Grant, 1986; Guo et al., 2016; Seidel et al., 2012). Moreover, from figure 2.4 it is seen that the porous disk models are located well within the log region of the velocity profile.

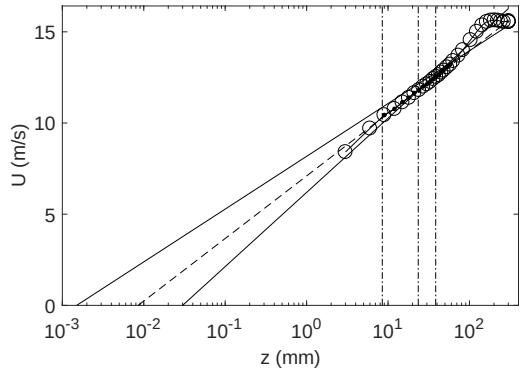

(a)

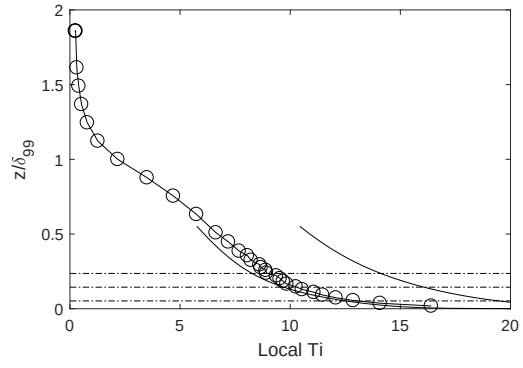

(b)

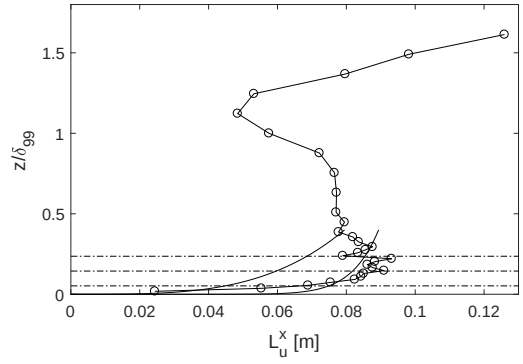

(c)

Figure 2.4: Mean velocity *a*), local streamwise turbulence intensity *b*), and streamwise integral length scale *c*) of the incoming boundary layer, measured with a 1-component hot-wire probe. Dashed lines represent the porous disk top-, bottom- and hub- height. Solid black lines indicate reference profiles by the ESDU and VDI guidelines.

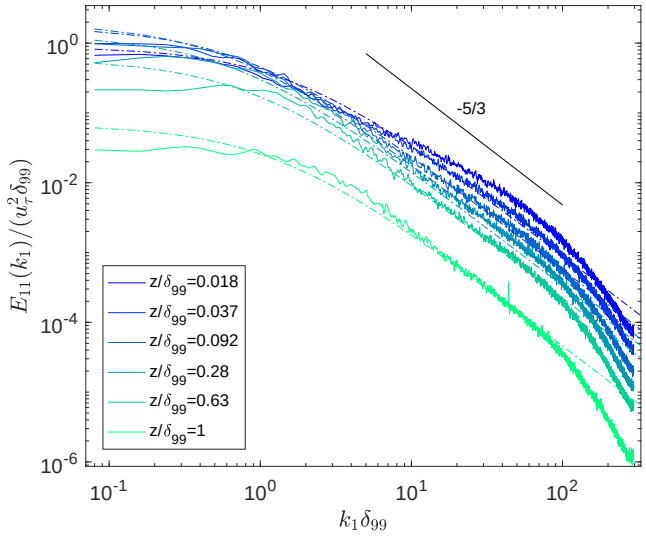

Figure 2.5: Spectral density of the streamwise velocity component, measured with a 1-component hot-wire probe, and for different heights in the boundary layer. The dashed lines show the Kaimal spectrum based on the measured integral length scales (Burton et al., 2001).

The measured velocity profile, local streamwise turbulence intensity and integral length scale are shown in figure 2.4 together with the suggested profiles for a moderately rough neutral atmospheric boundary layer (ABL), according to the VDI-guideline 3783/12 (VDI-guideline 3783/12, 2000) and the ESDU guidelines (ESDU, 1985). The range of integral length scales for a neutral ABL are indicated according to Counihan (1975). The selected measurement points for fitting the log-law profile are indicated with black dots. The streamwise local turbulence intensity at hub height is approximately 10%. The integral length scale Lu_x is calculated from the point where the autocorrelation reaches a value of e^{-1}, and by applying Taylor's hypothesis. The measured integral length scales at hub height are approximately three times larger than the porous disk's diameter and are of the same order of magnitude as the profiles suggested for a scaled moderately rough boundary layer (Counihan, 1975). The integral length scale in the boundary layer is important for a realistic amount of wake meandering in the wind farm, as this phenomena has been connected to the larger scales in the boundary layer (España et al., 2011).

Figure 2.5 shows the spectral density of the streamwise velocity component, for several heights in the boundary layer z/δ_{99}. In the log-layer, the spectra show a relatively good agreement with the Kaimal model, given by $E_{11}(k_1) =$

$4\sigma_u^2(L/\overline{U})/(1+6k_1L/\overline{U})^{5/3}$. The length scale L is defined by matching the high wave number asymptote with the von Karman spectrum leading to $L = 2.329L_u^x$ (Burton et al., 2001), and making use of the measured integral length scale L_u^x.

2.2 Design of a scaled wind turbine model

A first requirement for a scaled wind-turbine representation is a correct characterization of the wake structure (Theunissen et al., 2015). A possible approach is based on geometric scaling of the turbine design (Cal et al., 2010; Medici and Alfredsson, 2006; Odemark, 2012; Lignarolo et al., 2014a, 2015; Ebert and Wood, 1997; Whale et al., 2000; Kang and Meneveau, 2010; Lebrón et al., 2009; Bartl et al., 2012; Chamorro and Porté-Agel, 2011; Corten et al., 2004; Zhang et al., 2012). However, our interest is in placing a large number of turbines in the wind tunnel, which dictates a model rotor diameter of 3 cm. Using rotating blades for such small rotors, and building and operating 100 of them in the wind tunnel is not practical. Moreover, scaled rotating wind turbine models have inherent limitations since perfect flow similarity is not possible due to large scale differences.

An alternative approach to building a scaled turbine model is the use of a porous disk, which exerts a similar integral force to the flow. Wind turbines can be considered porous media by their significant amount of flow-through. Porous disk models have proven useful in reproducing approximate wind turbine wakes in wind tunnel experiments (Lignarolo et al., 2014b; Aubrun et al., 2013; España et al., 2011; Theunissen et al., 2015), and in numerical simulations that use the actuator disk representation (Mikkelsen, 2003; Meyers and Meneveau, 2012; Wu and Porté-Agel, 2011; Stevens, 2016). The near-wake of a porous disk differs as small scale turbulence is produced by a grid, while turbines introduce rotational momentum, tip and hub vortices and turbulence from the blades (Zhang et al., 2012). However, blade signatures and rotational momentum have are found to be overshadowed by ambient velocity fluctuations in the far wake (Aubrun et al., 2013). The main source of turbulence production in the far wake, where the flow becomes self-similar, is therefore velocity shear (Aubrun et al., 2013). By matching the self-similar velocity profile of a wind-turbine wake, porous disk models can create a similar far wake as rotating wind turbine models in case of turbulent flow conditions (Lignarolo et al., 2014b; Aubrun et al., 2013; España et al., 2011; Theunissen et al., 2015; Camp and Cal, 2016). Furthermore, a comparison study (Camp and Cal, 2016) of the flow field in the wake of a porous disk and a rotor model has shown that transport of mean kinetic energy is adequately represented in areas where the rotation of the wake is not a critical phenomenon. Located in a turbulent boundary layer, the region

where wake rotation is significant stays limited to the near wake of the wind turbine. This makes porous disk models useful to study the power output of a large wind farm, when focusing on physical phenomena occurring on length and time scales larger than those corresponding to the rotor diameter.

Next to a correct wake characterization, a second requirement for a scaled wind turbine model is the measurement of the power output or a representative surrogate, with a sufficiently high frequency response. As porous disk models do not rotate and thus don't convert the kinetic energy to electricity, the thrust force can be measured as a surrogate quantity. Fluctuations in the power output are present on many time scales, due to turbulence, large weather phenomena or at higher frequencies due to for example the blade-tower passage. As a wind turbine spatially filters the turbulent flow field over its swept area, the effect of small scale turbulence on the total power output variability is reduced (Farr and Hancock, 2014). In this study we focus on the power output variability generated by the larger energy-containing turbulent eddies, i.e. larger than the wind turbine diameter. The relevant time scales in full scale wind farms range from tens of seconds to hours.

Given the geometric scaling factor of 1:3333 (compared to a full scale wind turbine with a diameter of 100 m), and wind-tunnel velocities that remain in the same range of full scale conditions, equivalent wind-tunnel time scales are 3333 times faster. In order to capture these dynamical timescales of interest, an acquisition frequency up to a few hundred Hertz is required for the wind tunnel experiments.

Full scale wind turbines operating in the below-rated region (often referred to as region 2) are controlled to maximize aerodynamic efficiency by adapting the rotor speed and pitch angle to the incoming wind velocity (Aho et al., 2012). In this regime, the overall turbine thrust coefficient is roughly constant, typically in the range $C_T = 0.75 - 0.85$. It is relatively simple to match such a thrust coefficient with a porous disk, with a value that is only weakly dependent on Reynolds number (Mohamed and LaRue, 1990), so that it remains roughly constant for a range of wind-tunnel velocities. Hence, a properly designed porous disk model can match the control of a turbine working in region 2. In contrast, the rated regime (region 3) occurs less frequently and presents less potential for improvements, as the turbines already operate at their maximum power output. In this study we focus on the below-rated regime.

Given the considerations discussed above, we selected to use porous disk models in the current study. The design of the porous disk was based on the axisymmetric thrust distribution over a wind turbine rotor. The goal was to match the radial distribution of the thrust force by dividing the porous disk in several concentric annular areas. In each annular area, the porosity

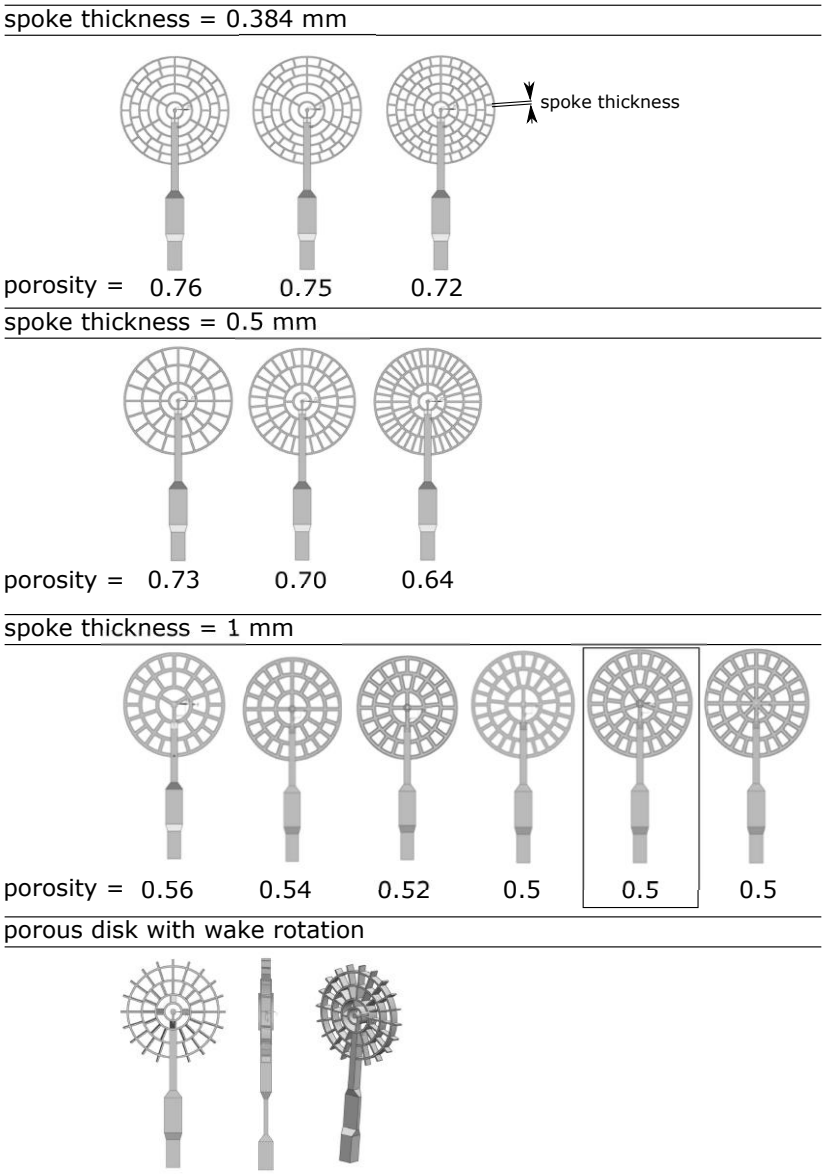

Figure 2.6: Overview of the considered porous disk models in the design process. The most optimal design was selected based on hot-wire measurements of the wake, and strain gage measurements of the thrust force. The selected design is indicated with the square.

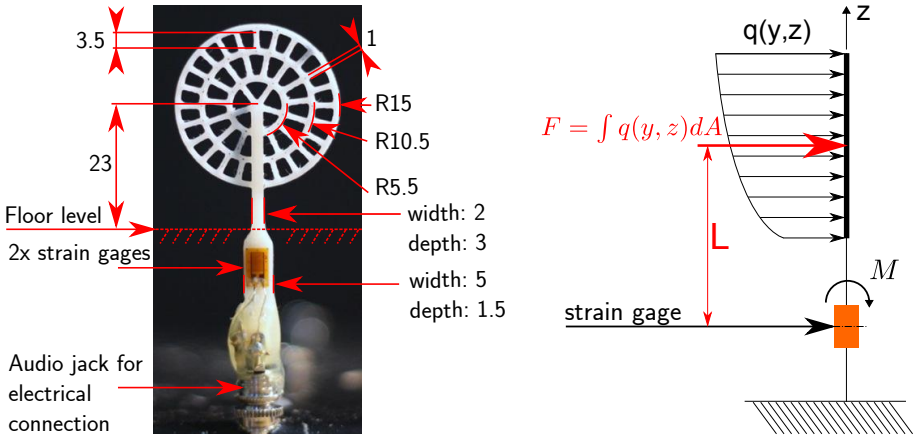

(a) (b)

Figure 2.7: *a*) Photograph of the porous disk model. Dimensions are given in mm. *b*) Schematic representation of the force distribution on the disk, resulting in the bending-strain measured by the strain gage apparatus.

is then determined by the number of spokes. We considered several spoke thicknesses, (0.384 mm, 0.5 mm, 1 mm), and a large number of different porosities, by changing the number of spokes. With hot-wire and strain gage measurements, the design was selected (indicated by the square in figure 2.6) based on the thrust coefficient and the agreement of the wake properties with reports in the literature (figure 2.8). From the considered porous disks, the selected model provided the highest thrust coefficient, and the best agreement with the targeted range, $C_T = 0.75..85$. The lowest spoke thicknesses were not preferred as they were more challenging to 3D print, make it more difficult to reach a thrust coefficient that is large enough, and showed less agreement with wake profiles in the literature. One main approximation of a porous disk is the lack of wake rotation. In an attempt to reduce the porous disk approximation, a model was designed with small plates, instead of spokes, which were angled to create a wake rotation. Hot-wire measurements of the tangential velocity components in the wake showed signatures of wake rotation. However, the mean velocity deficit showed less of a Gaussian shape. Designing a representative porous disk model with the appropriate amount of wake rotation would require a detailed and extensive design process. We decided to use the proven and validated approach of a regular porous disk without wake rotation, to make comparisons with LES more straightforward, and to not over-complicate the experiments.

The final design of the model is shown in figure 2.7 *a*). The porous disk was

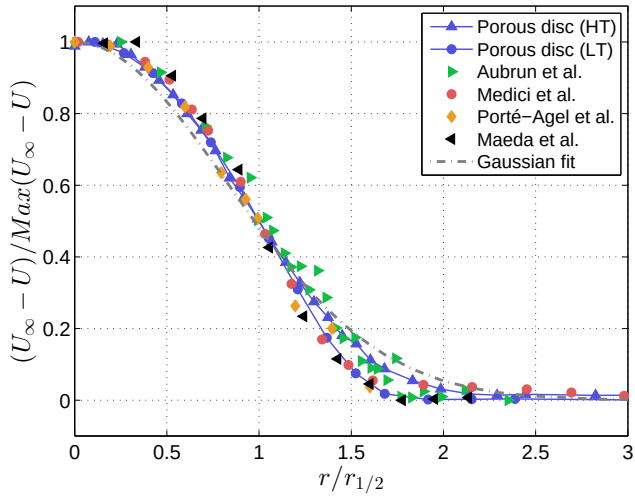

Figure 2.8: Wake measurement of the normalized steamwise velocity deficit at a downstream distance of $x/D = 3$. Turbine models are documented in table 2.1.

designed to match a realistic turbine thrust coefficient while keeping the solidity low. The final design has a measured thrust coefficient of $C_T = 0.75 \pm 0.04$ and a solidity of $\beta = 0.5$. The thrust coefficient was measured in a uniform flow with a background turbulence intensity of $TI_u = 0.12\%$ by means of strain gages on the model tower (cf. §2.4 for details on the strain-gage measurements).

2.3 Wake measurements and comparison

In order to measure the model wake characteristics, a porous disk is tested in the Corrsin Wind Tunnel, using a uniform inflow (the model is mounted sufficiently far from the wall). Wake measurements are performed with an in-house built 2-component hot-wire probe and a computer controlled three-axis traversing system. Data at each point are acquired for 26 seconds with a sampling frequency of 10 kHz and a low pass filter of 5 kHz. The uncertainty on the velocity measurements is estimated to be less than 2% (Thormann and Meneveau, 2015; Hutchins et al., 2009) and the uncertainty of the traversing system is estimated to be less than ± 0.1 mm.

Horizontal profiles are measured at a downstream distance of $x/D = 3$, because of the available data in the literature for this downstream location. The normalized mean streamwise velocity defect and turbulence intensity are shown

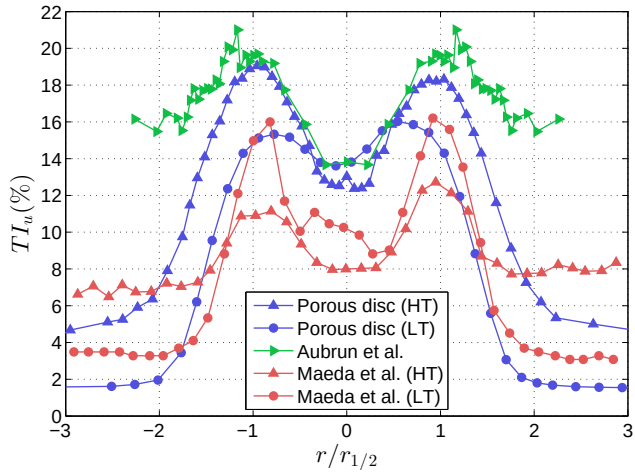

Figure 2.9: Wake measurement of the streamwise turbulence intensity at a downstream distance of $x/D = 3$. Turbine models are documented in table 2.1.

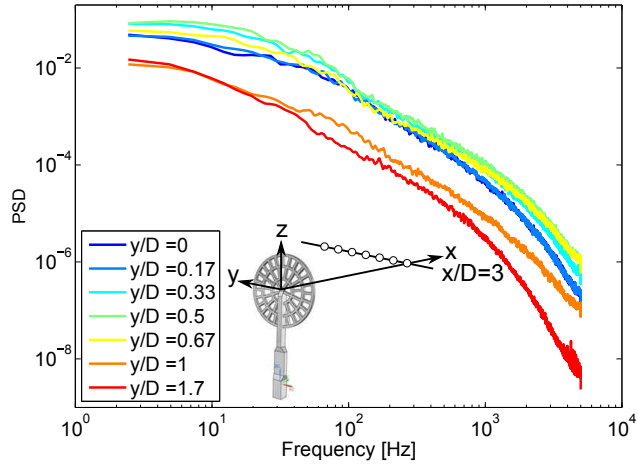

Figure 2.10: One-dimensional spectrum of the streamwise velocity in the wake of the porous disk for the higher turbulence case (HT) at $x/D = 3$ and at various cross-stream positions, shown as open circles.

in figures 2.8 and 2.9 respectively, and are compared to results for rotating wind turbine models in the literature (Aubrun et al., 2013; Medici and Alfredsson, 2006; Zhang et al., 2012; Chamorro and Porté-Agel, 2010; Maeda et al., 2011) — see Table 2.1 for a list. Inflows with two different background turbulence intensity levels are considered. The higher turbulence case (HT) is generated with an active grid (Thormann and Meneveau, 2014). The lower turbulence case (LT) is generated with a passive grid with a mesh size of 0.1m and a bar-width of 0.02m. The measured integral length scale, calculated from the area under the measured autocorrelation function to the first zero-crossing for the streamwise velocity and by making use of Taylor's hypothesis, is approximately 0.15m for the active grid, and 0.07 m for the passive grid.

	C_T	TI_u	Diameter	U_∞
Porous disk	0.75 ± 0.04	1.5% (LT) 5% (HT)	0.03 m	10 m/s
Aubrun et al. (2013)	0.5	13%	0.416 m	2.5 m/s
Medici et al. (2006)	0.84	4.5%	0.18 m	8.5 m/s
Chamorro et al. (2006)	0.42	2%	0.13 m	2.5 m/s
Maeda et al. (2011)		3% (LT) 8% (HT)	0.5 m	7 m/s

Table 2.1: Characteristics of wind turbine models from the literature used for the comparison in figure 2.8 and 2.9.

Figure 2.8 shows the scaled dimensionless velocity profiles, each normalized by the maximum velocity defect and half-wake thickness at $x/D = 3$. Results indicate very good agreement among the measurements for different types of turbine models. At $x/D = 3$ the data are slightly less smeared out than the self-similar Gaussian profile that can be expected in the far wake. Discrepancies between the streamwise turbulence intensity profiles in figure 2.9 originate from differences in the ambient flow characteristics and the thrust coefficients. However, a qualitatively similar shape is seen for all profiles. This suggests that velocity shear is the main contributor for the turbulence production in the far wake, allowing the porous disk to match profile shapes from rotor models. It is seen that at a distance of only $x/D = 3$ already a good agreement is found between the measured profiles and those in the literature for rotor models. It is expected that this agreement will improve further downstream, as blade signatures keep reducing and the wakes become more self-similar.

Finally, figure 2.10 shows the power spectrum of the streamwise velocity in the wake of the porous disk, at different spanwise locations. The absence of a distinct peak in the spectrum confirms that the porous disk model does not display significant bluff body vortex shedding. Overall, it is concluded that

the porous disk model is capable of reproducing the velocity and turbulence intensity profile in the far wake, with sufficient accuracy to allow the study of the wind farm power output, focusing on length and time scales larger than those corresponding to several rotor diameters, and away from the near-wake region.

2.4 Model instrumentation

By making use of the known thrust coefficient and measuring the thrust force, it is possible to estimate the incoming velocity at the porous disk model in a wind-farm setup. The equivalent wind turbine power can then be estimated using standard relations from momentum theory. The total thrust force is determined by measuring the bending of the model tower with a strain gage apparatus. An Omega SGD-3/350-LY11 strain gage is attached to each side of the tower (see figure 2.7) and measured in a half-bridge configuration with an Omega iNET-423 and iNET-555 acquisition device. Making use of the i512 wiring box, no external bridge resistors are needed.

The measured strain depends linearly on the resulting bending moment acting at the location of the strain gage, assuming constant material properties (figure 2.7 *b*)). For uniform load distributions and presuming a static situation, the bending moment corresponds to the total thrust force times the distance between the center of the disk and the strain gage L, with $q(y, z)$ the load per unit area and $F = \langle q \rangle A$:

$$M = \int_A q(y, z) z dA = \langle q \rangle \langle z \rangle A = FL. \tag{2.1}$$

However, for non-uniform load distributions, the center of the force will shift away from the center of the disk, cf. figure 2.7 *b*), and is not known during the measurements. This effect is considered by decomposing the force distribution in a spatially averaged and spatially fluctuating part.

$$q(y, z) = \langle q \rangle + \widetilde{q}(y, z) \tag{2.2}$$

$$M = \langle q \rangle \langle z \rangle A + \int_A \widetilde{q}(y, z) z dA \tag{2.3}$$

The second term of the static bending moment relation represents the expected mean measurement error due to shear in the mean velocity profile. This static offset is estimated to be on the order of +4% by using the incoming mean velocity profile and assuming a constant thrust coefficient over the disk. Models more downstream can see a more uniform velocity profile due to wake mixing

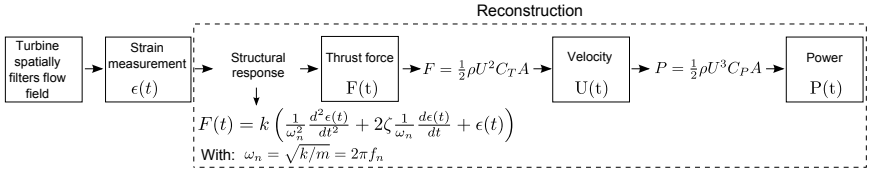

Figure 2.11: Reconstruction procedure to estimate the power output from the strain gage measurement.

(Chamorro and Porté-Agel, 2011), and hence a smaller offset. Because the mean row power estimates are normalized by the estimated power in the first row, this static offset can lead to a lower power estimate for the downstream rows.

In a dynamic load situation, in which the thrust force fluctuates with the turbulent velocity field, the relation between measured bending moment, by the strain gage, and thrust on the disk is more complicated. By modeling the structural response of the model as a harmonic oscillator using its first and dominant natural frequency, the dynamic thrust force behavior can be reconstructed from the strain measurements. The steps in the reconstruction procedure are shown in figure 2.11. To this end, the natural frequency f_n, spring k and damping ζ coefficients are determined for every porous disk model from a static and dynamic calibration (see §2.6 for details), allowing us to obtain measured values of the thrust force $F(t)$ from the measured strain time signal. With the thrust coefficient, the incoming spatially averaged velocity signal $\langle U \rangle(t)$ is reconstructed based on $F(t) = \rho \langle U \rangle^2(t) C_T A/2$, where $A = \pi D^2/4$ is the rotor area. The velocity represents a uniform incoming velocity which would result in the same thrust force as measured. With the reconstructed velocity, it is possible to estimate the equivalent power signal $P(t) = \rho \langle U \rangle^3(t) C_P A/2$ of the model by assuming a realistic power coefficient. Note that the results shown in this text, are always in terms of the ratio of power to the power of the first row, so that they are independent of the actual power coefficient.

2.5 Frequency response analysis

The accuracy of important parts of the reconstruction scheme is verified by comparing the reconstructed velocity $\langle U \rangle(t)$ from a porous disk with the simultaneously measured velocity from a hot-wire probe. The verification is performed for a model in the wind farm, here shown for row 8 and column 2 of the staggered wind farm layout. The measurement setup is shown in figure 2.12. The streamwise velocity was measured with a one-component hot-wire probe 30 mm upstream from the porous disk center. Both the hot-wire and

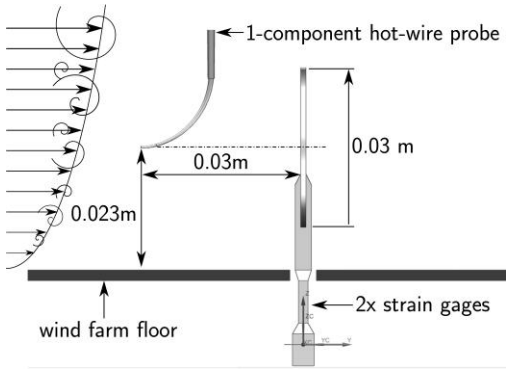

Figure 2.12: Measurement setup for the verification of the reconstruction procedure shown on figure 2.11, for a porous disk model in the wind farm.

strain signals were sampled at a frequency of 10 kHz and filtered by an analog low-pass filter at the Nyquist frequency or lower (5 kHz for the hot-wire probe and 4 kHz for the strain gage apparatus).

Figure 2.13 shows the power spectral density of the measured and reconstructed signals. The measured strain signal is shown in green and shows a clear peak at the natural frequency of the porous disk model. Frequencies above 270 Hz are not considered for the strain measurements, to ensure a sufficient signal to noise ratio. The power spectrum of the reconstructed thrust signal is shown in red, where the structural response model has compensated for the peak due to the natural frequency. The natural frequency is approximately 200 Hz and compares in this measurement to a reduced frequency of 0.6, when normalized by the mean hub height velocity and disk diameter. It can thus be expected that the signature of the spatial filtering by the porous disk can be captured in the measurements, i.e. the thrust force and related velocity follow from an integral over the disk area (see figure 2.7), and are thus not corresponding to a point measurement. Comparing the spectrum of the reconstructed velocity (shown in black) with the spectrum of the hot-wire velocity (shown in blue), a difference is indeed observed, consistent with the effect of a spatial filter, due to the averaging of the velocity over the rotor area. Spatial filtering is also present in full scale wind turbines (in section §2.7, the filter transfer function is quantified in more detail). Overall, considering the spatial filtering, the porous disk model features a frequency response up to approximately 200 Hz or a reduced frequency of 0.6 in the wind farm measurements described here.

Figure 2.14 shows the measured hot-wire velocity and the reconstructed velocity from the porous disk. Both signals are filtered by a digital sharp cut-off filter

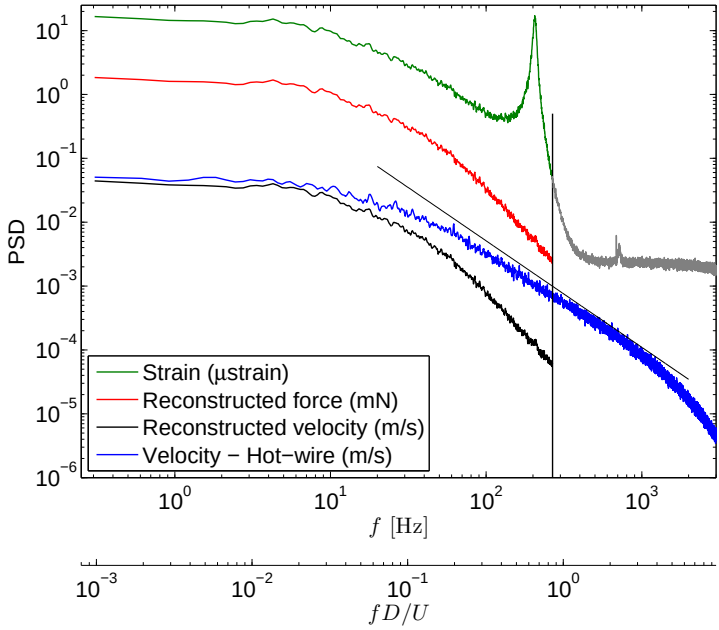

Figure 2.13: Power spectral density of the measured and reconstructed signals for a porous disk model in row 8 and column 2 in a staggered wind farm case. A second x-axis is shown with the frequency normalized by the mean hub-height velocity and the diameter of the model.

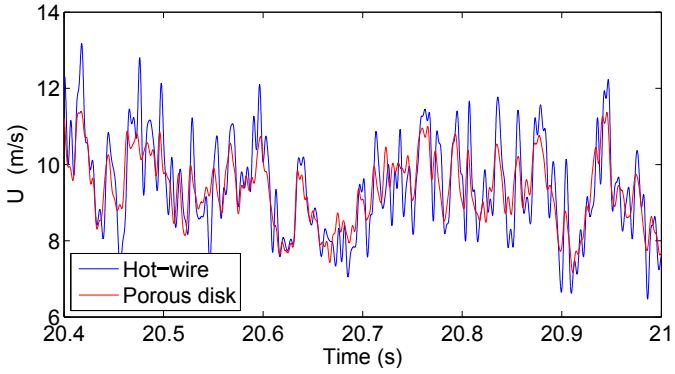

Figure 2.14: Comparison of the reconstructed velocity from the porous disk in row 8 and column 2 in a staggered wind farm and the velocity from the hot-wire probe. Both signals are filtered at $f = 200\,\mathrm{Hz}$. The correlation coefficient between both signals is $r = 0.86$.

with $f_c = 200\,\text{Hz}$ for the comparison. The qualitative comparison of both time signals in figure 2.14 shows a relatively good agreement. Differences are attributed to the difference in location between the hot-wire probe and the porous disk, and to the effect of spatial filtering by the porous disk. The correlation coefficient between both signals is $r = 0.86$.

2.6 Model calibrations

The reconstruction approach discussed above requires four physical calibration constants for each model: the spring constant k, damping constant ζ, natural frequency f_n and thrust coefficient C_T. Porous disk models were manufactured with 3D printing to guarantee the best possible accuracy. However, to account for the small changes in the material properties and the manual strain gage attachment-process, every model was calibrated individually.

The spring constant is determined from a static calibration, giving the relation between the force on the disk and the measured strain. An apparatus for this static calibration was designed to guarantee high accuracy and to facilitate the calibration of a large number of models (see figure 2.15). A force is applied by moving the porous disk vertically in small steps of approximately 0.02 mm, while a wedge applies the force on the center of the disk. The wedge is located on a precision scale (Tree HRB 203), which allows the measurement of the force. To avoid the effect of air drafts on the force, the air volume around the porous disk is closed. The force and strain measurements are controlled together with the vertical traverse system. The measurement uncertainties are estimated to be smaller than ±0.5% for the force and ±1-4% for the strain, depending on the sampling rate and sample integration time. The precision of the traverse system has no direct influence on the calibration procedure. Through an error propagation analysis, the uncertainty of the spring constant is found to be $\delta_k = \pm 4\%$.

The damping coefficient is measured from the impulse response. Within high accuracy, it was found to be the same for every model, so a single value ζ=0.03 is taken. The natural frequency could in principle also be determined from the impulse response. However, it can also be computed from the peak in the spectrum of the strain signal, and as a result is inherently measured during every wind farm measurement. The average natural frequency is $\overline{f_n} \approx 200\,\text{Hz}$. The measured spring constants and natural frequencies of the models selected for the measurements are shown in figure 2.16.

Finally, the thrust coefficient was measured for all models by a simultaneous measurement of the strain from the porous disk and the velocity from a

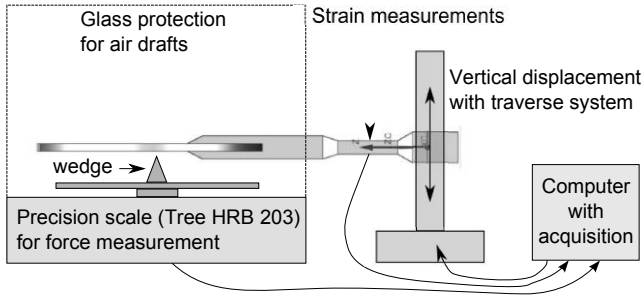

Figure 2.15: Static calibration setup. The precision scale and vertical traverse are computer controlled for an automatic calibration procedure.

Pitot probe. The porous disk models were located in a uniform flow with a turbulence intensity of $TI_u = 0.12\%$. The thrust coefficient is averaged over three measurements for each model. Each measurement was performed for 5 minutes, covering a velocity range from 6 m/s up to 12 m/s to verify the Reynolds dependency. As every porous disk is designed with exactly the same shape, variations in the measured thrust coefficient at a constant velocity are expected to be related to manufacturing uncertainties, while variations as function of velocity are expected to be directly related to Reynolds number dependencies. We observed that from 6 m/s to 7.5 m/s, the thrust coefficient increases from $C_T \approx 0.6$ to $C_T \approx 0.74$. Between 7.5 m/s and 12 m/s the thrust coefficient remains roughly constant in function of velocity with a value of $C_T = 0.75 \pm 0.04$. The related distribution of the thrust coefficient over the different models is shown in figure 2.17, for velocities between $7.5 < U < 12$ m/s. Since during the experiments, the lowest mean hub-height velocity was 8 m/s, and the porous disk models operate in a highly turbulent boundary layer, we assume the thrust coefficient to be Reynolds independent for the considered range of velocities.

From the static calibration it became clear that an extra measurement uncertainty is introduced by the creep of the material when a force is applied over a long time. Special care was taken during the design to minimize the amount of creep that the models show. The ABS polymer was found to give the best material properties. The amount of creep increases with the amount of strain. An optimal stiffness was determined for the lowest amount of creep while still maintaining enough measurement precision and a high natural frequency. Moreover, creep is linearly corrected with the measured strain at the end of the measurement, when the strain should be zero. This corrections is typically on the order of 4%.

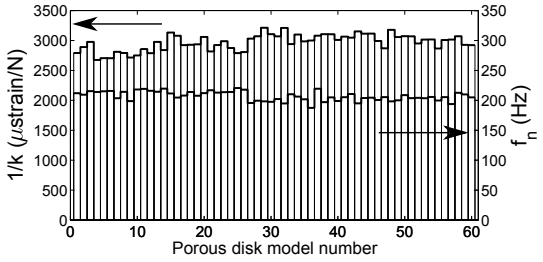

Figure 2.16: The distribution of the measured spring constants (top line) with a measurement uncertainty of $\delta_k = \pm 4\%$ and the natural frequency (bottom line) for the selected porous disk models.

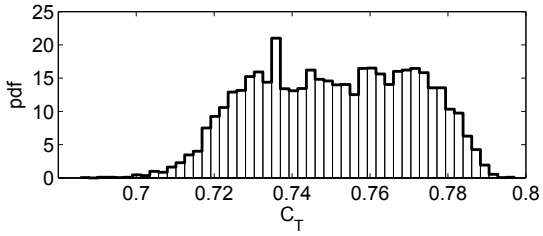

Figure 2.17: The distribution of the measured thrust coefficient with $C_T = 0.75 \pm 0.04$.

The uncertainty of the reconstructed signals was estimated from an error propagation analysis resulting in: $\delta U_i/U_1 = \pm 0.03$ and $\delta P_i/P_1 = \pm 0.08$.

2.7 Spatial filtering

We further investigate the effect of spatial filtering by the porous disk on the reconstructed velocity spectrum. First, we linearize the bending moment-velocity relation. Inertial effects on the thrust force can be neglected for frequencies significantly lower than the natural frequency, in our case lower than approximately 100Hz. For this frequency range, or by correcting with the structural model from figure 2.11, the bending moment-velocity-relation can be approximated by making use of axial-momentum theory:

$$M(t) = \frac{1}{2}\rho C_T \frac{1}{(1-a)^2} \int_A U_d^2(y,z,t) z dA, \tag{2.4}$$

where the bending moment-velocity relation is here expressed in terms of the local disk velocity $U_d(y,z,t) = U(y,z,t)/(1-a)$, with the axial induction factor a defined from axial-momentum theory as $a = (1-(1-C_T)^{1/2})/2$ and $U(y,z,t)$ the free stream velocity. The velocity is then decomposed spatially:

$$U_d(y,z,t) = \langle U_d \rangle(t) + \widetilde{U}_d(y,z,t), \tag{2.5}$$

and temporally:

$$\langle U_d \rangle(t) = \langle \overline{U}_d \rangle + \langle U_d \rangle'(t) \tag{2.6}$$

$$\widetilde{U}_d(y,z,t) = \overline{\widetilde{U}}_d(y,z) + \widetilde{U}'_d(y,z,t). \tag{2.7}$$

By neglecting the higher order terms, the bending moment-velocity relation for the moment fluctuations can be linearized,

$$\frac{M'(t)(1-a)^2}{\frac{1}{2}\rho C_T A} \approx 2\langle \overline{U}_d \rangle \langle U_d \rangle' \langle z \rangle \tag{2.8}$$

and defined in terms of the incoming free-stream velocity fluctuations $\langle U \rangle'(y,z,t)$ by making use of the relation for the induction factor.

$$\langle U \rangle'(t) \approx \frac{M'(t)}{\rho C_T A \langle \overline{U} \rangle \langle z \rangle} \tag{2.9}$$

To model the effect of spatial filtering, we follow the approach by Wyngaard (1968) for spatial filtering by hot-wire probes and Lavoie et al. (2007) for spatial filtering effects of PIV. The unfiltered (E_{11}) and filtered ($E_{11}^{<}$) one-dimensional energy spectrum of the velocity fluctuations are defined by the integration of the unfiltered (E_k) and filtered ($E_k^{<}$) velocity-spectrum tensor over all transverse wave numbers k_2 and k_3.

$$E_{11}(k_1) = 2 \iint_{-\infty}^{\infty} E_k(\mathbf{k})\, dk_2\, dk_3, \tag{2.10}$$

$$E_{11}^{<}(k_1) = 2 \iint_{-\infty}^{\infty} E_k^{<}(\mathbf{k})\, dk_2\, dk_3, \tag{2.11}$$

The spatial filter of the porous disk can be described by a radial box filter with a diameter Δ in physical space and defined by the *sinc* function in wavenumber space. The spatial filter is expressed in function of the radial wavenumber $k_r^2 = k^2 - k_1^2$:

$$A(k_r) = \frac{\sin(k_r\Delta/2)}{k_r\Delta/2}. \tag{2.12}$$

The one dimensional spectrum can be computed by assuming isotropic turbulence to model the velocity-spectral tensor:

$$E_k(\mathbf{k}) = \frac{e(k)}{4\pi k^2}\left(1 - \frac{k_1^2}{k^2}\right), \tag{2.13}$$

multiplying by the filter's transfer function $A^2(k_r)$ and integrating:

$$E_{11}^{<}(k_1) = \int_0^\infty A^2(k_r)\frac{e(k)}{k^2}\left(1 - \frac{k_1^2}{k^2}\right) k_r\, dk_r. \tag{2.14}$$

For the energy-spectrum function $e(k)$, a Kolmogorov spectrum $e(k) = C_K\epsilon^{2/3}k^{-5/3}$ is assumed:

$$E_{11}^{<}(k_1) = C_K\epsilon^{2/3}\int_0^\infty \left(\frac{\sin\left(k_r\Delta/2\right)}{k_r\Delta/2}\right)^2 (k_1^2 + k_r^2)^{-17/6}k_r^3\, dk_r. \tag{2.15}$$

The unfiltered spectrum is given by:

$$E_{11}(k_1) = \frac{18}{55}C_K\epsilon^{2/3}k_1^{-5/3}. \tag{2.16}$$

By numerical integration, the filter transfer function can be computed:

$$r_u(k_1) = \frac{E_{11}^{<}(k_1)}{E_{11}(k_1)} \tag{2.17}$$

In figure 2.18 the numerically integrated transfer function $r_u(k_1)$, applied to an infinite inertial range, is shown by the top solid line in red, and is compared with the ratio of the hot-wire signal and the reconstructed velocity from the porous disk strain-gage signal. It is observed that the analytical spatial filter does not perfectly describe the measured ratio.

The spatial filter is further investigated with LES of a turbulent boundary layer.[1] The spatial filter is estimated by comparing the frequency spectrum of

[1] An LES of the wind tunnel setup was performed with the SP-wind code developed at KU Leuven (Meyers and Sagaut, 2007; Delport et al., 2009; Calaf et al., 2010; Munters et al., 2016a). The spatially developing boundary layer was simulated by limiting the boundary layer height in the precursor simulation with a vertical damping layer. In this region a forcing is added to diminish the fluctuations and drive the mean velocity towards a symmetric boundary condition at the boundary layer height. The damping coefficient was set to $0.005s^{-1}$. The velocity is sampled from the precursor simulation and applied to the main domain with a fringe region. In the main domain the boundary layer can develop freely. The simulation was run at full scale conditions, e.g. a scaling of $1:3333$ compared to the wind tunnel. The boundary layer height was set to 500 m and the roughness height to $z_0 = 0.4$ m. The grid resolution was $\Delta x = 22$ m, $\Delta y = 20$ m and $\Delta z = 10$ m in the boundary layer region. Above a height of 1 km the vertical grid size was smoothly increased to $\Delta z = 100$ m. The dimensions of the precursor simulation were $11 \times 4 \times 2.6$ km, the main domain has the same height and width, and the velocity for the spatial filter was sampled at a distance of 3 km from the start of the domain.

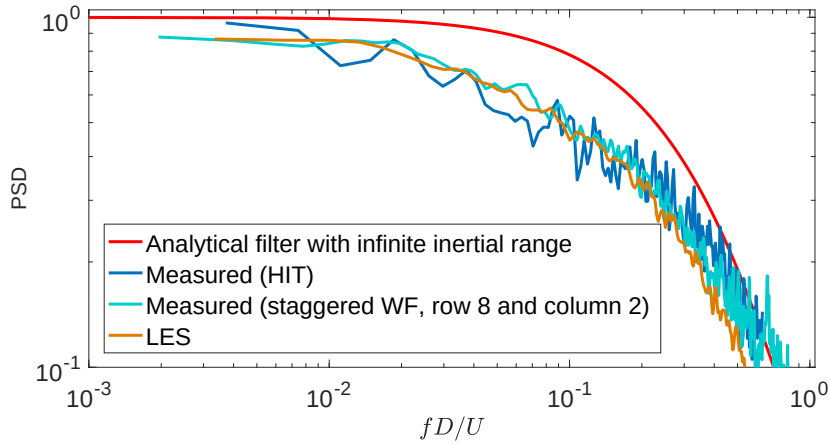

Figure 2.18: Power spectral density of the spatial filtering by the porous disk for a measurement in homogeneous isotropic turbulence (HIT) generated with an active grid (cf. §2.3) and for a porous disk model in the wind farm, compared to the analytically described filter applied to an infinite inertial range, and compared to the spatial filter measured from LES of a turbulent boundary layer.

the velocity at hub height, with the spectrum of the velocity averaged over an area equal to the rotor area of the porous disk model. Thus, the LES filter does not include the presence of an actuator disk model or the nonlinear effects of measuring the moment with strain gages. The spatial filter from LES shows a good agreement with the porous disk measurements.

As the measured filter from a porous disk in a homogeneous isotropic turbulent (HIT) inflow and in the wind farm produce very similar results, we hypothesize that the expected difference with the analytical filter is not directly related to the anisotropy in the boundary layer, but rather the aliasing of filtering transverse and vertical wavenumbers. Although this aliasing is modeled with the analytical filter, the effect is not visible because the modeled inertial range extends to an infinitely small wavenumber. To improve the analytical estimate for the spatial filter, a better model for the wavenumber spectrum is necessary. It is concluded that the difference between the hot-wire and the porous disk spectrum is mainly caused by spatial filtering, which was quantified with measurements and a LES simulation.

2.8 Concluding remarks: a micro wind farm

A porous disk model with a diameter of 0.03 m was designed which can reproduce the far wake properties of a wind turbine, by matching a realistic thrust coefficient of $C_T = 0.75 \pm 0.04$. The porous disk models are instrumented with two strain gages to measure the thrust force. By making use of momentum theory, and the measured thrust coefficient, the measurements can be used to estimate the spatially averaged velocity and a surrogate power output. The frequency response of the measurements reaches up to the natural frequency of the model, and is high enough to capture the spatial filtering by averaging the velocity over the disk area. One hundred instrumented porous disk models were manufactured, and each was calibrated individually with an automated setup. An array of all porous disk models was installed at the end of the Corrsin Wind Tunnel test section. The first part of the test section is used to develop a boundary layer naturally, after tripping at the entrance. The wind tunnel floor is designed in such a way that the strain gage part of each porous disk is located underneath the wind farm floor (see figure 2.7 (a) and 2.12). As a result, the boundary layer height is approximately 4 times higher than the top height of the models, and scales realistically. As intended, the wind farm consists of 20 rows and 5 columns (see figures 2.2 and 2.3). The wind farm setup was designed specifically to facilitate the measurement of many different layouts. The arrangement of the models can be adjusted by sliding the rows in the spanwise direction, or by increasing the streamwise spacing, as indicated in figure 2.3. Porous disk models can be interchanged easily by using an audio jack plug for the electrical connection of the strain gage sensors. Wooden chamfers are placed in the bottom corners of the wind tunnel test-section to prevent secondary flows.

Chapter 3

Micro wind farm validation

In chapter 2, a scaled model for a large wind farm with 100 instrumented porous disk models was designed and installed in the Corrsin Wind Tunnel. In this chapter, the performance of the experimental setup is validated with measurements of the surrogate power output and flow measurements with a hot-wire probe. Section 3.1 gives an overview of the measurement setup used for the validation measurements in this chapter. Wind farm measurements for six different arrangements, ranging from aligned to staggered, are presented to verify the setup's capabilities for studying the effects of layout on power. In section 3.2 the surrogate power and unsteady loading are discussed. The results are validated by comparing the power from the aligned layout with field data for the Horns Rev wind farm. In section 3.3, the frequency response of the data acquisition is used to study the correlations in the power outputs, and in section 3.4, hot-wire measurements of the flow field are used to validate the setup in more detail. Specifically the reconstructed spatially averaged velocity and turbulence intensity from the porous disk models are compared with the hot-wire measurements. The content in this chapter is adapted from Bossuyt, J., Howland, M. F., Meneveau, C. and Meyers, J., "Measurement of unsteady loading and power output variability in a micro wind farm model in a wind tunnel", Experiments in Fluids, 58(1):1, 2017.

3.1 Measurement setup

This section describes the data acquisition characteristics for all wind farm measurements presented in this dissertation. To use the available

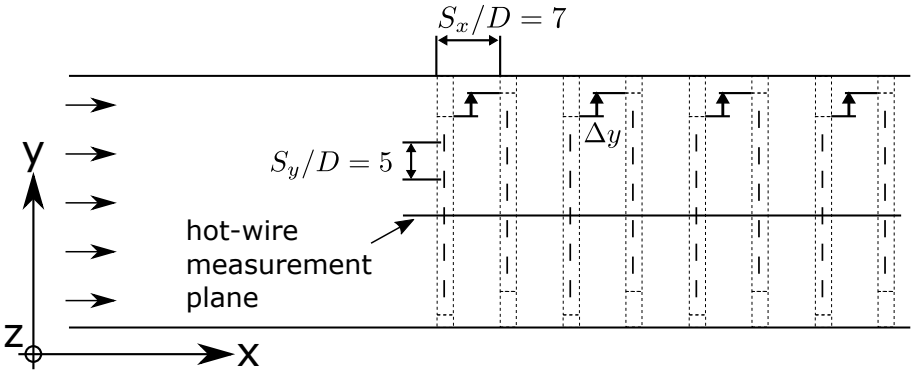

Figure 3.1: Wind farm layouts considered for the validation of the setup. The even rows are slided over a range of $\Delta y/D = 0 \ldots 0.5 \ldots 2.5$, from aligned to staggered.

instrumentation resources (60 data acquisition channels) on those turbine models least affected by wind farm border effects, the sixty porous disk models in the central three columns were selected for the strain gage measurements. The specific layout parameters used for the measurements in this chapter are indicated in figure 3.1. No signals were acquired from the models in the two side columns (column 1 and 5 in figure 2.3). Strain signals are measured with Omega iNET-423 voltage input cards in combination with one Omega iNET-430 16bit A/D converter. The internal 4 kHz low-pass filters are used to reduce high frequency noise. The large number of simultaneous strain gage measurements limits the sampling frequency per model to 0.866 kHz, lower than advised by the Nyquist criteria for the available filter. However, measurements for a single model have shown that the aliasing error is small for the frequency range of interest: $0 - 200$ Hz. The measurement time varies between 5 to 15 minutes, which is over 3 to 9×10^4 times the largest integral time scale (≈ 9 ms) measured for the incoming boundary layer, so that very well converged statistics are obtained.

For the purpose of this chapter, measurements were performed for six different layouts, ranging from aligned to staggered. The different arrangements are configured by sliding the even rows in the spanwise direction, as indicated in figure 3.1.

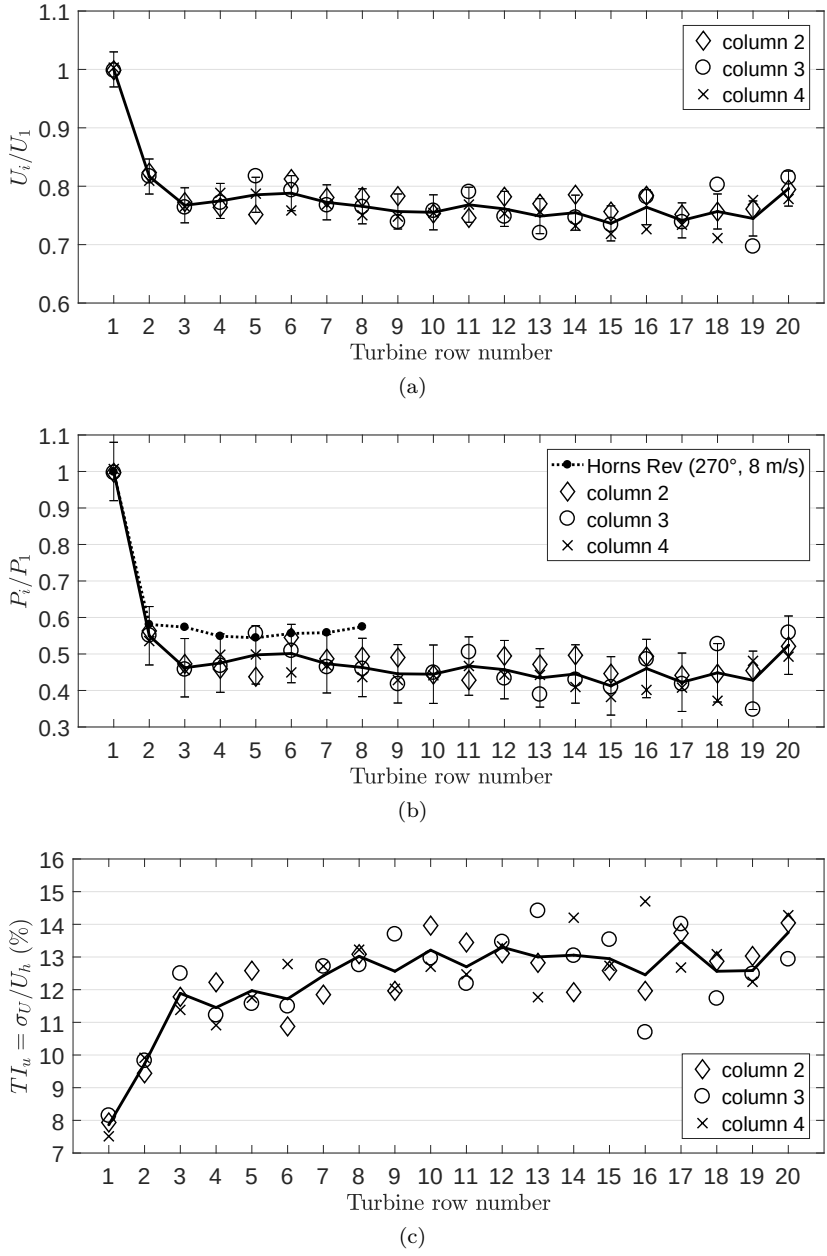

Figure 3.2: Mean reconstructed velocity (a), mean reconstructed row power (b), and turbulence intensity (c), measured by the porous disk models configured in an aligned layout.

3.2 Surrogate power and unsteady loading

The spatially incoming velocity, surrogate power output and turbulence intensity, reconstructed from the strain measurements, are shown in figure 3.2. Symbols indicate individual porous disk models. Variations within each row are expected to be directly related to the measurement uncertainty and indicate the need to average over multiple models for each row.

The reconstructed power (figure 3.2 (b)) is compared with data measured at the Horns Rev wind farm for a wind direction of $270 \pm 2°$, a velocity of 8m/s and for neutral thermal stratification (Barthelmie et al., 2007). For this wind direction the wind turbine rows are aligned with the wind direction from west to east and $S_x/D = S_y/D = 7$, while the columns are slightly angled to the perpendicular direction. Both cases show a similar power deficit and the same trend: the power decreases significantly after the first row, after which it stays approximately constant.

It is important to consider the differences between both cases. Horns Rev operates in a slightly rough boundary layer with a turbulence level of $< 8\%$, while the experiment is done for a moderately rough boundary layer with a turbulence intensity of 10% at hub height. While a higher turbulence level can lead to a better wake recovery and a smaller power deficit, the higher roughness length and velocity shear for the moderately rough boundary layer can lead to a lower power output asymptote at the end of the wind farm (Meneveau, 2012). It should also be noted that the spanwise spacing of the turbines in Horns Rev is $S_y/D = 7$, while this spacing is smaller in the experiment: $S_y/D = 5$.

Turbulence intensity is calculated from the reconstructed porous disk velocities and is therefore directly related to the unsteady loading of the wind turbines. As the measurements are limited to a frequency of up to 200 Hz, the calculated turbulence intensity does not represent the total variance. Also the increase in turbulence intensity levels off. However, only after approximately ten rows.

Figure 3.3 shows the reconstructed mean row power and turbulence intensity for the six different wind farm layouts. The change in mean row power shows a consistent trend as function of the wind farm layout. The most prominent improvements are seen for the first ten rows. For a staggered layout, the estimated power output is approximately equal for the first two rows, while the improvement at the end of the wind farm is limited. These trends are consistent with observations from Horns Rev for a wind direction of 263° (Barthelmie et al., 2011) and with the LES simulation study of Stevens et al. (2014). By measuring the same trends as seen by a full scale wind farm, we conclude that the setup is useful to study differences in the mean row power between different layouts, within the limitations by the measurement uncertainty. To

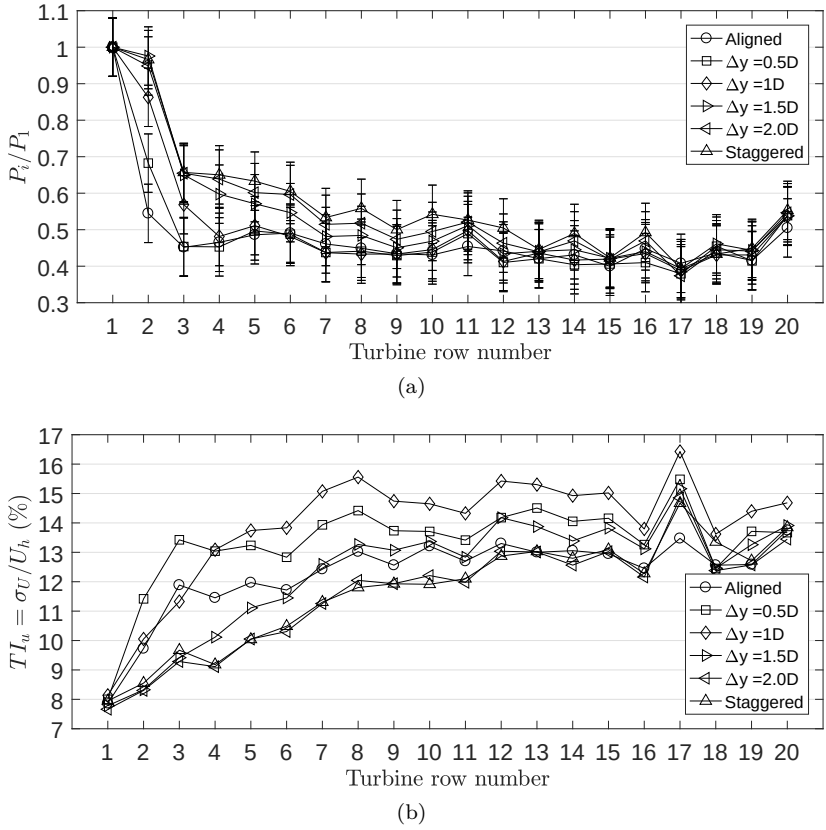

Figure 3.3: Mean reconstructed row power and turbulence intensity as a function of the wind farm layout, measured by the porous disk models.

validate the absolute values of the power reduction a more detailed comparison is necessary with data for a wind farm with the exact same inflow conditions and wind farm characteristics. Averaging over all three models in each row is necessary to reduce the uncertainty. However, row 17 still shows a significant and consistent difference with its neighboring rows, which is expected to be caused by a systematic measurement error from a model in row 17. The faulty measurement is possibly related to the calibration or a defect of the strain gage at the time of measurement.

The turbulence intensity measurements show the highest unsteady loading for the intermediate layouts, In this case, the even rows are only slightly shifted, e.g. $0.5D$ and $1D$. The staggered layout results in the lowest unsteady loading, which is expected due to the largest turbine-to-turbine distance, and in good

agreement with results from Chamorro et al. (2011).

Figure 3.4 shows the power spectral density of the reconstructed velocity signals, measured by the porous disk models, for the aligned and the staggered layout. The spectra are calculated for each individual model and then averaged over each row. The spectrum of the first row can be considered as a measurement of the incoming flow with the application of a spatial filter. Where the spectrum of the hot-wire velocity indicates an inertial range with a slope of approximately $-5/3$ (starting at $fD/U \approx 0.2$ in figure 2.13), the spectrum of the porous disk velocity is steeper due to spatial filtering.

For an aligned wind farm, the spectrum of the second row shows an increase in variance for a well defined frequency range, indicating the added turbulence by the upstream wake. The increase in variance for the third row of the staggered wind farm is observed at approximately the same frequency range, independent of the difference in wind farm layout. The corresponding reduced frequency is approximately 0.2, and has been connected to wake meandering in the wind tunnel experiments by Coudou et al. (2017). For more downstream rows the increased variance spreads over a larger range of scales.

Figure 3.5 shows the influence of the layout and the number of rows on the total wind farm power output. The output is normalized by the total power for a wake-less wind farm.[1] The influence of the layout on the mean row power is the most significant in the first rows of the wind farm. Considering more rows, hence reduces the difference in total power between an aligned and staggered case. However, for a wind farm with twenty rows, the staggered layout still results in a 6% higher power output than the aligned layout. A LES study by Stevens et al. (2014) shows the same trends and a good agreement with the porous disk measurements. The absolute values of the power improvements are slightly lower for the experiments compared to the LES results. Differences between both studies can explain this discrepancy, for example the slightly larger wind farm spacing and smaller roughness length in the LES study.

3.3 Spatio-temporal correlations

The power output of streamwise aligned turbines is known to be significantly correlated (Stevens and Meneveau, 2014). An improved understanding of this correlation can help explain and quantify the reduction in power fluctuations that is obtained after averaging over multiple turbines. The setup's capabilities to study these spatio-temporal characteristics are verified by analysis of the

[1] A wind farm with all turbines operating in the front row.

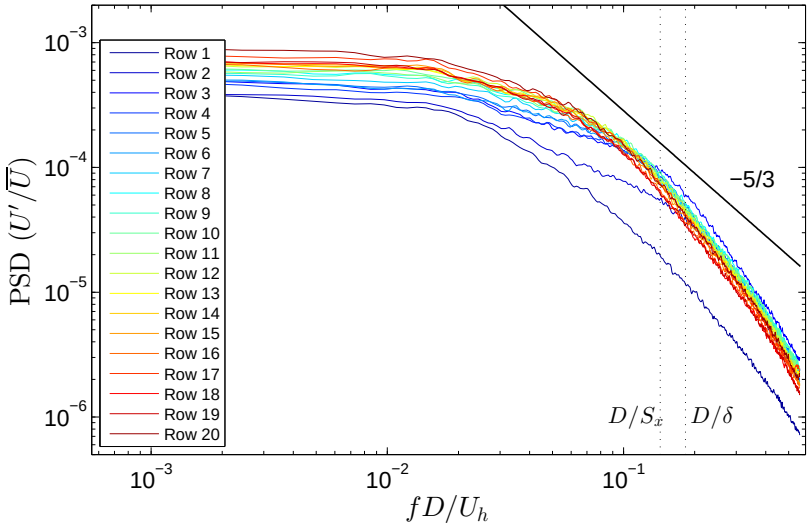

(a)

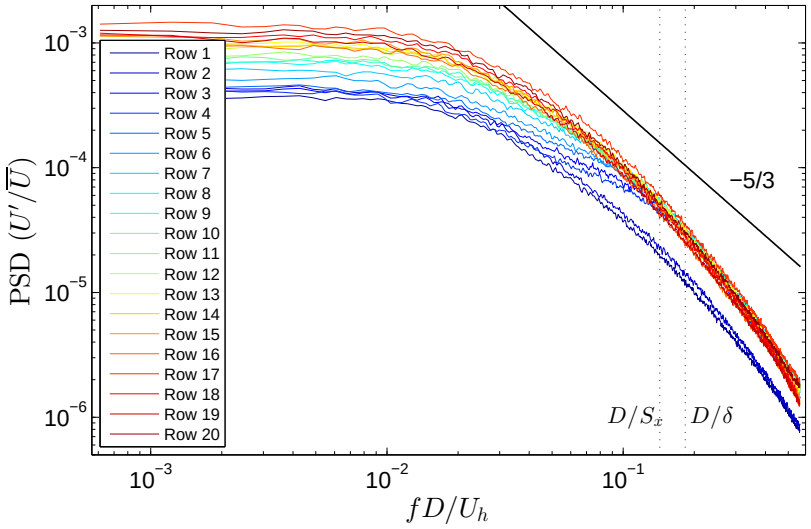

(b)

Figure 3.4: Power spectral density of the reconstructed velocity signals by the porous disk models, for each row in the wind farm. The frequency is normalized by the incoming velocity measured by the first row and the disk diameter.

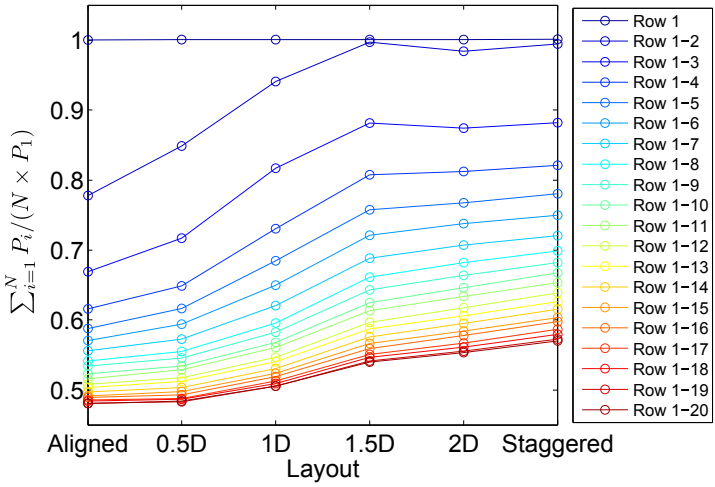

Figure 3.5: Total reconstructed wind farm power ($\sum_{i=1}^{N} P_i$) as a function of wind farm layout and the number of rows. The total power is normalized by the average surrogate power of a porous disk in the first row P_1, times the number of porous disk models N.

turbine-to-turbine cross correlation of the surrogate power output. Figure 3.6 shows the correlation coefficients for the surrogate power of every model in the three central columns with the power of the central model in the first row, as a function of time delay. Each column is given a different color to visualize the correlation in the spanwise direction.

The results shown in figure 3.6 (a), for the aligned layout, confirm a strong correlation with a corresponding time delay in the streamwise direction and small correlations in the spanwise direction. The time delay between peaks in high correlation is representative for the convective travel time of the velocity fluctuations between rows. The streamwise correlation is qualitatively significant up to ten rows.

Figure 3.7 compares the measurements with the results in figure 8 (a) from Stevens and Meneveau (2014) obtained from LES. A qualitatively good agreement is found, confirming the setup's capabilities for studying features of the spatio-temporal characteristics of wind farms.

As shown in figure 3.6 (b), shifting the even rows reduces the correlation for the shifted models, as the spanwise distance increases. The aligned models see an increase in correlation, as there are now less models located directly

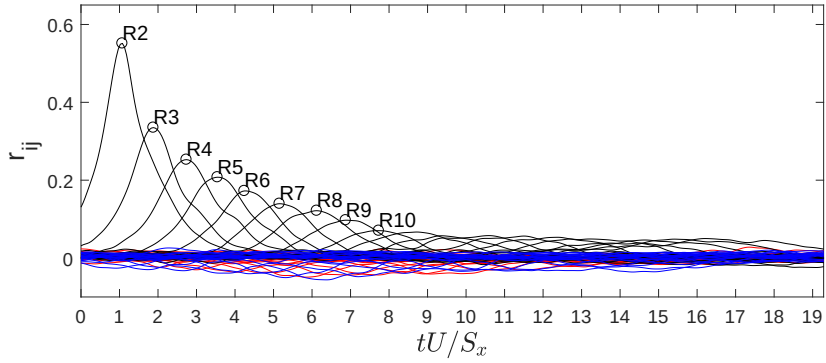

(a)

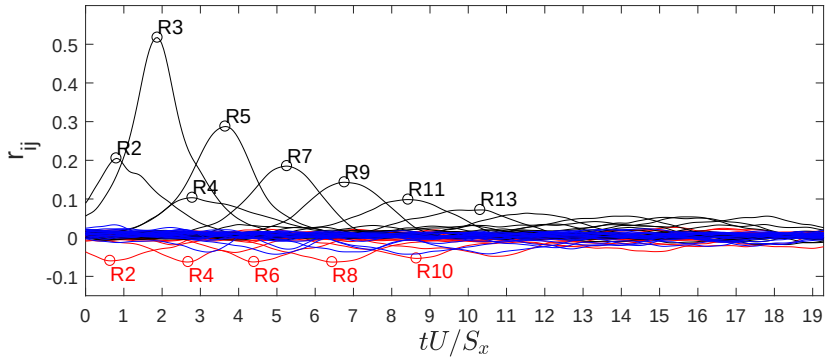

(b)

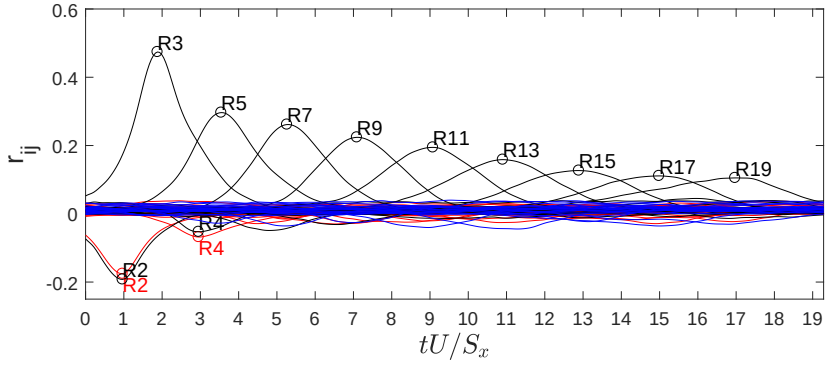

(c)

Figure 3.6: Cross-correlation of the reconstructed power output of every porous disk with the porous disk in the first row and central column, for an aligned layout (a), a $1D$ spanwise shift of the even rows (b) and a staggered layout (c). Colors indicate the different columns, according to figure 2.3. Time is normalized by the streamwise model spacing S_x and the mean velocity measured by the models in the first row.

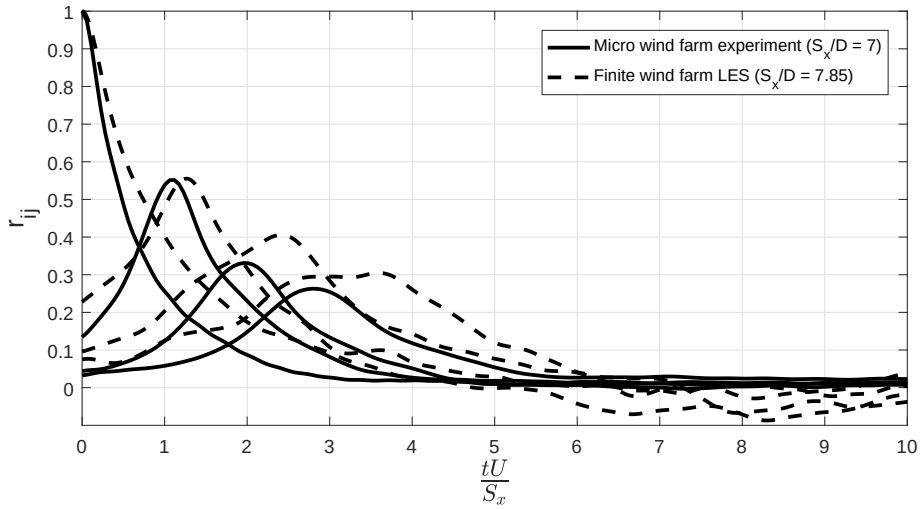

Figure 3.7: Comparison of the measured spatio-temporal correlation with results for a LES of a finite wind farm from Stevens and Meneveau (2014). The authors provided the LES correlation data for this comparison.

upstream to de-correlate the flow. For the staggered layout, streamwise aligned models show a significant correlation to the end of the wind farm, spanning ten consecutive rows. Staggered models on the other hand, show an anti-correlation over a small number of rows.

A strong streamwise correlation of the streamwise velocity fluctuations and a smaller anti-correlation ($r \approx -0.2$) in the spanwise direction have been measured before for a turbulent boundary layer (Ganapathisubramani et al., 2005; Hutchins and Marusic, 2007). These characteristics have been connected to the presence of long meandering streamwise vortices and elongated features in the logarithmic region of a turbulent boundary layer. Ganapathisubramani et al. (2005); Hutchins and Marusic (2007) found the spanwise location of the anti-correlation to be close to half the boundary layer thickness, at a height between $z/\delta = 0.15 - 0.5$ in the turbulent boundary layer. The spanwise spacing for the staggered wind farm layout is $2.5D = 0.075\,\mathrm{m}$, which is indeed approximately half of the boundary layer height: $\delta/2 = 0.08\,\mathrm{m}$.

In figure 3.8, wind farm measurements of sixty-five different layouts (see chapter 4) are used to map the maximum spatial correlation of the velocity measured by each porous disk. It is assumed that the spatial correlation is symmetric in the spanwise direction, Δy, to increase the number of measurement locations, which are indicated by the black points. The resulting 2–D map shows the strong

streamwise correlation and an anti-correlation at $\Delta y/\delta_{99} = \pm 0.5$ as described before, and in good agreement with the structure of a turbulent boundary layer (Ganapathisubramani et al., 2005; Hutchins and Marusic, 2007). However, the measured spatial correlation map is less smooth, as the presence of the porous disk models and their turbulent wakes increase decorrelation. The layout of the wind farm thus influences in some degree the spatial correlation of the flow.

We conclude that the measured correlations show a good agreement with the observations made for a turbulent boundary layer (Hutchins and Marusic, 2007). In a future study it should be studied how the presence of wind turbines or porous disk models in a boundary layer influence the correlation or de-correlation of the flow.

3.4 Velocity and turbulence intensity

In this section we extend the validation with a comparison between wind farm and hot-wire measurements. The horizontal velocity component, in a vertical (X–Z) plane through the central column of the wind farm (see figure 3.1), was measured for two layouts: aligned and staggered. The measurements were performed with an in-house built one-component hot-wire probe, and positioned in each measurement point with an in-house built automated traversing system. The measurement plane covers the first ten rows. The acquisition was done with a TSI IFA-300 Constant Temperature Anemometer hot-wire system and a PCI-PD2-MFS-8-1M/12 data acquisition card. The velocity in each point was acquired for 50 seconds at a sampling frequency of 10kHz and filtered with an analog low pass filter of 5kHz. The data were acquired over several independent measurement series, and matched together based on a reference pitot measurement in the freestream. These pitot measurements where also used during each measurement to regularly recalibrate the hot-wire probe (Talluru et al., 2014). Contours of the mean velocity and turbulence intensity ($TI_u = \sqrt{\overline{u'^2}}/U_0$ are shown in figures 3.9 and 3.10, with U_0 the freestream velocity, $u^{'}$ the velocity fluctuation and the temporal mean denoted with the overline, such that: $u = \overline{u} + u^{'}$. The blockage ratio of the wind farm is small, e.g. the ratio of frontal area covered by porous disk models to the area of the cross section in the wind tunnel is 0.4% for an aligned layout and 0.8% for a staggered layout, so that we do not expect significant blockage effects.

The mean streamwise velocity contours indicate the presence of wakes behind the porous disk models. For the staggered layout, it can be seen how the wakes can recover more fully before they reach the next row, due to the larger streamwise spacing. The contour plots of streamwise turbulence intensity show

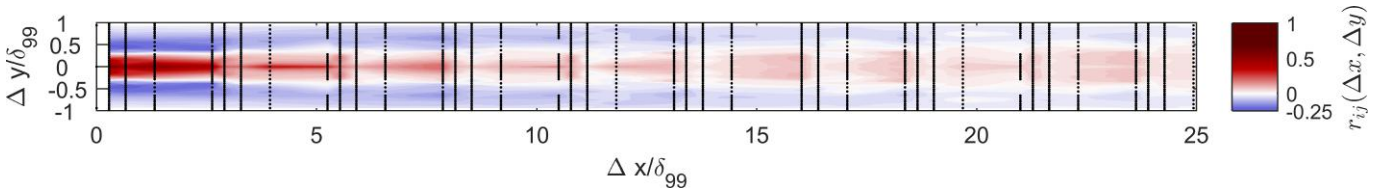

(a)

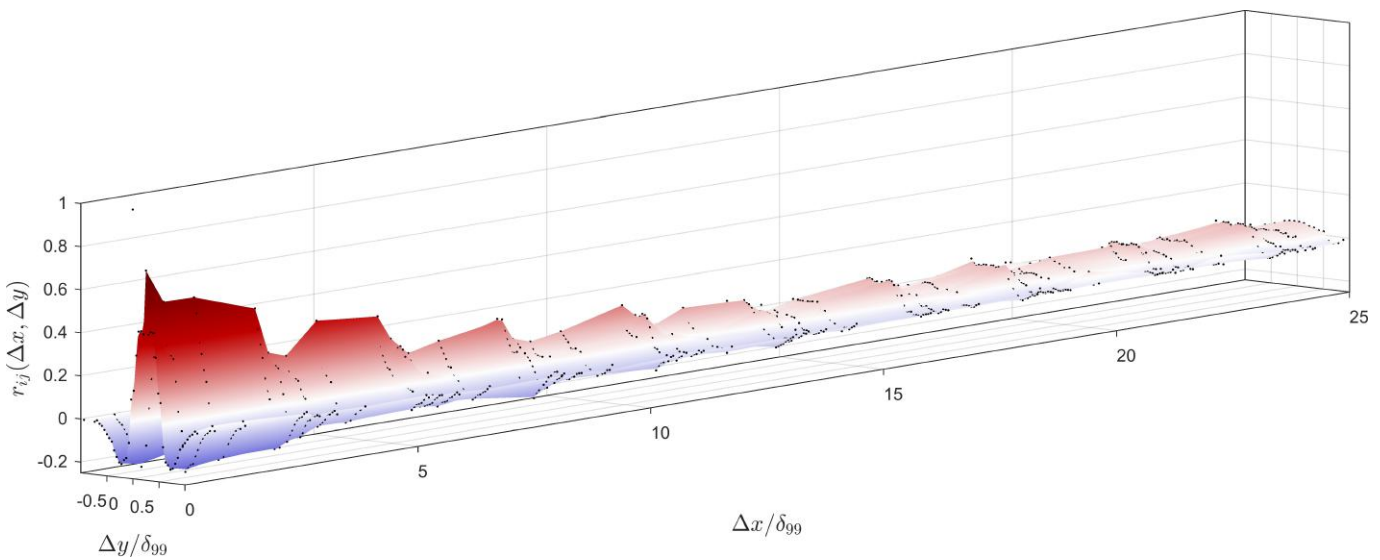

(b)

Figure 3.8: Map of the spatial correlation of the porous disk velocity, as collected from wind farm measurements for fifty-six different layouts.

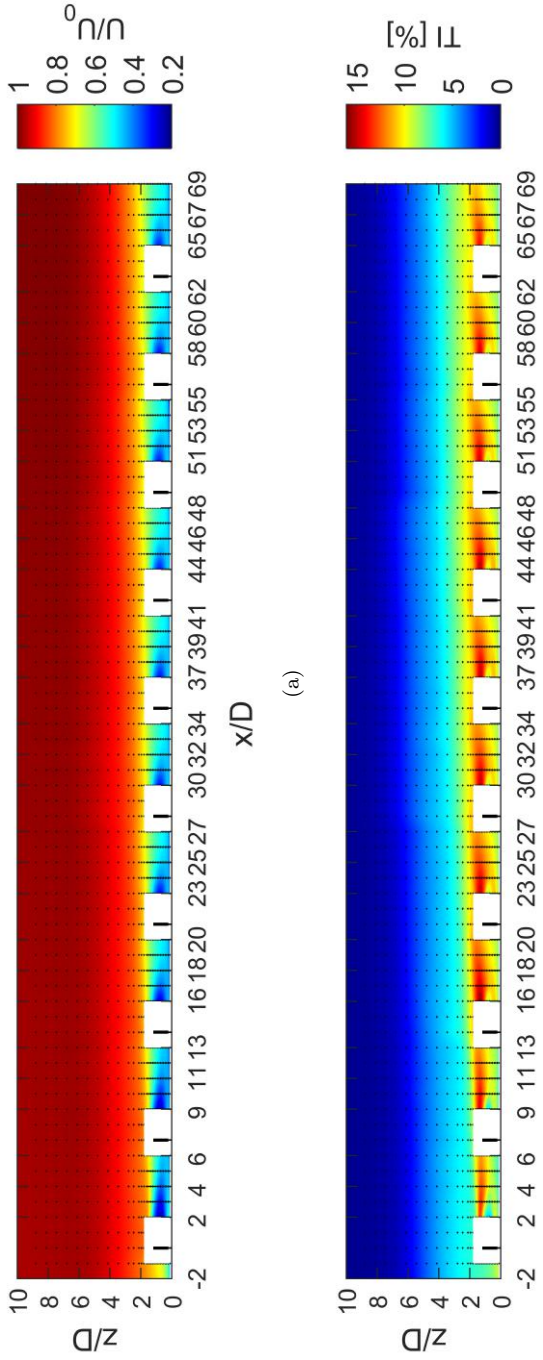

Figure 3.9: Hot-wire measurements of the mean streamwise velocity (a) and turbulence intensity (b) for an aligned layout

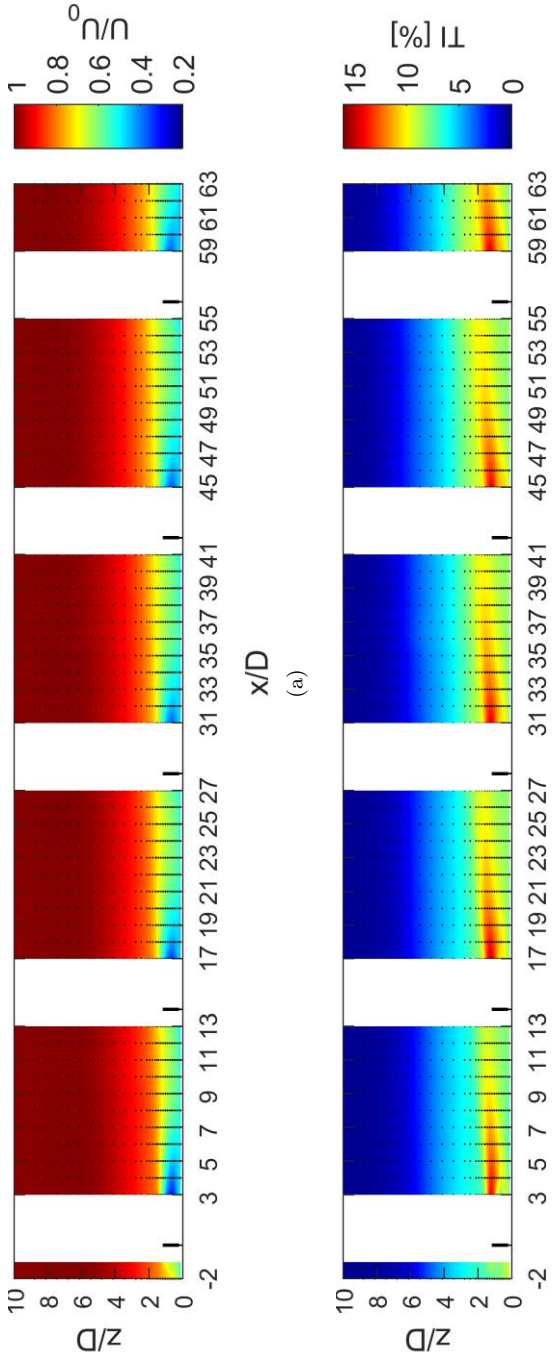

Figure 3.10: Hot-wire measurements of the mean streamwise velocity (a) and turbulence intensity (b) for a staggered layout.

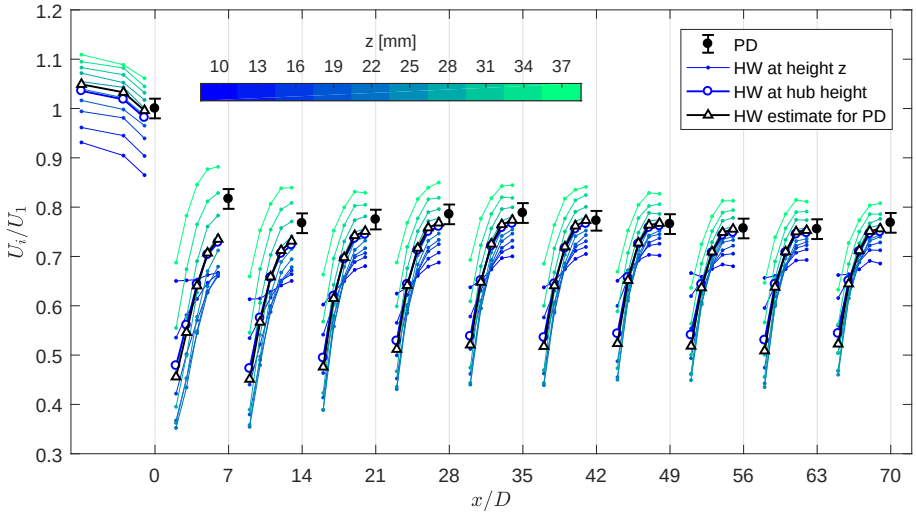

(a)

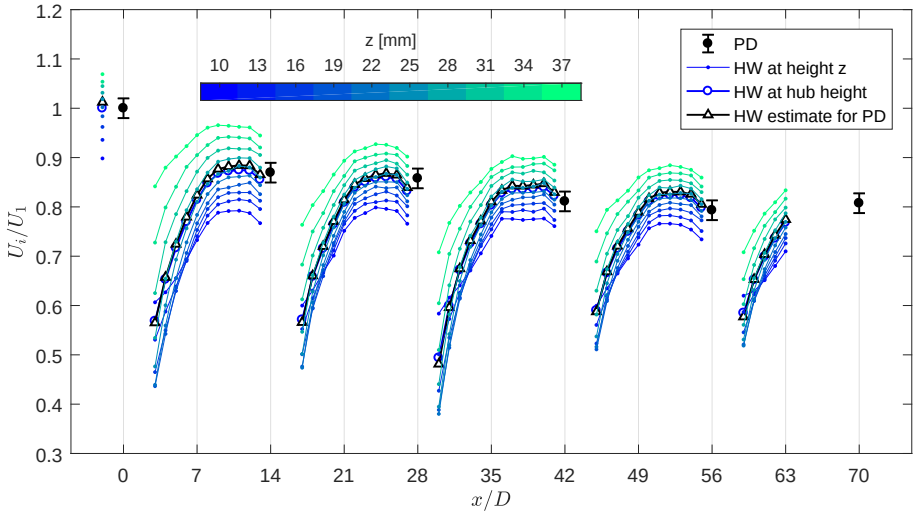

(b)

Figure 3.11: Comparison of the hot-wire measurements (HW) of the mean streamwise velocity with the spatially averaged velocity estimated by the porous disk models (PD) for an aligned (a) and staggered (b) layout. For comparison, the spatially averaged velocity measured by the porous disk models is estimated from the hot-wire measurements with equation 3.1.

the highest values in the shear layer at the top-height of the porous disk models. At the bottom of the porous disk models a small peak is observed. The wake is the strongest after the first row. Further downstream, the wake recovery increases thanks to the higher levels of turbulence, caused by the wakes. These results are qualitatively in good agreement with experimental (e.g. see figure 1.6) and numerical studies of rotating wind turbine models (Chamorro and Porté-Agel, 2011; Chamorro et al., 2011; Wu and Porté-Agel, 2013).

The hot-wire measurements are compared with the porous disk results in figures 3.11 and 3.13. Because of the velocity shear in the boundary layer, the spatially averaged measurements by the porous disk models cannot be directly compared to a specific point measurement from the hot-wire probe. All single point hot-wire measurements are shown for a height range that covers $z_h - D/2 \leq z \leq z_h + D/2$. Here z_h is the hub height of the porous disk model, D the diameter and R the radius.

The hot-wire velocity is normalized by the velocity measured at hub height and $2D$ upstream of the first wind turbine. For the aligned case, the normalization velocity was taken as the average of the measurements at an upstream location of $1D$ and $3D$, as no measurement data was available at a location of $2D$. The porous disk velocities are normalized by the velocity measured by the first model in the farm. The hot-wire measurements visualize the wake recovery. The results for the staggered layouts show a decrease of the velocity in front of each porous disk model, which is not observed for the aligned layout, except for the first row.

A good agreement is observed between the porous disk models and the hot-wire data at hub height. However, the porous disk velocity in the second and third row of the aligned layout is significantly higher. The velocity shear may cause this difference, as a porous disk measures the force, which scales with the square of the velocity. Higher velocities can thus have a larger impact. Furthermore, the porous disk models estimate the force through measuring the moment, a distribution of the force over the disk can thus lead to a measurement offset of $+1\%$ to $+5\%$ (this was estimated by assuming that the local drag force on the disk is given by $dF(\mathbf{x}) = (1/2)\rho C_T U^2(\mathbf{x}) dA$, and by calculating the corresponding bending moment). The effect of velocity shear in the experiment was estimated based on the vertical velocity profiles from figure 3.11. By linearizing and assuming that the velocity is uniform in the spanwise direction, we estimate the spatially averaged velocity measured by the porous disk $\langle U \rangle$ through reconstructing the bending moment relation:

$$\langle U \rangle = \sqrt{\frac{2}{z_h \pi R^2} \int_{z_h - R}^{z_h + R} z U^2(z) \sqrt{R^2 - (z - z_h)^2}\, dz}. \tag{3.1}$$

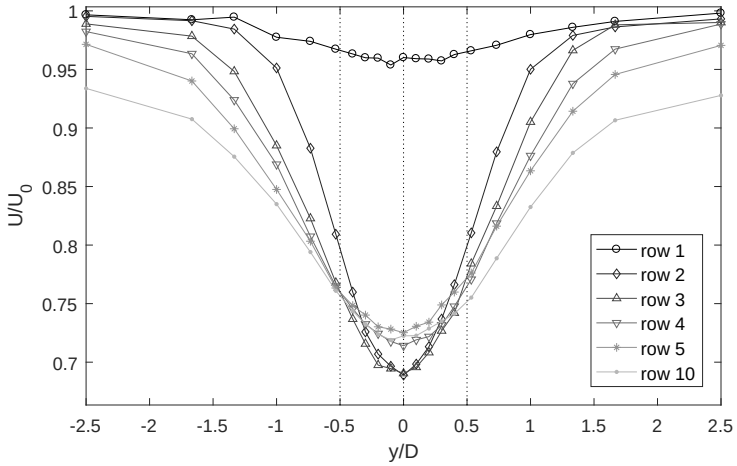

Figure 3.12: Spanwise profiles of the streamwise velocity measured with a hot-wire probe at hub-heigth. The profiles are measured at a distance of $1D$ upstream from each porous disk in the central column of the wind farm. The velocities are normalized by the incoming hub-height velocity U_0, measured $7D$ upstream from the first row.

The estimated velocity from equation 3.1 is slightly higher than the velocity at hub height. However, this difference is small or negligible in most cases, and does not explain the difference for the second and third row.

Figure 3.12 shows a horizontal profile of the streamwise velocity, measured by the hot-wire probe $1D$ upstream from each porous disk in the central column in the wind farm. Especially in front of row 2 and 3, the upstream velocity deficit in the wake is pronounced and the velocity is not uniform in the spanwise direction. Further downstream, the velocity variation over the disk area becomes smaller due to faster wake recovery. The hot-wire velocities shown in 3.11 are measured in the central plane, where the velocity is the lowest, and thus underestimate the porous disk velocities, especially for row 2 and 3. This effect is not noticed for a staggered layout, which is expected because of the larger streamwise spacing with a better wake recovery. For a complete validation, future measurements should measure the velocity in a Y – Z plane upstream of each porous disk, to consider the spatial variation.

Figure 3.13 shows the local turbulence intensity measured by the porous disks and the hot-wire probe. The local turbulence intensity is based on the local velocity of the hot-wire probe, or the spatially averaged velocity from the porous disk. The signal measured by the porous disk is filtered twice, once by a digital low-pass filter (a digital sharp cut-off filter at 200 Hz is applied

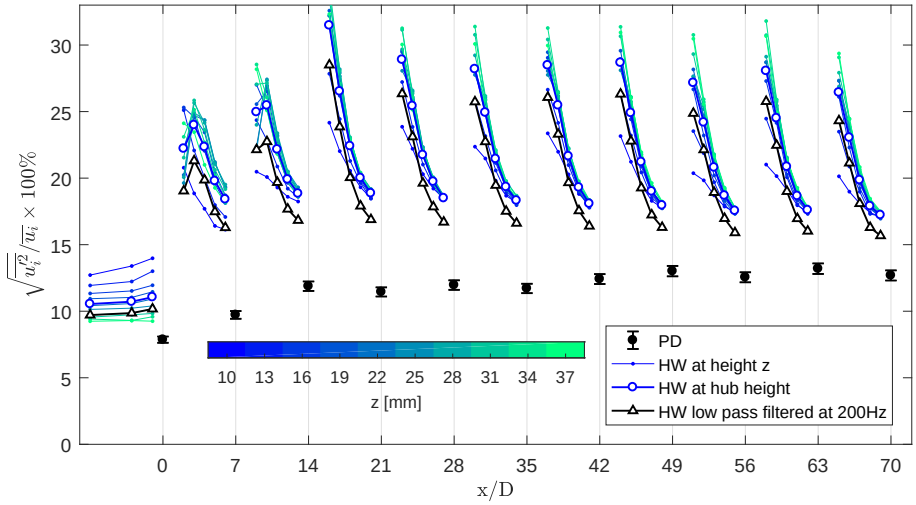

(a)

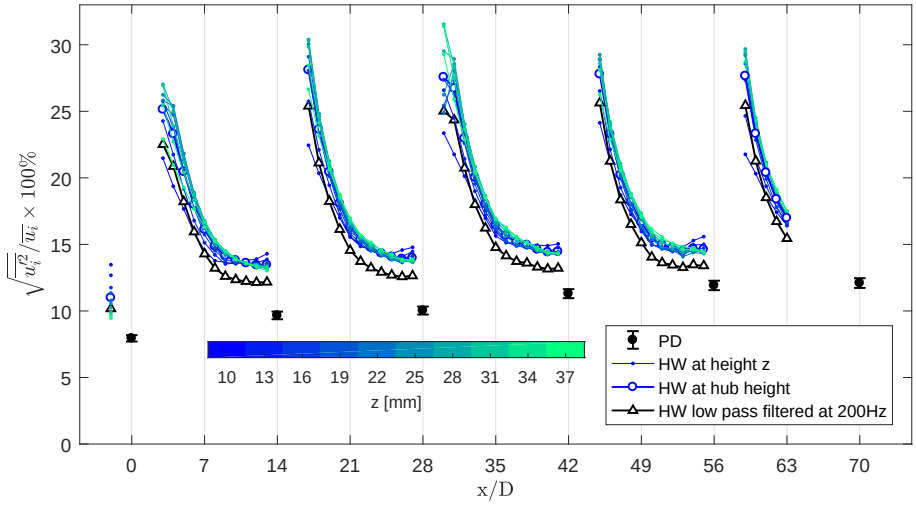

(b)

Figure 3.13: Comparison of the local turbulence intensity, measured by the hot-wire probe (HW), and by the porous disk models (PD) for an aligned (a) and staggered (b) layout.

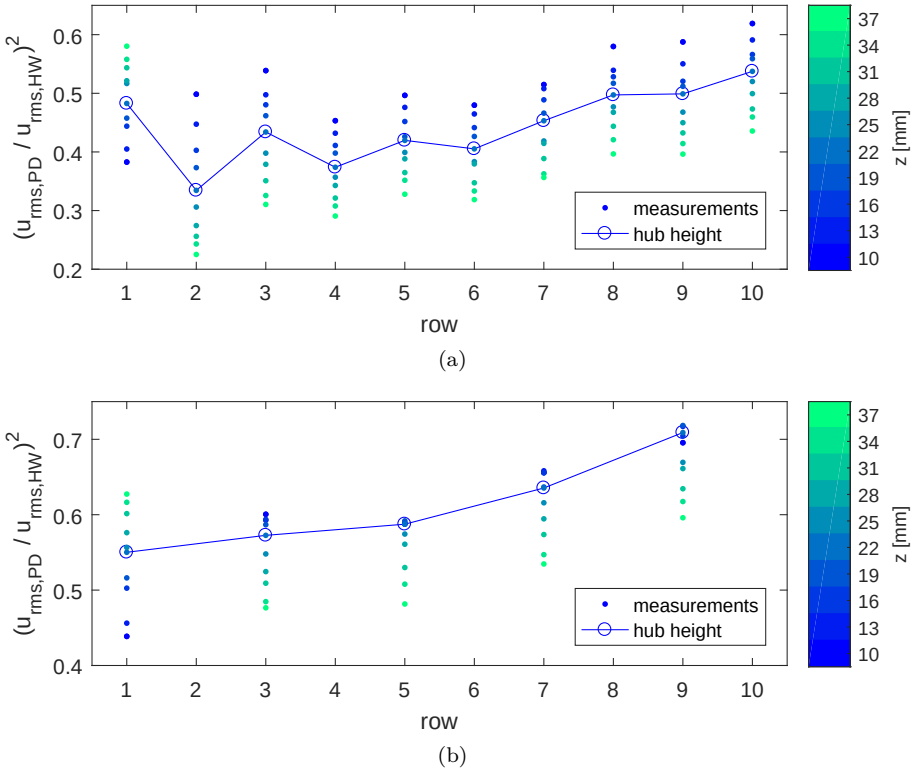

Figure 3.14: The filtered amount of energy of the velocity fluctuations measured by the porous disk models ($u_{rms,PD}$) compared to an upstream hot-wire probe ($u_{rms,HW}$), as a function of row number and height z, and for an aligned (a) and staggered layout (b).

in the post-processing) and once due to spatial averaging over the disk. The porous disk thus measures lower turbulence levels then the hot-wire probe. For comparison, figure 3.13 also shows the turbulence intensity calculated from the hot-wire velocity, after applying a similar sharp cut-off filter at 200 Hz. The turbulence intensity after filtering the hot-wire signals, shown with the black lines, are only slightly lower than the unfiltered levels, indicating that most of the energy-containing fluctuations are found below 200 Hz. The largest part of the spectral filtering for the porous disk is thus a result of the spatial averaging over the disk which reaches up to lower frequencies.

The amount of filtered energy depends on the original spectrum of the velocity fluctuations, and not only on the filter transfer function. As shown in figure 3.4, the wake downstream from the first row of an aligned layout contains

significantly more energy at higher frequencies, where the spatial filtering is more severe. For the aligned layout, more high frequency spectral energy is thus filtered by a porous disk in row 2, than in row 1 or far downstream, where the spectral energy is spread over a broader range of frequencies (figure 3.4). The changing shape of the velocity spectrum as the flow develops explains why the turbulence intensity measured by the porous disk models increases much slower, reaching a plateau after eight rows, while the turbulence intensity measured by the hot-wire, levels off after approximately three rows.

By comparing the spectra from the hot-wire measurements with the spectra from the porous disk, we have estimated the amount of energy filtered in each row, as shown in figure 3.14. Different hot-wire measurement points are colored by height. For the first row of the aligned and staggered layout, it can be seen how the filter effect is smaller compared to the spectrum of a hot-wire point that is located higher (e.g. the top-height). However, in the second row and more downstream, the opposite is observed. This can be explained by the increased small scale turbulence in the shear layer at the top-height of the porous disk models, which is filtered more strongly by the spatial averaging. Furthermore, as shown in figure 3.12, the velocity field is especially non-uniform in front of row 2 and 3 for an aligned layout, making it difficult to make a correct comparison with hot-wire point measurements. Each hot-wire point is measured separately, such that they are uncorrelated. For a complete validation, it is important to measure both the temporal and spatial fluctuations of the velocity field in front of each porous disk, for instance with PIV.

For the first row of the aligned and staggered layout, the same amount of filtering is expected. However, the results in figure 3.14 show a difference, which can be explained by the difference in location of the hot-wire probe. The hot-wire was located $-2D$ of the first row for the aligned layout, while this distance was only $-1D$ for the staggered arrangement. Due to the local slowdown in front of the porous disk, the estimated amount of filtered energy is lower for the staggered layout. The filtered energy loss is smaller for the staggered arrangement, as the streamwise spacing is larger, the wakes recover more, and the spectrum of the velocity for the downstream porous disk contains less high frequency fluctuations.

These results indicate the importance of knowing both the spatial filter and the shape of the original spectrum, if the spatially averaged thrust values from a porous disk, or the power measurements from a real wind turbine, are used to estimate the turbulence intensity of the flow.

3.5 Conclusions

A surrogate for the power output, the spatially averaged velocity and its turbulence intensity have been measured with the micro wind farm experimental setup. Measurements for six different layouts, ranging from aligned to staggered, match the main trends described in the literature. For an aligned wind farm the surrogate power drops quickly after the first row, leveling off at a value of $P_i/P_1 \approx 0.45$. This is slightly lower, but in reasonably good agreement with field data from the Horns Rev wind farm, considering the differences in wind farm layout and boundary conditions. For a staggered layout, the surrogate power increases mainly in the beginning of the wind farm, while the improvement at the end is much smaller, in good agreement with LES results by Stevens et al. (2014).

The model's capabilities for measuring the spatio-temporal characteristics have been used to study the cross-correlation of the power outputs. Streamwise aligned porous disk models show a high correlation, confirming results in the literature (Stevens and Meneveau, 2014). An anti-correlation was observed for staggered porous disk models, showing a good agreement with measurement results for a turbulent boundary layer (Hutchins and Marusic, 2007).

Detailed measurements of the streamwise velocity were performed for an aligned and staggered wind farm. The hot-wire measurements indicate that although the porous disk models do not perfectly match the detailed near-wake features of a wind turbine, the overall wake characteristics, recovery and boundary layer interaction, with the presence of a strong shear layer at the top-height of the models, is in qualitative good agreement with experimental and numerical results for wind farms. Considering the measurement uncertainty related to the strain gage measurements, we conclude that the setup is able to estimate the forces on the porous disk models and the corresponding incoming spatially averaged velocity. The frequency response of the measurements makes it possible to estimate the unsteady loading of the porous disk models. By taking into account that these signals are spatially filtered, it is possible to use them as a first estimate for the turbulence intensity of the flow.

Chapter 4

Study of wind farm layout

Optimization studies of wind farm layout are based mainly on simplified analytical models (Lackner and Elkinton, 2007; Meyers and Meneveau, 2012; Chowdhury et al., 2012), and have indicated that increasing the streamwise spacing is more beneficial than the spanwise spacing (Chen et al., 2013; Bokharaie et al., 2016). Studies of large wind farms with LES have confirmed these conclusions (Yang et al., 2012; Stevens et al., 2016b). Yang et al. (2012) reasoned that the wake expansion, or transverse interaction, is limited, while it is mainly the wake region that introduces vertical shear and transport to benefit wake recovery. As a result, layouts with a too large spanwise spacing make less efficiently use of the surface area they occupy. To improve wind farm efficiency, one should thus place the wind turbines closely together in the spanwise direction, and make the streamwise spacing as large as possible (Bokharaie et al., 2016). In another experimental study, McTavish et al. (2014) showed the benefit of placing a wind turbine slightly downstream, in between two other wind turbines, to take advantage of the local flow acceleration.

Based on LES of six different layouts, Archer et al. (2013) studied the power output for a finite wind farm. In their study, the staggered layout was found to produce the highest power output, showing good agreement with the wind tunnel experiments of an aligned and staggered wind farm (Chamorro and Porté-Agel, 2011; Chamorro et al., 2011). These measurements highlighted a strong effect of layout on the flow properties, by showing lower turbulence levels, and a slower development of an internal boundary, and equilibrium layer, for the staggered layout. Stevens et al. (2014) further investigated the effect of turbine alignment with the wind direction, on the power output of a finite farm. Their study showed that an alignment angle smaller than fully staggered

can result in an overall higher power output, indicating that a staggered layout is not necessarily the most optimal. Interestingly, while the layout influences significantly the power of the first few rows, the LES results by Stevens et al. (2014, 2016b) show only a small difference after ten rows. This asymptotic behavior indicates the appearance of a fully developed regime in large farms, also referred to as the infinite wind farm regime. There, a balance takes place between the vertical transfer of mean kinetic energy, and the power extraction by the wind turbines. Experimental (Cal et al., 2010) and numerical studies (Calaf et al., 2010) have verified this balance by showing that the power extraction by the turbines is of the same order as the vertical transport of mean kinetic energy. Therefore, in the infinite regime, the mean power does not change anymore from one row to the next. For relatively small spanwise spacings (e.g. smaller than $S_y/D \approx 6$), Yang et al. (2012); Stevens et al. (2016b) found only a small effect of arrangement on the power in the fully developed regime, however data is only available for a limited number of layouts.

In this chapter, we employ the micro wind farm for a parametric study of layout, in an attempt to find an optimal configuration for a maximal surrogate power and a minimal unsteady loading. With these measurements we aim at providing a large set of experimental data, for many different layouts, that can be used for validation purposes. Based on the observations in the literature we study layouts that explore especially large and non-uniform streamwise spacings, in an attempt to increase the overall power.

In section 4.1 the experimental setup is described. The wind farm measurements of surrogate power and turbulence intensity are presented for each case in section 4.2. In section 4.3 a layout-comparison is presented as function of the overall farm efficiency, and the efficiency in the fully developed regime. In the final section conclusions are presented about the influence of layout on the power and unsteady loading, and the most optimal layout is selected from our experiments.

4.1 Experimental setup

For the experiments in this chapter, the micro wind farm is used, as documented in chapter 2 and validated in chapter 3. In the experiments, the instantaneous forces on all sixty porous disk models in the three central columns are measured for each layout. The surrogate power output and turbulence intensity are estimated as explained in chapter 2, by making use of momentum theory, and by focusing on the below-rated operating regime of a wind turbine, for which the thrust coefficient is approximately constant and the blades are not stalled. The turbulence intensity is thus directly representative for the unsteady loading

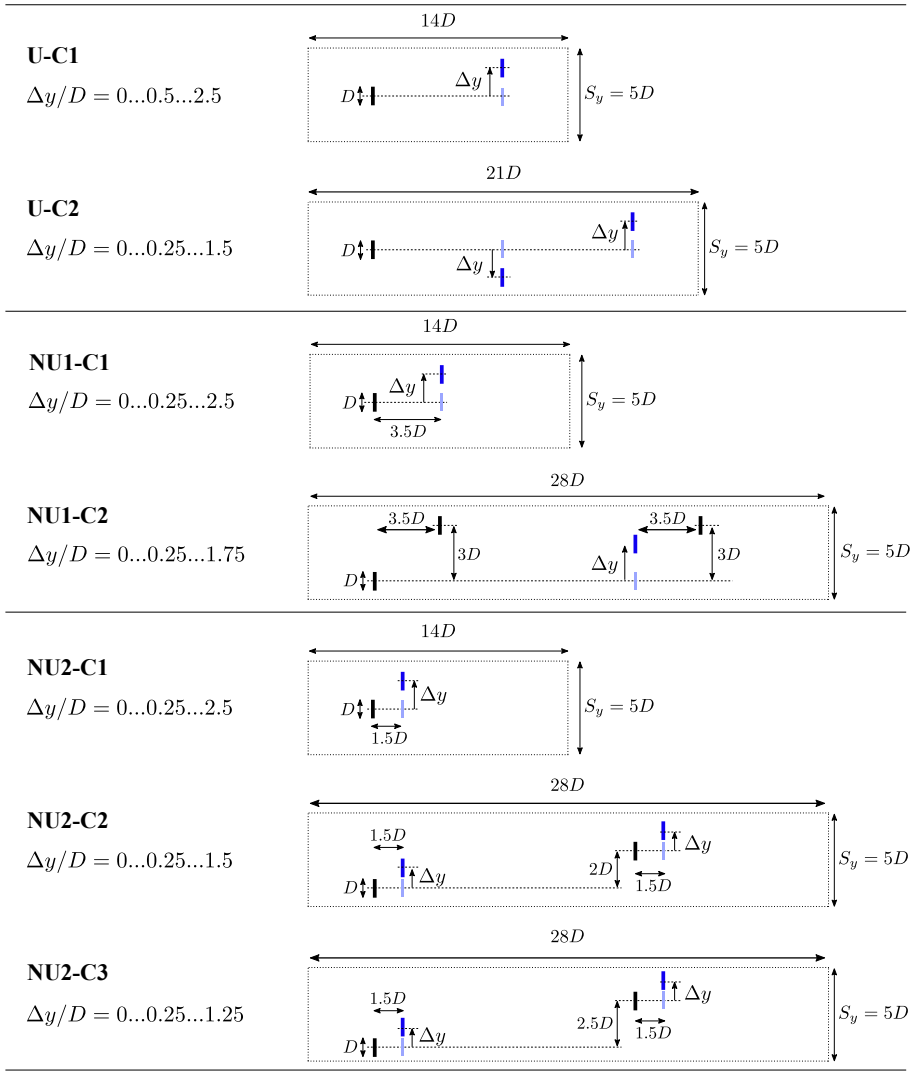

Figure 4.1: An overview of the studied wind farm layout patterns. Each series consists of a number of layouts, by sliding the indicated (blue) porous disk models in the spanwise direction, over the specified range for Δy.

of the porous disk models. It is important to note that the measured variance represents the large scale fluctuations, i.e. integrated over the disk. These fluctuations are representative for the tower bending loads. It is important to note that the blades of an actual wind turbine will encounter an increased unsteady loading due to rotation and smaller scale turbulence. The turbulence intensity is here defined as $TI = \sqrt{u'^2}/U_{h,i}$, with $U_{h,i}$ the mean hub height velocity in row i measured by the porous disk models. In chapter 3 it was shown that the spatial averaging over the disk filters on the order of 50% of the spectral energy, such that the turbulence intensity values from the porous disks are a rough estimate for 70% of the actual local turbulence intensity.

For each layout the same area is occupied in the wind tunnel, so that the area-density of porous disk models is constant, e.g. an area of $7D \times 5D = 35D^2$ for each porous disk model. The wind farm arrangements are configured by changing the intermediate streamwise spacing, and by sliding rows in the spanwise direction. It is noted that the spanwise spacing between models in each row is always $S_y/D = 5$. An overview of the studied layouts is given in figure 4.1. A layout with a zero spanwise shift, is referred to as 'aligned', and a layout with a maximal spanwise shift is referred to as 'staggered'.

The first series of layouts considers a uniform streamwise and spanwise spacing. For this layout series, two cases are considered. The first case, *U-C1*, consists of six layouts (earlier presented in chapter 3), which range from aligned to staggered, by sliding the even rows in steps of $0.5D$. The second case, *U-C2*, considers double staggering, for which each third row is slided in the other direction than each second row.

The second layout series consists of an uneven streamwise spacing which alternates between $S_x/D = 3.5$ and $S_x/D = 10.5$. Again two cases are considered. The first case, *NU1-C1*, follows the original approach of varying an aligned layout to a staggered configuration, by sliding the even rows. The second case, *NU1-C2*, only moves the third row in a pattern of four rows, while the other rows are shifted with a distance of 3D compared to the first row.

The third layout series considers a more extreme non-uniform streamwise spacing, which alternates between $S_x/D = 1.5$ and $S_x/D = 12.5$. Three cases are considered, for which the first, *NU2-C1*, follows again the original aligned to staggered approach. The second case, *NU2-C2*, repeats a pattern of four rows, for which the first two rows together are staggered with a distance of $2D$ compared to the last two. The even rows are moved in steps of $0.25D$. The third layout case, *NU2-C3*, follows a very similar approach, but now the first and third row are exactly spaced $2.5D$ in the spanwise direction.

The acquisition parameters for the strain gage measurements are the same as

documented in chapter 3. For all layouts, the measurement time is more then 3×10^4 times the integral time scale of the incoming flow (e.g. $\approx 9\,\text{ms}$), such that very well converged statistics are reached (see chapter 2).

4.2 Wind farm measurements

In this section the wind farm measurement results are presented. First the layouts with a uniform streamwise spacing are discussed. Then the benefits of a moderate (*NU1*), and a more extreme (*NU2*) non-uniform streamwise spacing are presented.

4.2.1 Uniform spacing

Figure 4.2 presents the results for the first two layout series, *U-C1* and *U-C2*. The first series represents the change of a regular array, from aligned to staggered. When the layout is fully aligned, the mean row power reduces quickly, and after approximately three rows it levels off to a constant value of $P_i/P_1 \approx 0.45$. These power losses are the same order of magnitude as the losses of 45% in the Horns Rev wind farm (Barthelmie et al., 2011) with a similar streamwise spacing, almost 50% in the Walney 2 wind farm with also a similar streamwise spacing (Nygaard, 2014), or more than 60% observed in the Middelgrunden offshore wind farm (Barthelmie et al., 2007) with a very close spacing. When the layout is changed from aligned to staggered, the surrogate power increases mainly for the first ten to fifteen rows, indicating a slower move towards a fully developed regime. Interestingly, at the end of the wind farm, little differences are seen compared to the aligned configuration, so that it seems that both layouts tend to the same asymptotic limit.The staggered layout results in the highest total farm surrogate power output. Furthermore, when staggered, the first two rows measure approximately the same surrogate power and turbulence intensity, indicating that the second row sees approximately an unperturbed free stream flow.

For every layout, it is noticed that the last row consistently measures a higher surrogate power. It is possible that this offset is related to its location, very close to the end of the wind tunnel test-section. There, the cross-section makes a slight contraction. Another possible cause could be a wind farm end-effect, similar to the pressure interactions as observed for a close group of cyclists (Blocken et al., 2013). However, for the layout *NU2-C1*, where the last row is shifted $5.5D$ upstream, the effect of a higher mean power for the last row has reduced significantly. This observation supports the first hypothesis. To

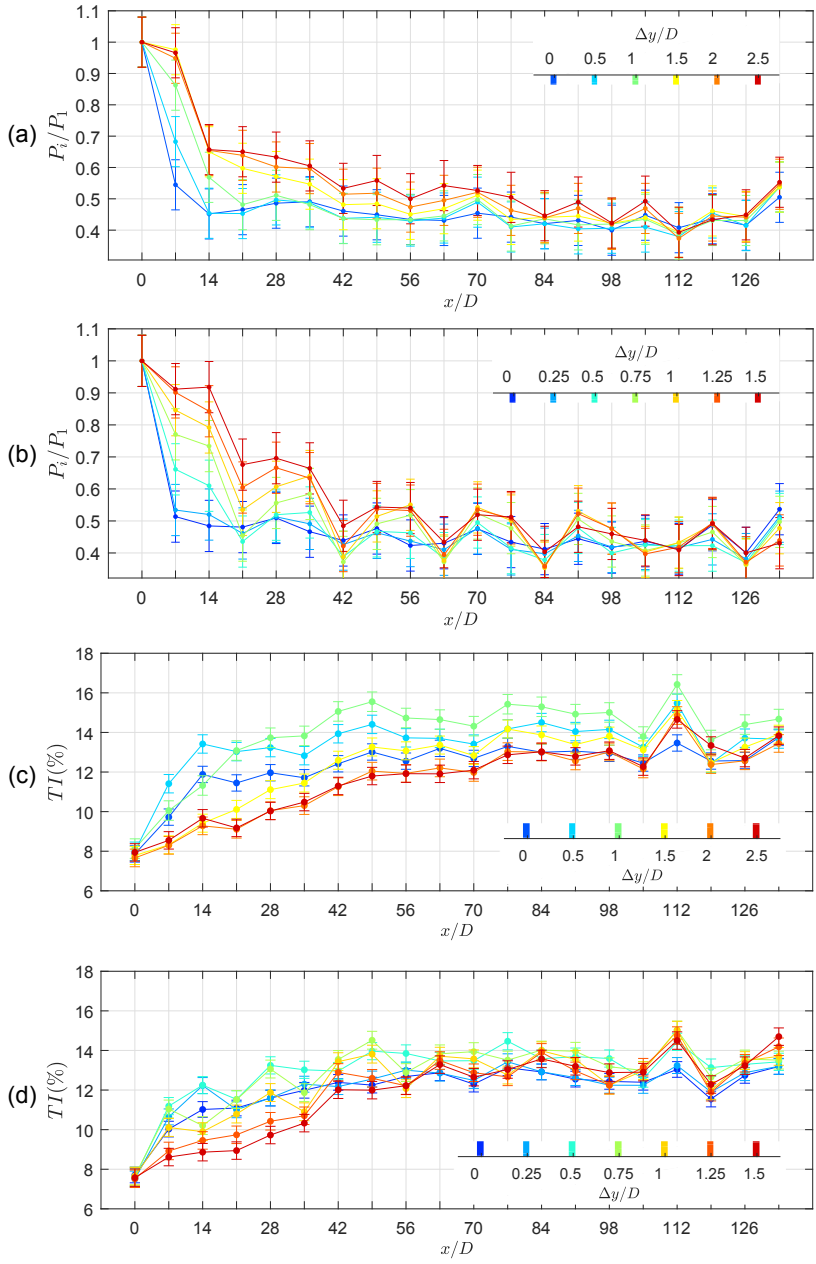

Figure 4.2: Wind farm measurements of the mean surrogate power in each row (a-b) and estimated local turbulence intensity (c-d), for the *U-C1* (a,c) and *U-C2* (b,d) layout series. See figure 4.1 for an overview of the layouts.

exclude this effect from the analysis, we do not include the last row when we study the asymptotic behavior in section 4.3.

The mean power for the *U-C2* layouts show the same trends. By shifting the rows to a double staggered configuration, the surrogate power increases mainly in the first ten-to-fifteen rows. However, the increase in the first half of the wind farm is larger than before. Within the measurement uncertainty, it is possible to recognize a pattern for each three consecutive rows, as a consequence of the repeating layout. The second and third row of the wind farm, show almost the same surrogate power as the first row. Further downstream, it is the rows that are not moved, i.e. the first row in each pattern of three, that show the lowest surrogate power, or largest wake losses.

Because it is impossible to accommodate the three-row pattern until the end of the twenty-row wind farm, the last two rows were kept unchanged in the aligned configuration. The thereby increased wake effects explain the lower power for the last two rows. In the last part of the wind farm, the pattern is also more difficult to distinguish, which could be a result of the measurement uncertainty. Qualitatively, both layouts, *U-C1* and *U-C2*, tend to the same asymptotic limit in the fully developped regime.

The unsteady loading as measured for *U-C1* and *U-C2* is shown in figure 4.2 *c-d*. For the aligned layout, the turbulence intensity increases fast in the first three rows, and eventually levels off after approximately twelve rows. This trend indicates that while the power levels off quickly, the flow is still developing until the twelfth row. The staggered layout results in a smaller unsteady loading, which increases more slowly with row number, but eventually reaches the same level as the aligned layout at the end of the wind farm, e.g. $TI \approx 13\%$. It is interesting to note that while all layouts tend to the same mean power asymptote, the unsteady loading shows different asymptotes, with higher values for *U-C1* layouts with a spanwise shift smaller than $1D$. In these cases the porous disk models have a partial wake overlap which is expected to cause the higher variability. These slightly-shifted layouts are thus not preferred, as they result in a below-optimal power output and the highest level of unsteady loading.

The *U-C2* layout-series shows similar trends for the unsteady loading. The double staggered layout results in a similar slow increase, with at the end also a turbulence intensity of $TI \approx 13\%$. In this case, the intermediate layouts only result in a slightly higher unsteady loading, thanks to the increased streamwise spacing of a double staggered approach. The consistent peak value of the turbulence intensity in row 17 is expected to be caused by a measurement error.

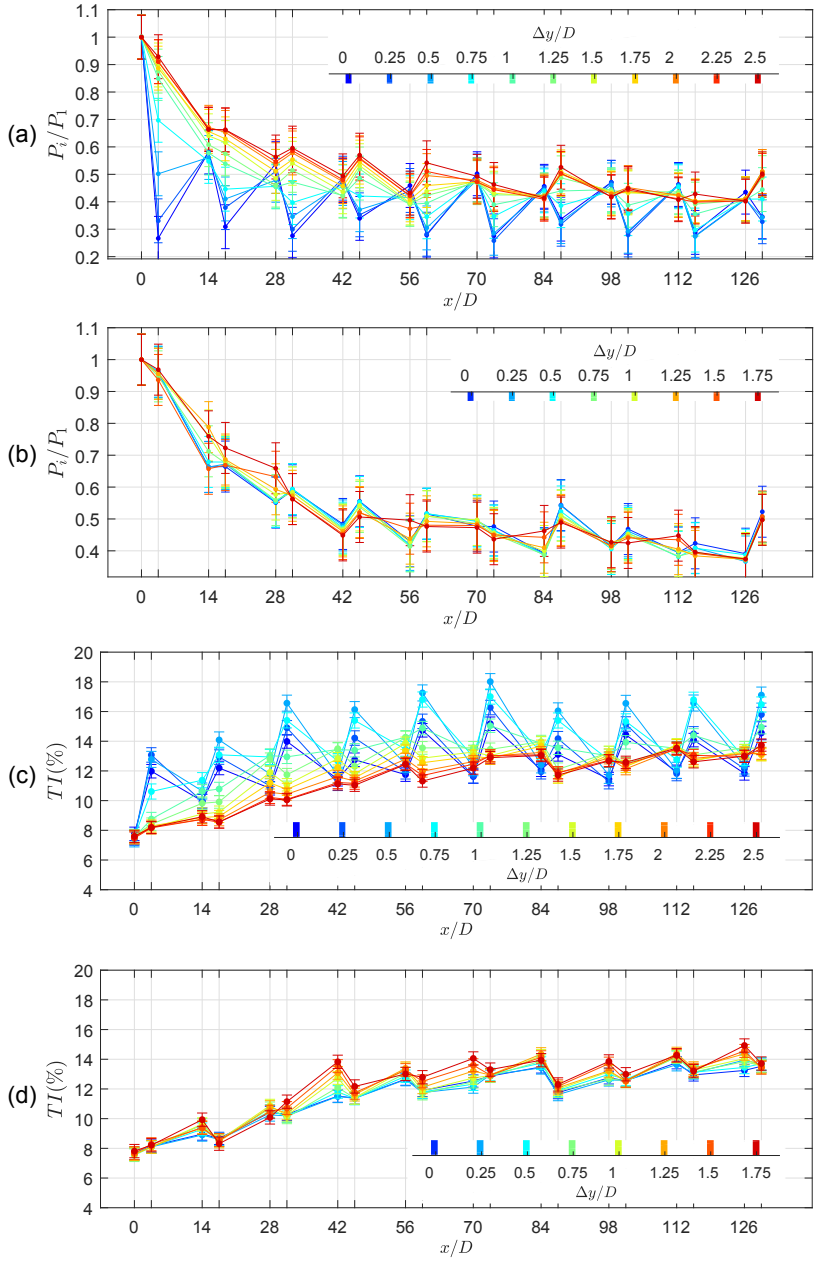

Figure 4.3: Wind farm measurements of the mean surrogate power in each row (a-b) and estimated local turbulence intensity (c-d), for the *NU1-C1* (a,c) and *NU1-C2* (b,d) layout series. See figure 4.1 for an overview of the layouts.

4.2.2 Moderate non-uniform spacing

The measurement results for the non-uniform layouts series *NU1* are shown in figure 4.3. For an aligned configuration, the disadvantage of a smaller mutual distance (i.e. $S_x/D = 3.5$ instead of $s_x/D = 7$) between half of the rows is clear. Every second row shows a very low surrogate power output and high unsteady loading, indicating clearly their location in the near wake from an upstream model. The rows with a larger upstream streamwise spacing (i.e. $S_x/D = 10.5$ instead of $s_x/D = 7$) do measure a higher power, e.g. $P_3/P_1 \approx 0.6$ compared to $P_3/P_1 \approx 0.45$ for the original aligned layout. However, these improvements do not compensate the significantly lower outputs of the closely spaced models.

By sliding the even rows in the spanwise direction, the impact of wakes is reduced significantly. Most of the improvements are made by shifting from $0D$ to $1D$. Increasing the spanwise shift of the even rows to a fully staggered layout results in the highest surrogate power output. The mean row power for the staggered configuration follows a very similar trend as the previous results for a uniformly spaced staggered wind farm. The surrogate power is the highest at the beginning of the wind farm, and reduces towards an asymptote at the end. Interestingly, the staggered layout shows a repeating pattern for each pair of consecutive rows. The even rows (starting from row 6) which are closely spaced and staggered with the upstream uneven rows, measure a higher surrogate power, which indicates less wake losses, or possibly the presence of a local flow interaction, similar to observed by (McTavish et al., 2014). However, a clear trend is not obvious. As before, the fully staggered layout results in the lowest unsteady loading. The turbulence intensity levels off after approximately 13 rows, reaching a value of $TI \approx 13\%$, similar as the observation for the previous layout series.

The measurements for the *NU1-C2* series show no clear benefits for the power. While the second to fifth row increase for the largest spanwise shift, the power decreases slightly everywhere else in the wind farm. Interestingly, also the unsteady loading of the porous disk models increases with increasing spanwise shift. It is concluded that the *NU1-C2* layout series brings no direct benefits for power output or unsteady loading.

4.2.3 Extreme non-uniform spacing

The measured surrogate power output for the *NU2* series are shown in figure 4.4, and the estimated turbulence intensity is shown in figure 4.5. This layout series pursues an extremely uneven streamwise spacing. As a result, the even

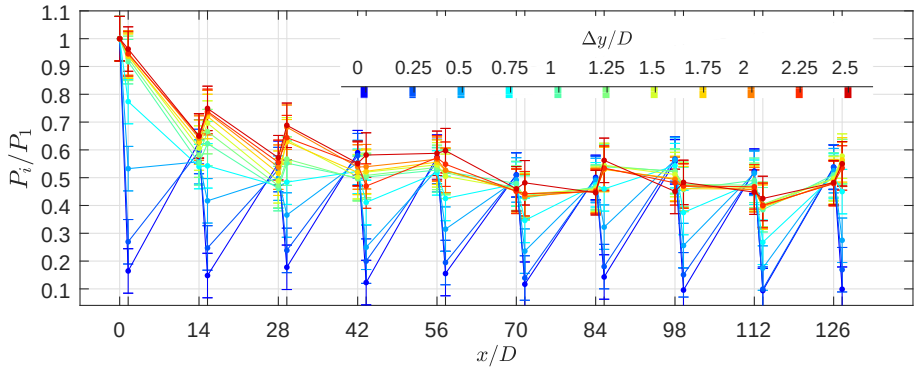

(a)

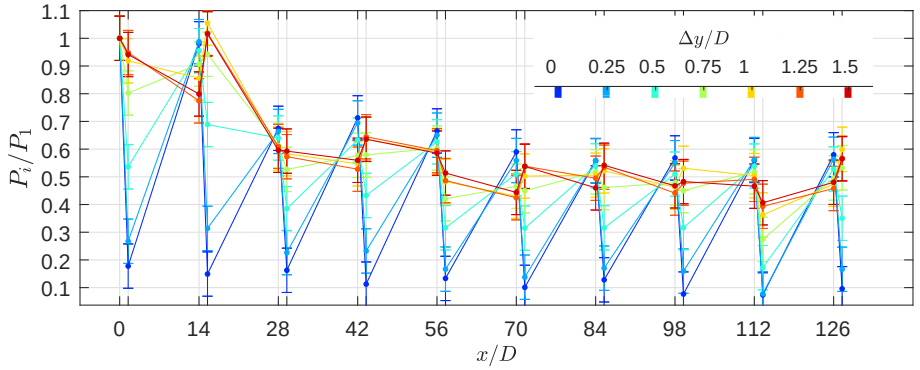

(b)

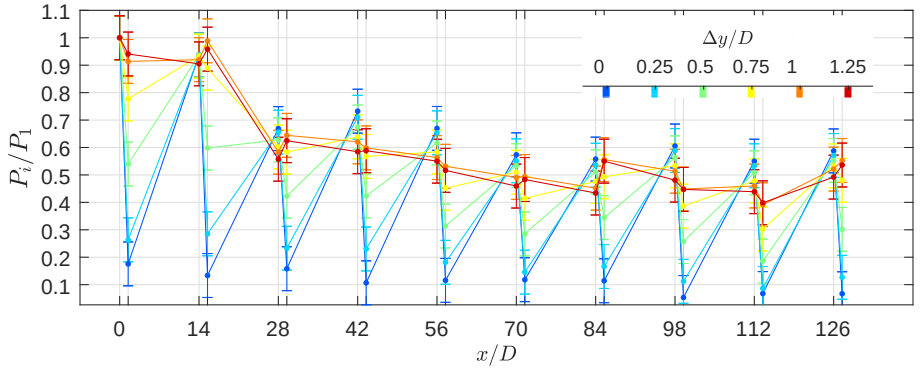

(c)

Figure 4.4: Wind farm measurements of the mean surrogate power in each row for the *NU2-C1* (a), *NU2-C2* (b), and *NU2-C3* (c) layout series. See figure 4.1 for an overview of the layouts.

rows in the aligned configurations measure a very low surrogate power output, of approximately $P_i/P_1 \approx 0.1...0.2$.

The *NU2-C1* layout series shows similar trends as the *NU1-C1* series, however, with a better performance in the staggered configuration. For this layout, every even row measures the same or higher power than the upstream row, indicating less wake losses or a possible local flow interaction, e.g. the local blockage results in a slight acceleration towards the downstream model similar to observations by McTavish et al. (2014). Qualitatively, the mean row power reduces less quickly, with row 10 measuring a surrogate power output of $P_i/P_1 \approx 0.6$.

For the staggered *NU2-C2* layout, the power of the first four rows does not drop significantly, and the power of the fourth row is approximately equal, or even slightly higher, than the value of the first row (it is important to note that considering the measurement uncertainty the small increase is not statistically significant). Similar to the *NU2-C1* series, every fourth row of each recurring four-row-pattern, displays a slightly higher surrogate power. These observations indicate a possible local acceleration of the flow towards each fourth row. The *NU2-C3* series shows similar trends, however, now the values for each fourth row are slightly lower, while the power of each third row has increased. As a result, the mean row power follows a smoother progression towards an asymptote at the end of the farm. With the layout *NU2-C2* and *NU2-C3* it is thus possible to significantly increase the power of the first four rows, to almost the same value of the first row.

The measurements of local turbulence intensity are shown in figure 4.5. When the layouts are aligned, the even rows measure very high values of the local turbulence intensity due to the low velocities in the near wake. However, when the layouts are staggered, a relatively smooth progression is observed, very similar to the other layout series. After approximately 11 rows, the local turbulence intensity plateaus to a value of approximately $TI \approx 13\%$.

4.3 Discussion: wind farm layout

The wind farm results in the previous section displayed a number of main trends. First, most of the improvements in surrogate power output are made at the beginning of the farm. This trend shows good agreements with results in the literature (Barthelmie et al., 2011; Stevens et al., 2014), and indicates the importance of reducing wake losses in the entrance region of the farm. Second, for each series, the layouts with the highest surrogate power show a relatively smooth decrease of the power towards a constant value, or asymptote, at the end of the farm. The independence of surrogate power with row number indicates

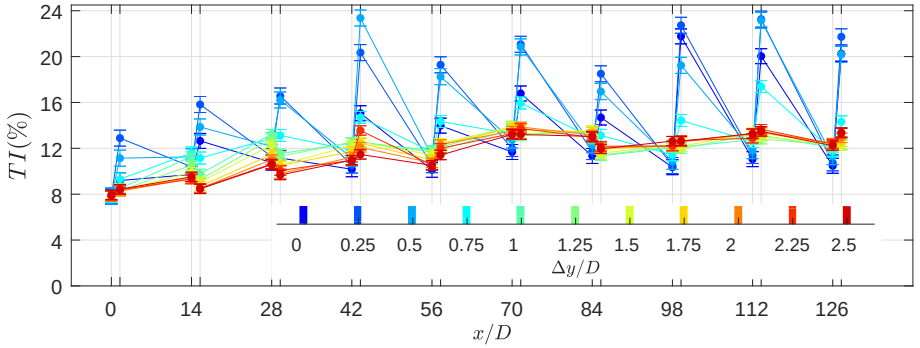

(a)

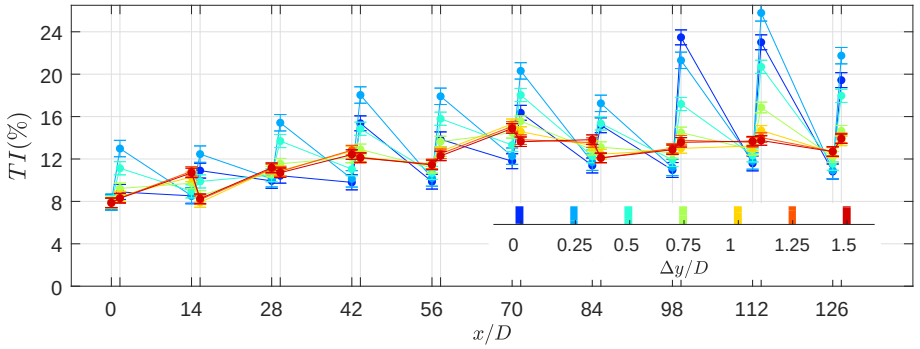

(b)

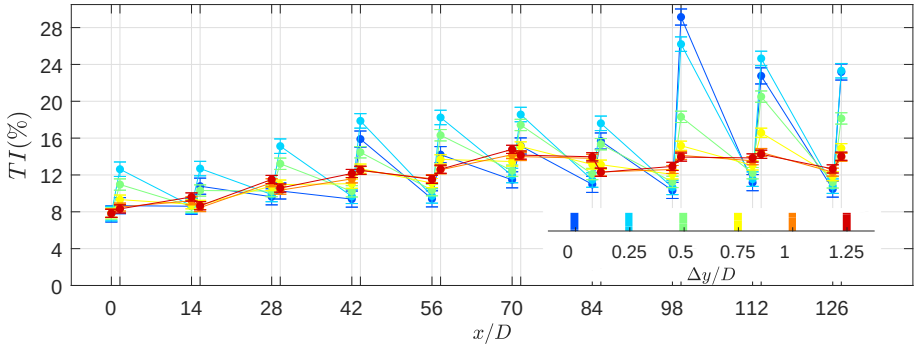

(c)

Figure 4.5: Porous disk measurements of the turbulence intensity in each row for the *NU2-C1* (a), *NU2-C2* (b), and *NU2-C3* (c) layout series. See figure 4.1 for an overview of the layouts.

the approach of a fully developed flow regime. In this section these two regions are analyzed as function of layout by studying the average power of the whole farm, and for the last few rows.

The farm-averaged surrogate power $\overline{P_i}/P_1 = (1/N)\sum_{i=1}^{N} P_i/P_1$ is shown in figure 4.6 (a) as a function of the spanwise shift Δ_y. If the farm efficiency is defined as the total power output per square area, finding the layout with the highest farm efficiency, is similar to finding the layout with the highest farm-averaged surrogate power $\overline{P_i}/P_1$, as the farm area is a constant in the experiments.

In general, the lowest farm efficiencies are measured for a zero spanwise shift. In this case more porous disk models are aligned in the streamwise direction, which increases the wake losses. The wake losses are especially large for the layouts with an uneven streamwise spacing, as half of the models are spaced very closely (e.g. $1.5D$ for *NU2* and $3.5D$ for *NU1*). The *NU2-C1* series has the lowest efficiency for a zero shift, while the variations *NU2-C2* and *NU2-C3* have a slightly higher efficiency.

From the first two layout series with a regular spacing, the double staggered layout (*U-C2* at a spanwise shift of $1.5D$) outperforms the staggered layout (e.g. *U-C1* at a spanwise shift of $2.5D$). The layout series with a moderate uneven streamwise spacing, e.g. *NU1-C1*, does not indicate any advantages, as it performs less well than the original layout series *U-C1*. For the *NU1-C2* series, very little influence of the spanwise shift is seen, so that it also does not provide any obvious advantages. The *NU2-C1* series, at a zero shift, produces the lowest farm efficiency of all layouts. However, the power increases fast for a shift larger than $1D$, and is higher than any of the earlier discussed layouts (e.g. *U-C1*,*U-C2*, *NU1-C1* and *NU1-C2*), at a spanwise shift of $2.5D$. The highest farm efficiencies are measured for the layout series *NU2-C2* and *NU2-C3*. Interestingly, the max power of these layouts is not observed at the maximum spanwise shift of $1.5D$, which would result in more uniform spanwise distribution (the spanwise distribution of porous disk models would be uniform for a spanwise shift of $1.66D$). Instead, the max efficiency is reached at a smaller spanwise shift of $1D$, because of smaller wake losses, and possibly indicating that local flow accelerations due to the close spacing may play a role in this maximum performance. The layout series *NU2-C3* and *NU2-C3* with a spanwise shift of $1D$ also results in low turbulence intensity levels, reaching a value of $13-14\%$ at the end of the wind farm, such that these layouts are found to give the highest power output with a low level of unsteady loading.

As seen in figures 4.3 and 4.4, for a zero spanwise shift, the uneven layouts show an alternating pattern of very low and high surrogate power values, due to the strong wake losses. However, the layouts with the highest power of each series

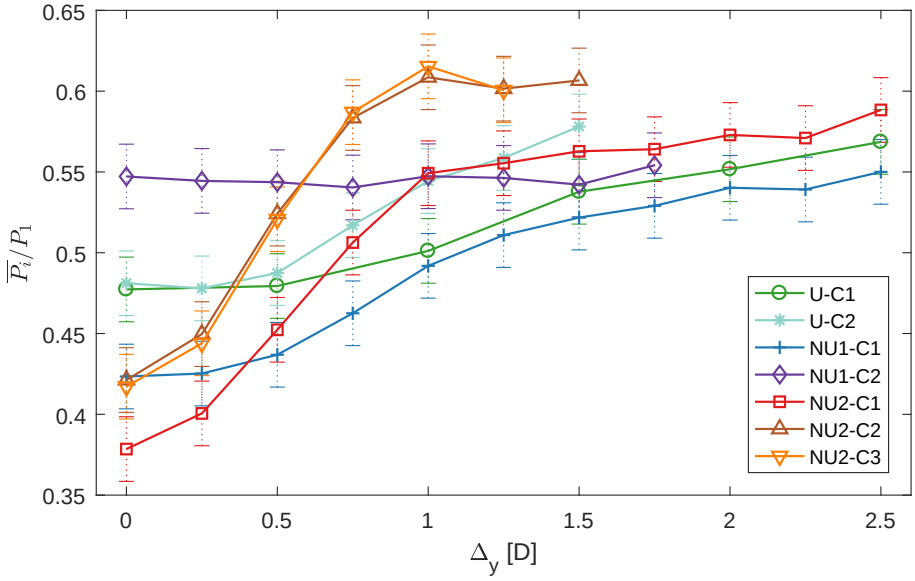

(a)

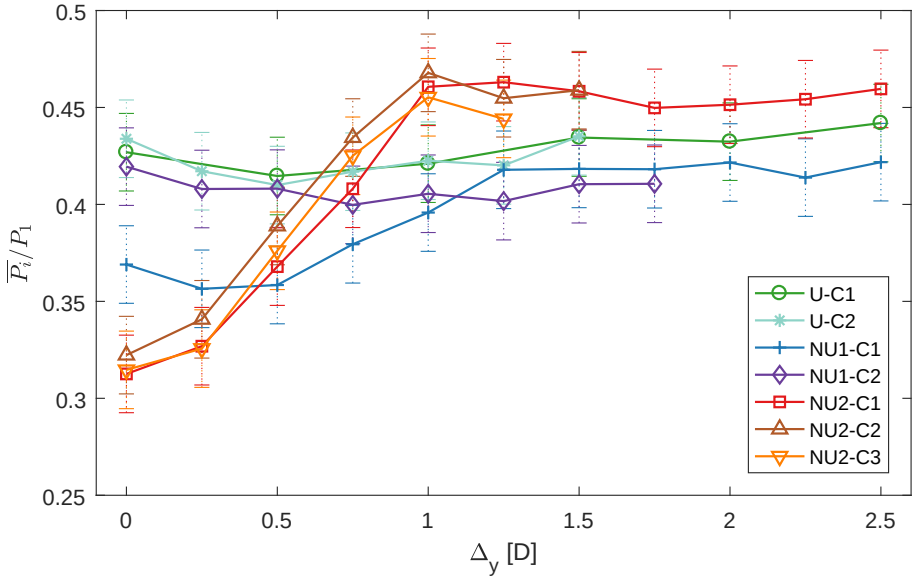

(b)

Figure 4.6: The farm-average surrogate power (a) and the average over row 16-19 (b) as a function of the spanwise shift Δ_y. See figure 4.1 for an overview of the layouts.

show a relatively smooth asymptotic behavior of the surrogate power at the end of the wind farm, indicating that a fully developed regime is being approached. To investigate the influence of layout on the value of the asymptote, figure 4.6 (b) presents the average power of row 16 to 19.

The *U-C1* and *U-C2* show very little differences for the mean power at the end of the farm as a function of layout. This observation shows that all the improvements in power are made in the entrance region of the farm. These observations are in good agreement with the top-down model, which assumes that the wind turbine forces are uniformly applied on the flow, and predicts a power asymptote which is only dependent on the wind turbine density. However, the uneven streamwise layout series *NU1* and *NU2* show a large variation of the power at the end of the farm, with the lowest value when the spanwise shift is zero. Strong wake losses can thus influence the entire farm and reduce the asymptote for non-uniform layouts. It is important to note that the power asymptote can also decrease if the spanwise spacing would be increased (and consequently the streamwise spacing proportionally decreased), as the transverse wake expansion is limited and the area occupied by the wind farm becomes less optimally used (Yang et al., 2012). Such an effect is taken into account in the coupled wake boundary layer (CWBL) model of Stevens et al. (2016a) using an effective coverage area that may be smaller than the actual area for wide spanwise spacings. This effect is not expected to play a role in these experiments as the spanwise spacing is kept constant.

The maximum power for the layouts with a moderate uneven streamwise spacing *NU1*, found for a spanwise shift of $2.5D$, reaches approximately the same value as for the *U-C1* and *U-C2* series. Interestingly, the *NU2* layout series can reach a slightly higher maximum value, with the highest power found for the *NU2-C2* series and a spanwise shift of $1D$. It is important to note that because of the measurement uncertainty, it is difficult to say if this difference is statistically significant. However, these results indicate that the extreme non-uniform streamwise spacing of the *NU2* layout series might have benefits for both the entrance region of the wind farm and the fully developed regime. Yet, it is important to note that if the wind changes direction, a close spacing of wind turbines might result in very high losses, as indicated for a small spanwise shift.

4.4 Conclusions

An experimental parametric study of farm layout was performed with the micro wind farm model in the Corrsin Wind Tunnel. The instantaneous forces of all sixty porous disk models in the central three columns of the wind farm were

Figure 4.7: A photograph of the *NU2-C3* layout with a spanwise shift of $1D$ in the wind tunnel.

measured for 56 different layouts. In this chapter we used the mean surrogate power of each model and the estimated local turbulence intensity to find the most optimal layout. By keeping the area occupied by the wind farm constant for each layout, we are especially interested in finding the configuration with the highest farm efficiency, as defined by the ratio of power over occupied area. Furthermore, the temporal data acquisition capabilities of the porous disk models are used to assess the unsteady loading caused by turbulent scales significantly larger than the disk.

Three main layout series were considered, a series with a uniform streamwise spacing ($S_x/D = 7$), with a moderate alternating streamwise spacing ($S_x/D = 3.5$ and $S_x/D = 10.5$), and with an extreme alternating streamwise spacing ($S_x/D = 1.5$ and $S_x/D = 12.5$). For each series, layout variations are created by sliding specific rows in the spanwise direction.

The experiments resulted in a large data-set of surrogate mean row power and local turbulence intensity for each layout, in controlled and documented conditions. For each series, the layout with the highest overall power, shows a relatively smooth decrease of the row power towards an equilibrium value at the end of the farm. This trend is in agreement with results in the literature

(Stevens et al., 2014, 2016b). The largest improvements in farm efficiency are created by the increase of surrogate power in the first half of the wind farm. All layouts with a uniform streamwise spacing approach approximately the same value at the end of the farm, in agreement with the top-down model (Frandsen, 1992; Calaf et al., 2010), which predicts a single power asymptote for a certain wind turbine density.

However, for the layouts with an alternating streamwise spacing, the mean power at the end of the farm shows a strong dependence on the spanwise shift. The lowest values are generally reached when the spanwise shift is zero, due to strong wake effects. For a moderate uneven streamwise spacing, the maximum power at the end of the farm is reached with a spanwise shift of $2.5D$, and is approximately the same as for a uniform layout. Interestingly, for an extreme uneven streamwise spacing, a slightly higher value is reached at the end of the farm (up to $\approx 5-6\%$) for a spanwise shift of $1D$. The layouts with an extreme uneven spacing were also found to measure the highest farm-aggregate surrogate power, which indicates advantages for both the entrance and the fully developed region. Furthermore, these results indicate the possible beneficial role of local flow accelerations, similar to the results by McTavish et al. (2014) for three wind turbines.

For each series, the layout with highest overall power, also results in the lowest unsteady loading. All of these layouts indicate a similar, slow progression of the unsteady loading, which levels off after approximately $11-13$ rows, and reaches a value of $TI \approx 13-14\%$. For the less optimal layouts, the unsteady loading increases due to wake effects.

Overall it is concluded that the layouts with an extreme alternating streamwise spacing can result in the highest surrogate power and a low unsteady loading if the spanwise shift is larger or equal to $1D$. Specifically the layout *NU2-C2* with a spanwise shift of $1D$ showed the most optimal results. The disadvantage of the layouts with an extreme non-uniform spacing is that for certain wind directions the wake losses can become very large, as indicated in figure 4.6 for a zero spanwise shift. Future studies should explore in more detail the beneficial effects of closely spacing small groups of wind turbines for a range of wind directions.

Chapter 5

Wind farm power output variability

Wind energy is characterized by inherent variability. When wind farms are connected to an electricity grid, the power fluctuations need to be compensated by, e.g., ancillary power generators (Apt, 2007) or wind farm control (Shapiro et al., 2016). It is thus important to understand over which time scales and with what magnitudes the power output fluctuates. This issue has motivated several studies on the spectral characteristics of the electrical power output from a wind farm or a cluster of wind farms (Apt, 2007; Katzenstein et al., 2010; Vigueras-Rodríguez et al., 2010; Stevens and Meneveau, 2014; Bandi, 2017). Understanding the interaction between the wind turbines and the turbulent boundary layer, with its inherent statistical structure and presence of large coherent motions, is necessary for describing the resulting spectrum of the power output.

Apt (2007) analyzed the spectrum of the power, aggregated over six turbines, and observed a power law behavior with a $f^{-5/3}$ scaling over four orders of magnitude in frequencies. This observation raised the question of the relation between the spectrum and the scaling of the velocity fluctuations in the boundary layer, which follow a $f^{-5/3}$ spectrum over a similar range of scales (Larsén et al., 2016). Recently, Bandi (2017) discussed how the spectrum of the power output from a single turbine scales similarly with that of the velocity fluctuations. In this analysis, Bandi (2017) considered the structure function of the power output and showed that higher order structure functions of velocity fluctuations scale similarly, considering inertial range scalings in analogy with Kolmogorov's 1941 theory (Kolmogorov, 1941).

For the sum of the power over many wind farms, the individual wind farm outputs can become uncorrelated on time scales related to local turbulence, because of the large geographical spacing. In this case, self correlation of the power signals becomes dominant, and is shown to lead to a limiting power law scaling of $f^{-7/3}$ (Katzenstein et al., 2010; Bandi, 2017). However, on the scale of a single wind farm, the wind turbine power outputs can show significant correlations (Stevens and Meneveau, 2014), which cannot be neglected in estimating the wind farm spectrum.

For a fixed wind direction, large-eddy simulations by Stevens and Meneveau (2014), confirmed power law behavior with a slope close to $-5/3$ for the spectrum of the aggregate wind farm power output. The spectra also showed a peak at a frequency corresponding to the convective travel time between streamwise aligned turbines. Stevens and Meneveau (2014) confirmed that the wind turbine outputs show indeed a correlation at a time delay similar to the convective travel time between rows.

In this chapter we consider the fundamental question whether power fluctuations in wind farms can be related to the structure of turbulence in boundary layers. First, the measurement data from the micro wind farm experiments are used to study the spectral properties of the porous disk surrogate power outputs, and their relation to spatio–temporal correlations. Based on these observations, we interpret the interaction between the array of wind turbines and the turbulent boundary layer as a discrete spatial sampling in order to model and explain how the wind farm frequency spectrum is composed. The analysis is done by making use of a model-parametrization for the wavenumber–frequency spectrum of the streamwise velocity in high Reynolds number turbulent boundary layers (Wilczek et al., 2015b).

In section 5.1 an overview of the results from the wind tunnel experiment are given including main characteristics of the experimental setup. Based on these observations, a model for the wind farm frequency spectrum is developed in section 5.2. The model is compared with experimental data and conclusions are provided in section 5.3. The content in this chapter is adapted from Bossuyt, J., Meneveau, C., and Meyers, J., "Wind farm power fluctuations and spatial sampling of turbulent boundary layers", Journal of Fluid Mechanics, 823:329-344, 2017 and from Bossuyt, J., Howland, M. F., Meneveau, C., and Meyers, J., "Wind tunnel study of the power output spectrum in a micro wind farm", J. of Physics: Conf. Series, volume 753, 2016.

5.1 Wind farm experiment

In this section, the spatio-temporal acquisition capabilities of the micro wind farm are used to study the spectrum of wind farm power. As described in chapter 2, the instantaneously measured thrust force of a porous disk model can be related to the incoming spatially averaged velocity and a surrogate power output. The porous disk models have a frequency response up to 200 Hz, which, with a geometric scaling of 1 : 3333, covers timescales as small as 16 seconds scaled to full scale. The normalized frequency response is $fD/U \approx 0.6$, which is high enough to study timescales corresponding to turbulent eddies with a size multiple times larger than the porous disk diameter. In this section we use the measurement data from the aligned and staggered layouts (see chapter 3) to study the main trends of the spectrum of the wind farm output.

The power spectral density (PSD) is calculated after normalizing a surrogate power output signal P_i for a porous disk model i with the temporal mean of the signal, denoted with an overbar, e.g. $(P_i(t) - \overline{P_i})/\overline{P_i}$. The PSD is calculated with Matlab's pwelch function, by averaging over 50 segments and windowing with the Hanning function. The calculated PSD's are averaged over all three porous disk models in a certain row. The total surrogate farm power is calculated by summing up all individual power output time signals $P_{WF}(t) = \sum_{i=1}^{60} P_i(t)$. The PSD is then calculated with the same normalization, the pwelch method and the same windowing parameters.

Figure 5.1 shows the estimated PSD's for two cases: an aligned and a staggered wind farm layout. The row-averaged PSD's for single porous disk models are shown with the colored lines, according to the row number. The row-averaged PSD for a porous disk model in the first row, indicated by the blue line, can be considered as a measurement of the surrogate power from the incoming flow characteristics with the application of a spatial filter by the porous disk (see chapter 2). The spatial filtering explains why the slope for the highest frequencies in the measurement range (approximately $50 - 200$ Hz) is steeper than the expected $-5/3$ Kolmogorov slope (as shown in figure 2.5). The PSD for downstream rows show a higher variance due to added turbulence from wakes of upstream models.

The PSD of the total farm power exhibits a significant reduction in variability. Furthermore, the spectrum shows an approximate power law behavior with a slope close to $-5/3$ in a frequency range of approximately $2 - 20$ Hz. This observation is in agreement with previous results from field experiments (Apt, 2007) and LES (Stevens and Meneveau, 2014). Interestingly, this power law behavior for the total farm power extends to lower frequencies than observed for individual models. Considering that the velocity at hub height is approximately

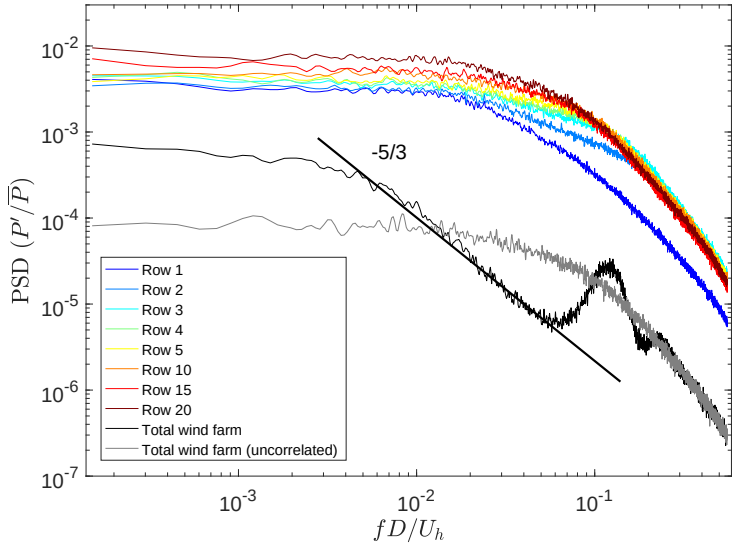

(a)

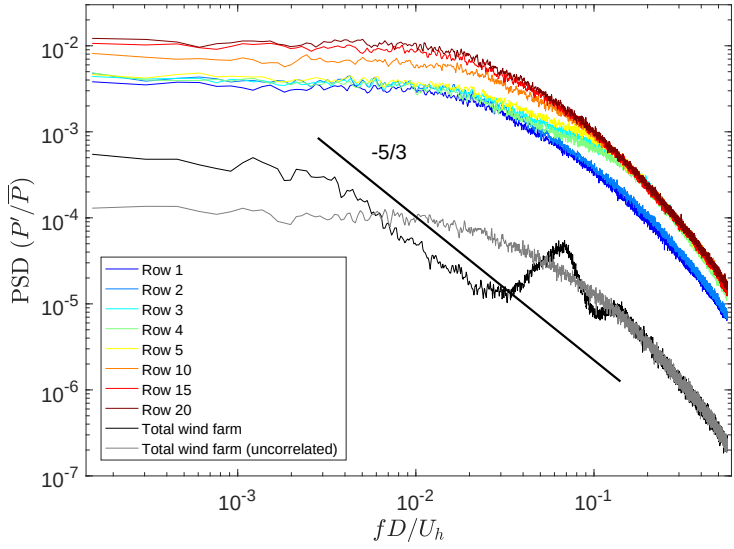

(b)

Figure 5.1: Power spectral density (PSD) measured for an aligned *(a)* and a staggered *(b)* wind farm layout. Colored lines are the average of the individual PSD's for all three porous disk models in a specific row. The black line is the PSD of the total wind farm. The gray line is the PSD of the total wind farm, when the power signals are uncorrelated in time. Frequency is normalized by the velocity measured by the first row and the disk diameter.

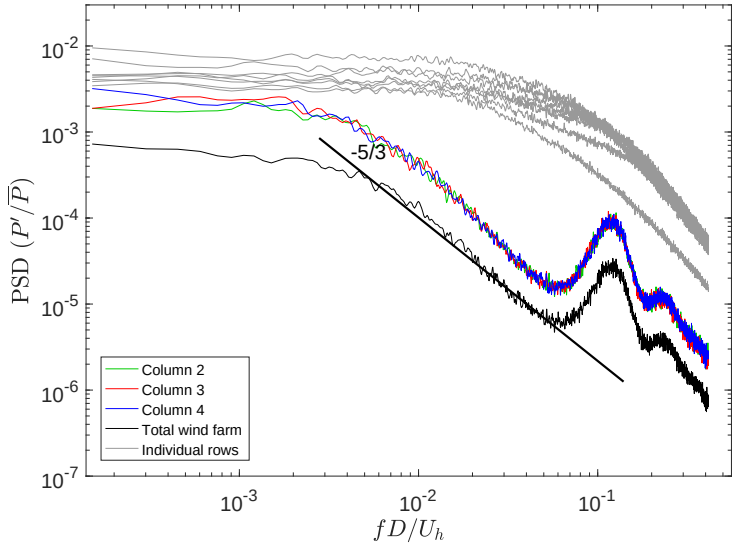

(a)

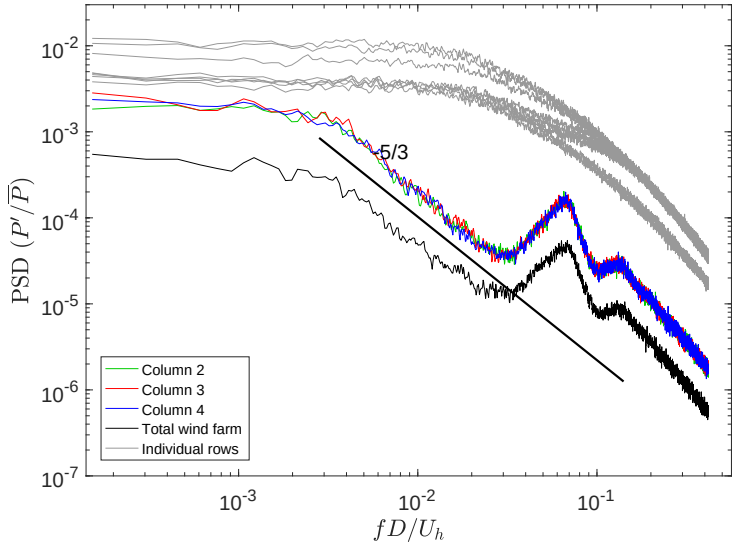

(b)

Figure 5.2: Power spectral density (PSD) measured for an aligned *(a)* and a staggered *(b)* wind farm. Colored lines are the PSD for the total surrogate power of each column. The black line is the PSD of the total farm. The gray lines are the average PSD's for the individual rows, as shown in figure 5.1. Frequency is normalized by the velocity measured by the first row and the disk diameter.

10 m/s in the measurement, the lowest frequency of 2 Hz corresponds to a length scale of 5 m. This length scale is similar to the length of the entire wind farm model. As previously also observed by Stevens and Meneveau (2014) a peak and a second harmonic peak are observed at frequencies corresponding to the convective flow time between two consecutive models. This peak is measured at a frequency of approximately 44 Hz for the aligned and 23 Hz for the staggered farm. Making use of the incoming velocity at hub height measured by the first row of porous disk models, and the streamwise spacing between streamwise consecutive models, the reduced frequency of these peaks is approximately $fL/U = 0.86 - 0.9$ for both cases.

The frequency dependent reduction in variability indicates the importance of cross-correlations in the power signals, which was previously recognized by Sørensen et al. (2002) and Stevens and Meneveau (2014). To verify the specific impact of the correlations, the individual power signals were artificially uncorrelated in time by applying a random time shift. The PSD of the total power output (e.g. the sum of the uncorrelated time signals) is shown by the gray line in figure 5.1. It is seen that the PSD of the total power output for uncorrelated signals (gray line) is approximately $N = 60$ times smaller than the average of the individual porous disk PSD's (colored lines), independent of the frequency. This is in agreement with the reduction of the variance of the mean of N normally distributed, uncorrelated, signals.

The higher variance for the PSD of the correlated wind farm power output (black line on figure 5.1) at frequencies lower than 5 Hz, compared to the uncorrelated wind farm (gray line), indicates that the power output of porous disk models are correlated at these time scales. For higher frequencies ($5 - 20$ Hz) we find that the porous disk models are anti-correlated, resulting in a lower variance. Finally, at the time scale corresponding to the convective flow time between two consecutive models, also shown by the peak, we notice a correlation between porous disk models.

Results for the staggered layout show similar trends, as seen in figure 5.1 *(b)*. The peak has now shifted to a lower frequency due to the larger streamwise spacing. The power law region with a slope close to $-5/3$ now reaches to frequencies as low as 1 Hz. Considering a hub-height velocity of 10 m/s, this corresponds to length scales of 10 m, similar to the length of the wind tunnel test section.

The surrogate power outputs of streamwise aligned models are significantly correlated, while the correlation in the spanwise direction is almost negligible (see section 3.3). The influence of this directional dependence of the cross-correlation between porous disk models on the power output variability is illustrated by figure 5.2. Colored lines represent the PSD of the total power output of each

column (as defined in figure 2.3) of streamwise aligned porous disk models. The black line represents the PSD for the total wind farm and the gray lines represent the individual row-averaged porous disk PSD's, as shown in figure 5.1. Summation over all porous disk models in a column results in a reduction of the variability with the same trends as described before. Summation over all columns, to find the total farm power, reduces the variance with a constant factor of approximately 3. It is thus clearly the significant streamwise correlation which plays a key factor in the specific variability reduction.

5.2 Modeling of the wind farm power output frequency spectrum

Based on the observations in the previous section, this section describes a model to estimate and explain the shape of the spectrum of the wind farm power output. In the first part of this section, the relation between the wind turbine power and velocity fluctuations is discussed. This will allow the use of a recently developed parametrization for the wavenumber–frequency spectrum of the velocity (Wilczek et al., 2015b), as discussed in the second part. Then, a transfer function to represent the discrete spatial sampling of the boundary layer is derived. Both are then combined to find the frequency spectrum of the wind farm power output. This section is concluded with a validation of the model with the experimental data from the previous section.

5.2.1 Power fluctuations

The power output of a wind turbine $P_i(t)$ is generated by the forces acting on the blades as they sweep through the flow field. At a typical tip speed ratio the order of $5-10$, the blade tips sweep through the flow $5-10$ times faster than the incoming velocity. The focus of this study is on turbulent length scales that are significantly larger than the turbine diameter, i.e comparable to the streamwise turbine spacing or larger. Over the corresponding timescales, the blades make multiple full rotations within the time for turbulent eddies of these scales to pass through the wind turbine. The turbine power can therefore be expressed in terms of the disk average power of the air flowing through the rotor area (the spatial average is denoted with angle brackets) $P_{air}(t) = (1/2)\rho A\langle u\rangle^3(t)$ and the instantaneous power coefficient of the wind turbine $C_P(t)$ (Milan et al., 2013), thereby neglecting higher order terms and leading to $P_i(t) \approx (1/2)\rho A C_P(t)\langle u\rangle_i{}^3(t)$ for wind turbine i.

Focusing on the below-rated operating regime, wind turbines are controlled to maximize aerodynamic efficiency. In this regime, the overall turbine power coefficient $C_P(t)$ is kept maximal and can be considered nearly constant (Aho et al., 2012). Furthermore, power fluctuations are significantly less sensitive to changes in $C_P(t)$ then to velocity fluctuations (Theunissen et al., 2015). With a constant power coefficient, the instantaneous turbine power depends on the cube of the velocity, as given by $P_i(t) \approx C_1 {\langle u \rangle_i}^3(t)$ and with $C_1 = \frac{1}{2}\rho A C_P$ a constant.

The spatially averaged velocity is decomposed in a temporal mean and fluctuating part: $\langle u \rangle = \overline{\langle u \rangle} + \langle u \rangle'$, to express the power fluctuations in terms of the velocity fluctuations:

$$P_i'(t) \approx C_1 \left(\overline{\langle u \rangle_i} + \langle u \rangle_i' \right)^3 - C_1 \overline{\left(\overline{\langle u \rangle_i} + \langle u \rangle_i' \right)^3} \tag{5.1}$$

$$\approx 3 C_1 \overline{\langle u \rangle_i}^3 \left(\frac{\langle u \rangle_i'(t)}{\overline{\langle u \rangle}_i} + \frac{{\langle u \rangle_i'}^2(t)}{\overline{\langle u \rangle_i}^2} + \frac{1}{3} \frac{{\langle u \rangle_i'}^3(t)}{\overline{\langle u \rangle_i}^3} - \frac{\overline{{\langle u \rangle_i'}^2}}{\overline{\langle u \rangle_i}^2} - \frac{1}{3} \frac{\overline{{\langle u \rangle_i'}^3}}{\overline{\langle u \rangle_i}^3} \right) \tag{5.2}$$

$$P_i'(t) \approx C_2 \langle u \rangle_i'(t), \tag{5.3}$$

with $C_2 = \frac{3}{2}\rho A C_P \overline{\langle u \rangle}^2$. Equation 5.3 involves neglecting higher order terms. For typical atmospheric conditions over reasonably short time intervals over which nearly stationary conditions can be assumed (e.g. $10 - 20$ minutes, say), it is acceptable to assume $\langle u \rangle' / \overline{\langle u \rangle} \ll 1$ (e.g. measurements at the Horns Rev wind farm show $TI_u = (\overline{u'^2})^{1/2}/\overline{u} \approx 0.05 - 0.1$ (Hansen et al., 2012)), so that the higher order terms can be neglected as a first approximation.

With these simplifications, the power fluctuations are shown to scale approximately linearly with the disk-averaged velocity fluctuations. As shown by Bandi (2017), higher powers of u' scale similarly, providing further justification for the simplifications used. The spectrum of the aggregated wind farm power ($P_{\mathrm{WF}} = \sum P_i$) can thus be considered as a discrete spatial sampling of the fluctuating disk-averaged velocity field.

5.2.2 Spatio-temporal flow description

To evaluate the frequency spectrum of the power output of an array of turbines with a given spatial distribution, a description for the space–time correlation of the boundary layer is required. To this end, we use the model developed by Wilczek et al. (2015b) for the spectral analogue, the wavenumber–frequency

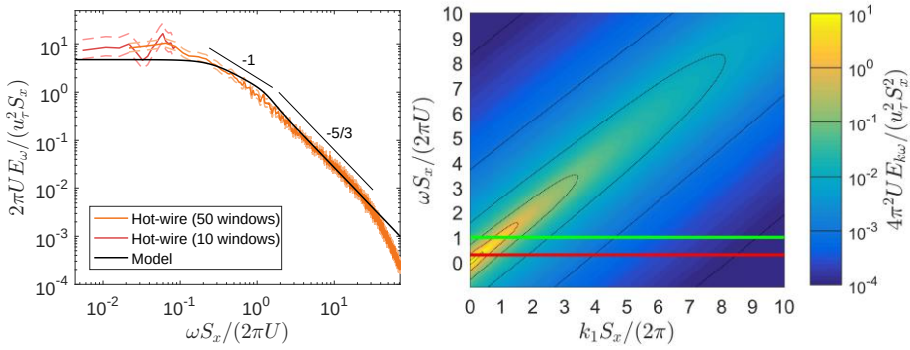

(a) (b)

Figure 5.3: (*a*) Comparison of the modeled frequency spectrum E_ω with the measured hot-wire spectrum upstream of the scaled wind farm and (*b*) the corresponding modeled streamwise wavenumber–frequency spectrum $4\pi^2 U E_{k\omega}(k_1, \omega)/(u_\tau^2 S_x^2)$. The horizontal green and red line indicate the location of two cuts of the spectrum, discussed in §5.2.4 and shown in figure 5.5.

spectral density, as given by:

$$\Phi_{11}(k_1, k_2, \omega) = \frac{E_{kk}(k_1, k_2)}{\sqrt{2\pi\langle(\mathbf{v}\cdot\mathbf{k})^2\rangle}} \exp\left(-\frac{(\omega - k_1 U)^2}{2\langle(\mathbf{v}\cdot\mathbf{k})^2\rangle}\right). \tag{5.4}$$

Here, U is the convective velocity, taken to be a mean velocity at hub-height in the x direction, $\omega = 2\pi f$ the angular velocity, $E_{kk}(k_1, k_2)$ the wavenumber spectrum of the streamwise velocity fluctuations (see appendix A for definitions of the spectra), and $\mathbf{v}$ a random sweeping velocity in the horizontal direction.

The approach is developed in a horizontal plane at hub height z and spanning the streamwise k_1 and spanwise k_2 directions, where we assume horizontal homogeneous flow properties. The spatial averaging of the velocity over the rotor area in the vertical direction is not considered, but takes place at smaller length and corresponding time scales (the order of the diameter) than those of interest (the order of the streamwise spacing and larger). Thereby, the height-dependence of the spatio-temporal flow structure (Wilczek et al., 2015a) over the rotor height is not considered, and is expected to slightly smear out the spectrum over the frequency axis.

We use the analytical form for the spatial 2D spectrum $E_{kk}(k_1, k_2)$ and the necessary parameters as provided by Wilczek et al. (2015b). This analytical spectrum assumes a classical scaling for the logarithmic and inertial range regions of streamwise wavenumbers in turbulent boundary layers (e.g. k_1^{-1} and

$k_1^{-5/3}$), see Nickels et al. (2005). The high wavenumber range of this spectrum, $E_{kk}^{>}(k_1, k_2)$, is modeled by an infinitely extended inertial range:

$$E_{kk}^{>}(k_1, k_2) = \frac{\Gamma(1/3)C_K}{5\sqrt{\pi}\Gamma(5/6)}\epsilon^{2/3}\left(1 - \frac{8}{11}\frac{k_1^2}{k^2}\right)k^{-8/3}, \tag{5.5}$$

with $k = \sqrt{k_1^2 + k_2^2}$, $C_K \approx 1.6$ the Kolmogorov constant, $\epsilon = u_\tau^3/(\kappa z)$ an estimate for the energy dissipation and $\kappa \approx 0.4$ the von Kármán constant, such that $(\Gamma(1/3)C_K)/(5\sqrt{\pi}\Gamma(5/6)) \approx 0.268$. For the low wavenumbers, a k_1^{-1} region is transitioned to a constant spectrum by:

$$E_{kk}^{<}(k_1, k_2) = z u_\tau^2 D(z)\left(\left(\frac{1}{H}\right)^\beta + k_1^\beta\right)^{-1/\beta}, \tag{5.6}$$

with the exponent $\beta = 4$ and H a length scale for the boundary layer height. These two ranges are blended together to form the complete wavenumber spectrum:

$$E_{kk}(k_1, k_2) = [1 - \theta(kz)]E_{kk}^{<}(k_1, k_2) + \theta(kz)E_{kk}^{>}(k_1, k_2), \tag{5.7}$$

with $\theta(kz) = (\tanh(\alpha \log(kz)) + 1)/2$ and $\alpha = 4$. The height dependent amplitude $D(z)$ for the low wavenumber range is determined numerically such that $\int E_{kk}\, dk_1\, dk_2 = \sigma_u^2$. The wavenumber spectrum is thereby defined by three parameters: H, u_τ and σ_u. In projecting E_{kk} to the wavenumber–frequency domain with equation 5.4, the term $\langle(\mathbf{v}\cdot\mathbf{k})^2\rangle$ is modeled as $\langle(\mathbf{v}\cdot\mathbf{k})^2\rangle = \sigma_u^2\left(k_1^2 + Ck_2^2\right)$, with $C \approx 0.41$ (Wilczek et al., 2015b).

In figure 5.3 (*a*) we compare the spectrum measured by the hot-wire probe in the wind tunnel experiment upstream from the wind farm, with the 1D spectrum implied by this model ($E_\omega = \iint \Phi_{11}(k_1, k_2, \omega)\, dk_1\, dk_2$) and based on the values for $H = \delta_{99}$, u_τ and σ_u from the hot-wire measurement (see section 2.1). The hot-wire spectrum is estimated by averaging over windowed segments. Because the time-length of the hot-wire signal is limited, the spectrum is estimated once by averaging over 10 segments to cover the lowest frequencies, and once over 50 shorter windows for a better estimate of the higher frequency range. A Hanning window is used and the 95% confidence bounds are shown, as estimated by the *pwelch* routine in Matlab™. Overall, the agreement is acceptable and mostly within the uncertainty bounds for high frequencies. Note that the dissipation range is not modeled as it takes place at scales significantly smaller than those of interest. The modeled spectrum has a slightly lower energy at the lowest frequencies. This is caused by the higher modeled spectrum where the -1 and $-5/3$ regions are blended, which results in a smaller parameter $D(z)$ and a lower spectrum or correlation in the low frequency and wavenumber ranges. This limitation of the modeled spectrum should be kept in mind when

modeled wind farm spectra are compared with experimental data, as further discussed in section 5.2.5. The streamwise wavenumber–frequency spectrum $E_{k\omega}(k_1,\omega) = \int \Phi_{11}(k_1,k_2,\omega)\,dk_2$ from the model using the measured hot-wire parameters, is shown in figure 5.3 (b).

Inside the wind farm, the wind turbines interact with the boundary layer by producing wakes with a lower velocity and added turbulence, thereby modulating the spatio-temporal structure in some degree. These effects result in a deviation from the classical scaling for the velocity spectra in a turbulent boundary layer. However, it is experimentally extremely challenging to measure the full wavenumber–frequency spectrum of such a large domain. Furthermore, from the cross-correlation results in section 3.3 it is clear that inside the farm the large scale spatio-temporal structure of the flow is still very similar to that of a classical turbulent boundary layer, but with an increased decorrelation due to the turbine wakes. We thus use the wavenumber–frequency spectrum for the boundary layer in front of the wind farm to characterize the baseline flow properties that are sampled by the array of turbines.

5.2.3 Spatial sampling transfer function

The fluctuating part of the wind farm power is evaluated as the sum of the fluctuations of each turbine, according to: $P'_{\mathrm{WF}} = \sum P'_i \approx C_2 \sum \langle u \rangle'_i$ (see (5.3)), where we assume that C_2 is the same for all turbines. Consequently, the sampling of the velocity field by the wind farm can be expressed as a convolution evaluated at the wind farm position, e.g. $P'_{\mathrm{WF}}(t) \approx C_2 \iint g(x,y) u'(x,y,t)\,dx\,dy$, where $g(x,y)$ is the wind farm sampling kernel. This function represents the sum over all turbines as well as the spatial averaging over the rotor area of each wind turbine. The latter is here modeled with a Dirac impulse at the location of turbine i and a box filter with width equal to the turbine diameter. The wind farm sampling function is given by:

$$g(x,y) = \sum_{i=1}^{N} \delta(x - x_i) \frac{1}{D} H\left(\frac{D}{2} - |y - y_i|\right). \tag{5.8}$$

Analogous to the power spectrum of the wind farm power output, we consider the spatial filtering of the energy spectrum of the streamwise velocity $\Phi_{11}(k_1,k_2,\omega)$, by the respective transfer function $\widehat{g}(k_1,k_2)$ (Maidanik and Jorgensen, 1967):

$$\widetilde{\Phi}_{11}(k_1,k_2,\omega) = |\widehat{g}(k_1,k_2)|^2 \Phi_{11}(k_1,k_2,\omega), \tag{5.9}$$

where the tilde indicates the spatial sampling. The frequency spectrum can then be found by integrating over all wavenumbers:

$$\widetilde{E}_\omega(\omega) = \int_{-\infty}^{\infty}\int_{-\infty}^{\infty} \widetilde{\Phi}_{11}(k_1, k_2, \omega)\, dk_1\, dk_2, \tag{5.10}$$

so that the filtered energy spectrum is connected to the spectrum of the wind farm power output by $PSD(P'_{\text{WF}}) \approx C_2^2 \widetilde{E}_\omega$. The transfer function $\widehat{g}(k_1, k_2)$ is found by taking 2π times the Fourier transform of the physical-space filter function in each direction (see appendix B for details):

$$\begin{aligned}\hat{g}(k_1, k_2) &= \int_{-\infty}^{\infty}\int_{-\infty}^{\infty} g(x, y)\exp(-ik_1 x)\exp(-ik_2 y)dxdy \\ &= \frac{\sin\left(k_2\frac{D}{2}\right)}{k_2\frac{D}{2}} \sum_{i=1}^{N} \exp\left(-i(k_1 x_i + k_2 y_i)\right),\end{aligned} \tag{5.11}$$

resulting in:

$$|\widehat{g}(k_1, k_2)|^2 = \left(\frac{\sin\left(k_2\frac{D}{2}\right)}{k_2\frac{D}{2}}\right)^2 \left(\sum_{i=1}^{N}\sum_{j=1}^{N} \cos\left(k_1\left(x_i - x_j\right) + k_2\left(y_i - y_j\right)\right)\right). \tag{5.12}$$

5.2.4 Discussion

The manipulation of the wind farm frequency spectrum by the sparse sampling of the turbulent boundary layer can be better understood by considering the simplified transfer function for a single streamwise column of wind turbines. For such an array of N wind turbines with uniform streamwise spacing S_x, the transfer function is (see appendix B for details):

$$|\widehat{g}(k_1, k_2)|^2 = \underbrace{\left(\frac{\sin\left(\frac{k_1 S_x N}{2}\right)}{\sin\left(\frac{k_1 S_x}{2}\right)}\right)^2}_{\widehat{g_A}(k_1)} \underbrace{\left(\frac{\sin\left(k_2\frac{D}{2}\right)}{k_2\frac{D}{2}}\right)^2}_{\widehat{g_B}(k_2)}. \tag{5.13}$$

The transfer function is separable in the streamwise and spanwise directions, with both components shown in figure 5.4. The streamwise contribution $\widehat{g}_A(k_1)$ shows a power law decrease of the amplitudes for reduced wavenumbers of $kS_x/(2\pi) < 1$ and peaks with amplitude N^2 at increments $kS_x/(2\pi) = 0, 1, 2, ...$ of the streamwise spacing. The spanwise contribution $\widehat{g}_B(k_2)$, shown in red, represents the averaging over the rotor width. Because this only influences scales

significantly smaller than S_x, with a comparably smaller energy, the effect of $\widehat{g}_B(k_2)$ is not considered in the next part of this discussion. Doing so, the filtering is a function of k_1 only, and is given by $\widetilde{E}_\omega(\omega) = \int \widehat{g}_A(k_1) E_{k\omega}(k_1, \omega)\, dk_1$.

If the flow would stay perfectly correlated, while being advected by the mean horizontal velocity U, the wavenumber–frequency spectrum would be given by $E_{k\omega} = E_k(k_1)\delta(k_1 - \omega/U_1)$, representing a Doppler shift. In this case, the filtered frequency spectrum is given by $\widetilde{E}_\omega(\omega) = \widehat{g}_A(\omega/U_1)E_k(\omega/U_1)$. The transfer function then directly modulates the resulting frequency spectrum, thereby extending and/or steepening the already present power law region of the velocity spectrum and introducing peaks at frequencies corresponding to the travel time between rows of turbines. Interestingly, as shown in figure 5.4, the power law range of the transfer function has a slope close to $-5/3$ for an aggregate over twenty rows. In the limit of large N and $k_1 S_x/(2\pi) \ll 1$, the slope can be shown to reach a -2 asymptote.

In practice there is temporal decorrelation of the turbulence, which is here modeled in the wavenumber–frequency model by considering random sweeping (Wilczek et al., 2015b). The impact on $E_{k\omega}(k_1, \omega)$ is depicted in figure 5.3 (b) and figure 5.5 by the Doppler broadening (i.e. a broader distribution of the spectral energy) along the Doppler shift (as described by $\delta(k_1 - \omega/U_1)$). Consequently, the spectral energy content of a single frequency has contributions from a range of wavenumbers. The influence on the spatially sampled frequency spectrum is visualized in figure 5.5. Two cuts of $E_{k\omega}(k_1, \omega)$ are shown, together with the streamwise transfer function for a wind farm with twenty rows. Due to the Doppler broadening, the sharp features from the transfer function smear out. More specifically, it widens and reduces the amplitude of the peak, and smooths out the power law region of the transfer function.

5.2.5 Validation with experimental data

The frequency spectrum of the wind farm power output is calculated by numerically integrating equation 5.10, making use of the spectrum from section 5.2.2, and with $|\widehat{g}(k_1, k_2)|^2/N^2$ as the transfer function (see appendix B for an overview of the transfer functions). Dividing by N^2 is done to represent the relative reduction of the spectra (cf. the normalization in section 5.1). Because figures 5.6 and 5.7 compare the spectra of velocity fluctuations, the surrogate power signals from the wind tunnel study are scaled with the constant $C_2 = (3/2)\rho A C_P \overline{\langle u \rangle}^2$ to represent the same units. The signals are furthermore also divided by the number of considered porous disk models N to represent the relative reduction in the fluctuations. Here, $\overline{\langle u \rangle}$ is chosen as the average velocity measured by the considered porous disk models in the experiment and also used

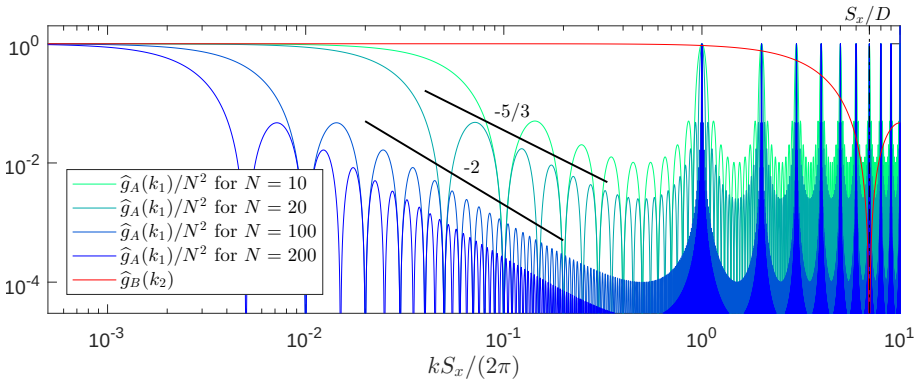

Figure 5.4: Spatial sampling transfer functions for a single streamwise column of N wind turbines, spaced evenly with spacing S_x and with diameter D. The lines for $\hat{g}_A(k_1)$ show lobes beginning at decreasing wavenumber as N increases from 10 to 200. The line for $\hat{g}_B(k_2)$ (red) does not display low-wavenumber lobes below $k_2 S_x/(2\pi) \sim S_x/D$.

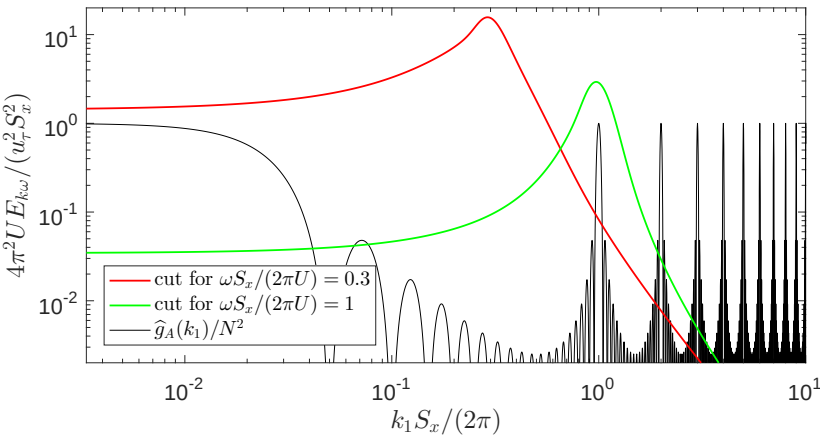

Figure 5.5: Comparison of two cuts of the wavenumber–frequency spectrum $E_{k\omega}(k_1, \omega)$ from figure 5.3 with the streamwise transfer function $\widehat{g}_A(k_1)$ for a streamwise column of twenty wind turbines, spaced evenly with a spacing S_x.

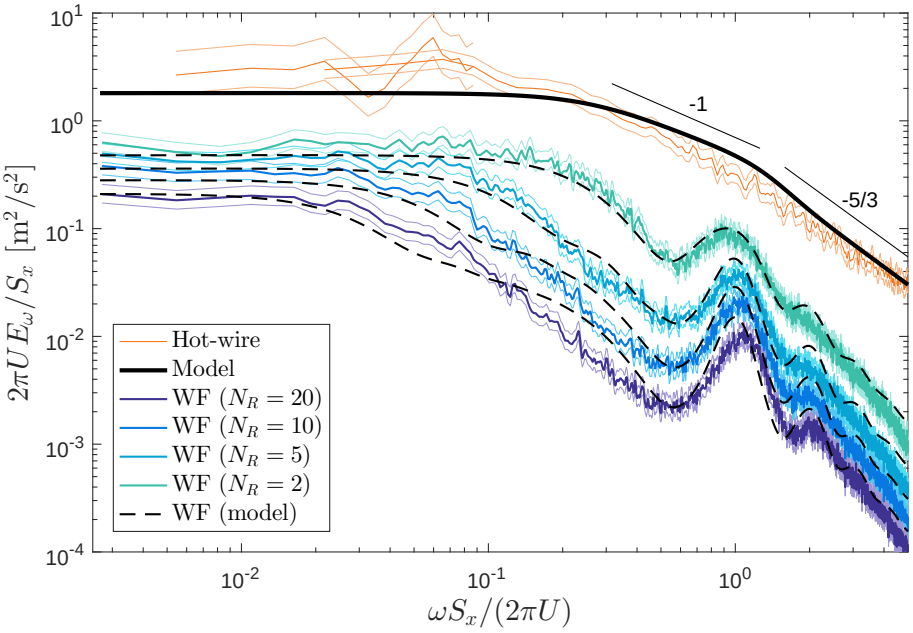

Figure 5.6: Comparison of the modeled wind farm spectrum and the wind tunnel data, for which 95% confidence bounds are displayed as estimated by the *pwelch* routine in Matlab™. Results are shown for an aligned layout.

to normalize the frequency axis, as an approximation of the convection velocity in the experiment.

A comparison between the modeled wind farm spectra (dashed lines) and experimental data (solid lines) is given in figures 5.6 and 5.7. As a reference, the hot-wire spectrum (orange) and the corresponding unfiltered model spectrum (black) are also shown. On each figure, four different wind farm spectra are included, each for a different sum of wind turbine power outputs, as indicated by the number of rows N_R over which the aggregate is taken. In each row, the values from the three central models are measured, resulting in a total aggregate over $N = 3N_R$ porous disk models. When wind tunnel results are shown for less than twenty rows, the rows are selected counting from the end of the wind farm.

For the aligned case (figure 5.6), excellent agreement is observed for $N_R = 2$, approximately within the measurement uncertainty bounds. When more rows are considered in the aggregate, the model correctly predicts the extension of the power law region to lower frequencies. However, the agreement weakens

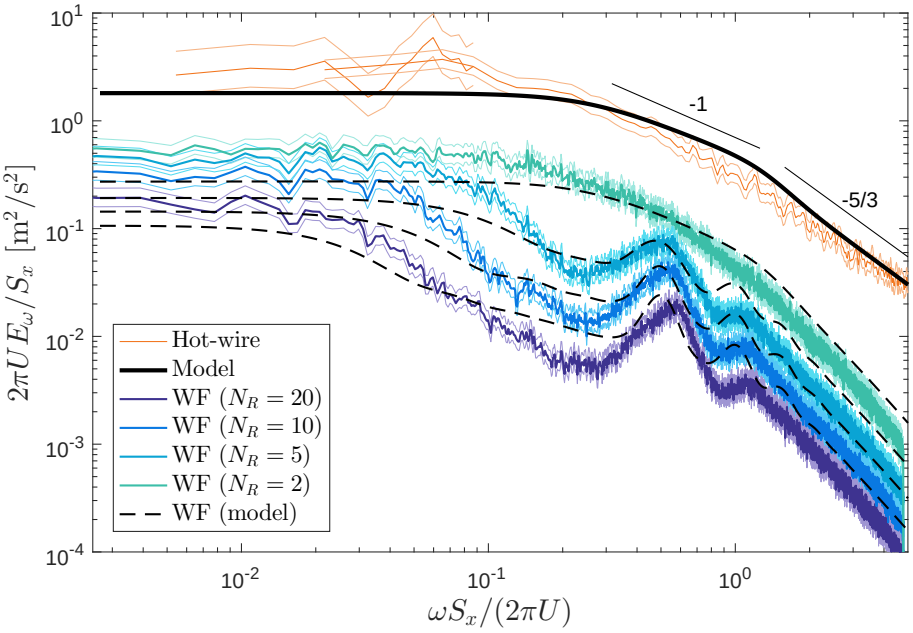

Figure 5.7: Comparison of the modeled wind farm spectrum and the wind tunnel data, for which 95% confidence bounds are displayed as estimated by the *pwelch* routine in Matlab™. Results are shown for a staggered layout.

and the modeled slope shows deviations from the measured spectra. More specifically a bulge appears in the power law range, which influences the local slope, and the peaks become over predicted up to 1.5 times for the largest aggregate. On the other hand, the low frequency limit of the model spectrum agrees with the experimental data within the uncertainty bounds. In general, it can be seen that the two main effects observed in the literature are captured by the model: an extended power-law region to lower frequencies than observed for the unfiltered spectrum and peaks at frequencies comparable to the turbine-to-turbine convection time.

For the staggered layout (figure 5.7), it is observed that the model correctly predicts the peaks at a lower frequency due to the larger apparent spacing between streamwise aligned turbines, and that the magnitude of the main peaks are within the uncertainty bounds. The agreement is however also not perfect. There is an underestimation of the spectrum at low frequencies up to a factor of 2, and the second peaks at $\omega S_x/(2\pi U) = 1$ are overestimated.

The differences for the aligned and staggered layout are expected to be mainly

caused by the use of an approximate wavenumber–frequency model with a lower energy in the low wavenumber and frequency ranges, and which does not consider the lower velocity and increased decorrelation by the presence of the wind turbine wakes. The largest differences are seen for the staggered layout. Because the apparent spanwise spacing is twice as small, the resulting wind farm spectrum becomes significantly more sensitive to the spanwise correlation, or in some cases anti-correlation, as observed in section 3.3. This indicates that the approach can be improved by better representing the wavenumber–frequency spectrum inside the wind farm.

5.3 Conclusions

An analytical model for the frequency spectrum of the aggregate power output from a wind farm is presented, as function of wind farm layout and inflow turbulence properties of the wind. The calculation is performed in spectral space, based on an analytical model for the wavenumber–frequency spectrum. This approach allows us to interpret and explain the interaction between the wind turbines and the boundary layer flow as a discrete spatial sampling. More specifically, it is shown how Doppler shift and broadening smear out the sharp features of the spatial sampling transfer function. The model also reproduces the observed peak in the spectrum of a wind farm at a frequency corresponding to the convective travel time between rows, and the extended steeper decay in the spectrum. The steeper decay can be considered close to a $-5/3$ power law region (but is not strictly such a power law), which reaches up to lower frequencies than present in the spectrum of the velocity.

Considering its simplifications and assumptions, the model shows good agreement with the measurement data for an aligned wind farm. For a staggered layout the model under predicts the spectrum for frequencies $fS_x/U < 0.2$. This is expected to be related to the imperfect modeling of the flow inside the wind farm, more specifically an underestimation of the spanwise correlation. Further improvement, by studying how the wavenumber–frequency spectrum is altered by the presence of the wind turbines, is the subject of future research.

Chapter 6

Conclusions and future research

The main conclusions of this dissertation are formulated in section 6.1 and followed by a discussion of future research possibilities enabled and motivated by this work, in section 6.2.

6.1 Conclusions

Experimental data of large wind farms are necessary for validation of analytical and numerical models. While validation with field experiments is challenging due to atmospheric variability and limited available data, wind tunnel studies can provide detailed measurements in controlled conditions. However, wind tunnel studies have been limited to small wind farms (e.g. 30 turbines or less), only a few layouts (e.g. aligned or staggered), and typically without measurements of the power outputs. Also studies of layout by high-fidelity numerical simulations, such as LES, are limited, and typically consider only uniform spacings. In the current dissertation, porous disk models enabled wind tunnel measurements of a scaled farm with 100 turbines for many different, uniform and non-uniform layouts.

The porous disk approach makes it possible to match the far-wake flow properties of a wind turbine operating in below-rated regime, by wielding a thrust coefficient which is only weakly Reynolds number dependent. Considering these approximations, the focus of this work is specifically on the interaction of

the larger and energy containing turbulent scales in the flow with a wind farm. We have shown that, through instrumenting the tower with strain gages, it is possible to measure the thrust force accurately with a frequency response that reaches up to the natural frequency of the model, and is high enough to measure the spatial filtering of the velocity field by the disk. This alternative to measuring the electrical power from a generator in a small scale rotor model circumvents the difficulties created by low aerodynamic and mechanical efficiencies typical for such setups. Furthermore, the strain signals can be used to estimate the time signal of the spatially averaged incoming velocity and a surrogate for the power output, by making use of the known thrust coefficient and momentum theory. Each model was individually calibrated with an automatic calibration apparatus. A wind farm with 100 porous disk models was installed in the Corrsin Wind Tunnel, in a configuration which allows easy changes of layout through sliding rows in the spanwise direction, or changing the streamwise spacings. By naturally developing the boundary layer over an appropriate surface, after tripping it at the entrance of the test-section, realistic boundary layer conditions were created, with a correct scaling of the mean velocity, turbulence intensity and integral length scale.

The performance of the micro wind farm model was validated with measurements of a classical aligned and staggered layout, and four intermediate configurations. The measurements of surrogate power showed a reasonably good agreement with results for the Horns Rev wind farm (Barthelmie et al., 2007) and trends observed in the LES study of Stevens et al. (2014). The frequency response of the measurements was used to measure the correlations of surrogate power outputs. The wind farm results showed a significant correlation for streamwise aligned models, with a time delay related to the convective travel time between consecutive rows. For a staggered layout, a smaller anti-correlation was measured between two consecutively staggered models. These observations are in good agreement with the structure of high-Reynolds number turbulent boundary layers (Ganapathisubramani et al., 2005; Hutchins and Marusic, 2007). The correlation results also showed and excellent agreement with data from an LES of a finite wind farm by Stevens and Meneveau (2014). Furthermore, the streamwise velocity in a vertical plane through the center of the wind farm was measured with a hot-wire anemometer for an aligned and staggered layout. The porous disk measurements of spatially averaged velocities show a good agreement with the hot-wire measurements, while the estimated turbulence intensities are lower due to spatial filtering. Although a porous disk does not perfectly match the detailed near-wake features of a wind turbine, the overall wake characteristics, the recovery rate and boundary layer interaction, which is indicated by a strong shear layer at the top-height of the models, were found to be in good qualitative agreement with experimental measurements in the literature (Chamorro and Porté-Agel, 2011; Chamorro et al., 2011).

Based on the careful and extensive validation, it was concluded that the designed micro wind farm is able to capture the main trends in mean row surrogate power, unsteady loading and spatio–temporal correlations in the power outputs. The micro wind farm model is therefore useful for studies of layout optimization and temporal characteristics of the power outputs. In general, it was concluded that using instrumented porous disk models is an efficient approach to study wind farms with over 100 turbines in a wind tunnel setting.

A parametric study of wind farm layout was performed with wind farm measurements for 55 different layouts. For each case, the time signal of the force, from all porous disk models in the three central columns, were measured simultaneously. The arrangements cover a series of layouts with a uniform, a moderately uneven, and an extremely uneven streamwise spacing. These measurements compose a vast data-set which can be used for validation of analytical and numerical models, and further detailed studies of the spatio–temporal interaction with the boundary layer.

For a uniform spacing, the total surrogate power of a staggered farm is higher than for an aligned, but a double staggering performs even better. These results are in good agreement with a previous LES study by Stevens et al. (2014). While the row power shows significant increases in the beginning of the farm by staggering or double staggering rows, at the end of the farm, the mean row power tends to the same asymptotic value for all of these cases, indicating a fully developed regime. A moderately uneven streamwise spacing shows no obvious benefits for the surrogate power or unsteady loading, compared to a uniform spacing. To the contrary, when the models are aligned, significant wake losses reduce the surrogate power in both the entrance and the fully developed region, such that the average asymptote at the end of the farm is lower. Interestingly, an extremely uneven streamwise spacing in a staggered configuration shows a higher surrogate power in both the beginning of the farm, and at the end. These results indicate the possible benefits of spacing small groups of wind turbines closely together. However, as also indicated by the measurements, when porous disk models are aligned with the wind directions, such a non-uniform layout can result in significant wake losses for both the entrance and the fully developed region of the farm.

Finally, the unique spatio-temporal data acquisition capabilities of the setup are used to study the spectrum of the surrogate power and its relation to the correlations of individual power signals. Measurement data for an aligned and staggered layout were analyzed and found to confirm the features observed in the literature (Apt, 2007; Stevens and Meneveau, 2014): the spectrum follows a power-law decrease with a slope close to $-5/3$ and a peak at a frequency related to the travel time between rows. The measured spectrum also indicated that the $-5/3$ power law region extends to lower frequencies than present in

the spectrum of the velocity field. Furthermore, by artificially decorrelating the individual measured power signals, the crucial role of spatio–temporal correlations in producing these spectral features was confirmed. Based on these observations, it was concluded that the spectrum results from a discrete spatial sampling of the spatio–temporal turbulent boundary layer structure. By using an existing model for the wavenumber-frequency spectrum, an analytical model was developed to estimate the spectrum of the wind farm power. The model explains the appearance of a spectral peak and an extended power law region, through the interaction between the spatial sampling transfer function and the wavenumber-frequency spectrum. As such, the model can explain the individual roles of Doppler shift, from advection, and Doppler broadning, or decorrelation of the flow. Validation with wind farm measurements for an aligned and staggered layout showed good agreements, but indicated the possibility for an improvement if the wavenumber-frequency spectrum inside the wind farm can be better represented.

6.2 Future research

The current dissertation introduces the application of instrumented porous disk models for wind tunnel studies of large wind farms. This improved methodology opens many new experimental research opportunities, as it allows to fit wind farms with many models in a wind tunnel, and makes it possible to perform simultaneous measurements of a surrogate for power from each model.

First, it is important to acknowledge the limitations of the current study. The experiments in this work have focused on one specific inflow condition of a neutral developing boundary layer. Several studies have indicated the significant impact of inflow conditions such as thermal stability and boundary layer height on the wake effects and wind farm efficiency (Chamorro and Porté-Agel, 2010; Zhang et al., 2013; Allaerts and Meyers, 2017). Small scale models make it possible to study different inflow conditions easily, as the necessary development length for the boundary layer is reasonably short, e.g. 5 m for the experiments in this dissertation. Future research can thus employ the concept of instrumented porous disk models to study the effects of boundary layer height, surface roughness, or thermal stability on power and unsteady loading of turbines in large wind farms. The measurements in this work were generally performed at a Reynolds number of approximately 2×10^4 (based on hub height velocity and disk diameter). The validation of the setup at this Reynolds number showed reasonably good agreement with high Reynolds number studies in the literature (field experiments and LES), and measurements at higher velocities (not included in this work) resulted in the same trends. However, we suggest to consider this

Reynolds number as a lower bound, as a separate test showed that the thrust coefficient of a single porous disk model in a laminar inflow starts to decrease at an approximately 30% lower Reynolds number. Future studies should thus verify possible Reynolds number effects by using, for instance, larger porous disk models (see the efforts by Charmanski et al. (2014)) or higher velocities.

In the process of designing an instrumented porous disk model, many design parameters play an important role on the final accuracy and frequency response. Based on the experience gained during this work a number of main guidelines can be given to help future designs. First, it is important to consider the trade-off between measurement sensitivity and the frequency response. Increasing the sensitivity by making the tower more flexible will inevitably lower the natural frequency and thus the frequency response. The accuracy can be increased by making the distance between the center of the disk and the location of the strain gage on the tower larger, as this reduces the uncertainty caused by the force-distribution over the disk. Another important design choice is material selection. Certain polymer materials were found not to bond with the strain gage glue. Furthermore, polymers exhibit creep when a force is applied over a long time. It is thus advised to choose a material with less creep, ideally a metal. The porous disk models in this dissertation make use of two strain gages in a half-bridge configuration, a higher accuracy can be reached by using four strain gages in a full bridge configuration. Finally, the resistance changes measured from the strain gages are very small. Our experience showed that an audio jack connection does not always provide a perfect electrical contact. We therefore advice to carefully select an electrical connection with a reliable and low contact-resistance.

The experiments performed in this study, compose a large data-set of power and velocity time-signals, for 55 different layouts. The carefully documented experimental data can now be used for detailed validation of LES and other numerical or analytical models. Such a validation can be of particular interest to study for instance the minimum allowable grid size and the effects of the subgrid scale model in LES. In this dissertation we have merely studied the average power, unsteady loading, and the spectral properties for an aligned and staggered layout. However, the data contains significantly more information. For instance, it can be useful for the study of convection velocities and spatio–temporal correlations in turbulent boundary layers. But also for the study of loads on wind turbines and the detailed effect of wakes on the load statistics. The authors are happy to share measurement data with interested researchers.

Wind energy is inherently variable due to the turbulent nature of the boundary layer. Power variability introduces uncertainty and the need for ancillary services, which need to compensate the fluctuations (Apt, 2007), or control, to follow a reference signal from a grid operator (Shapiro et al., 2016). In this

dissertation, an analytical model for the frequency spectrum of the wind farm power was developed that showed the presence of a peak in the spectrum at time scales corresponding to the travel-time between rows. At that time-scale one can thus expect larger power fluctuations. By making use of this model, it is possible to steer the layout of a wind farm in such a way that it is advantageous for the spectral characteristics of the power variability. Future research can thus consider the incorporation of this model in layout-optimization algorithms to find an optimal layout which reduces both wake effects and output variability.

Intentional yaw misalignment results in a wake deflection which can potentially reduce the wake losses for a downstream turbine (Jiménez et al., 2010). This principle has recently received an increased attention as it can improve the overall farm efficiency (Fleming et al., 2016; Gebraad et al., 2016). The wake deflection of one or a few wind turbines has been studied numerically (Jiménez et al., 2010; Fleming et al., 2014), experimentally (Grant et al., 1997; Adaramola and Krogstad, 2011; Bastankhah and Porté-Agel, 2015) and with field tests (Fleming et al., 2017b). However, wind tunnel studies of dynamic or static yaw control for wind farms with many turbines are challenging, and have not been performed yet. Yawed porous disk models result in a wake deflection similar to that of actual wind turbines (Howland et al., 2016). The micro wind farm setup can thus be used to study the effects of yawing on the power output and unsteady loading. However, one important aspect of the designed porous disk models is that they measure the force perpendicular to the disk. An experiment was performed in which both force components acting on a yawed porous disk were measured. These measurements indicated that the force is not necessarily perpendicular to the disk. A yawed porous disk can thus be considered as a porous circular wing, with a lift and drag coefficient, and for which the tip vortices at the top and bottom result in wake curling (Howland et al., 2016). Thus, to use porous disk models for studies of yawed wind turbines, a relation needs to be defined between the measured forces on the porous disk, and what an actual wind turbine would produce in power. This is still an open challenge.

In section 2.2 the possibility of designing a porous disk with wake rotation is mentioned. As shown with LES (Porté-Agel et al., 2011), wake rotation may improve the agreement with the wake characteristics of an actual wind turbine. Following the approach described in section 2.2, future research can thus focus on the careful design of a porous disk which also matches wake rotation.

Appendix A

Definitions of spectra

In this appendix a brief overview is given of the notations and main definitions of spectra in chapter 5, following the usual conventions in the corresponding literature Wilczek et al. (2015b); Pope (2001).

For statistically stationary and homogneous turbulence, the wavenumber energy spectrum is defined by the Fourier transform of $R_{11}(\mathbf{r}, 0)$:

$$E_k(\mathbf{k}) = \frac{1}{(2\pi)^3} \int R_{11}(\mathbf{r}, 0) \exp(-i\mathbf{k} \cdot \mathbf{r})\, d\mathbf{r}, \tag{A.1}$$

while the energy spectrum in the wavenumber–frequency domain is defined by:

$$E(\mathbf{k}, \omega) = \frac{1}{(2\pi)^4} \iint R_{11}(\mathbf{r}, \tau) \exp(-i\mathbf{k} \cdot \mathbf{r}) \exp(i\omega\tau)\, d\mathbf{r}\, d\tau.) \tag{A.2}$$

Here, $R_{11}(\mathbf{r}, \tau)$ is the two-point and two-time velocity covariance tensor of the streamwise velocity component, defined by:

$$R_{11}(\mathbf{r}, \tau) = \overline{u_1(\mathbf{x}, t) u_1(\mathbf{x} + \mathbf{r}, t + \tau)}. \tag{A.3}$$

In this paper we do not consider filtering in the vertical direction. The energy spectra in the horizontal plane are found by integrating the full energy spectra over k_3:

$$E_{kk}(k_1, k_2) = \int E_k(\mathbf{k})\, dk_3, \tag{A.4}$$

$$\Phi_{11}(k_1, k_2, \omega) = \int E(\mathbf{k}, \omega)\, dk_3. \tag{A.5}$$

Further, we also use:

$$E_\omega = \iint \Phi_{11}(k_1, k_2, \omega)\, dk_1\, dk_2 \tag{A.6}$$

$$E_{k\omega} = \int \Phi_{11}\, dk_2 \tag{A.7}$$

Appendix B

Calculation of the spatial transfer function

This appendix describes the derivation of the spatial transfer function defined in chapter 5. The transfer function is calculated by applying 2π times the Fourier transform to the physical space sampling function, in each direction Pope (2001):

$$\hat{g}(k_1, k_2) = \int_{-\infty}^{\infty} \int_{-\infty}^{\infty} g(x, y) \exp(-ik_1 x) \exp(-ik_2 y)\, dx\, dy. \tag{B.1}$$

Inserting the sampling function $g(x, y)$ and separating the integrals leads to:

$$\begin{aligned} \hat{g}(k_1, k_2) &= \sum_{i=1}^{N} \int_{-\infty}^{\infty} \delta(x - x_i) \exp(-ik_1 x)\, dx \\ &\quad \int_{-\infty}^{\infty} \frac{1}{D} H\left(\frac{D}{2} - |y - y_i|\right) \exp(-ik_2 y)\, dy, \end{aligned} \tag{B.2}$$

and:

$$\begin{aligned} \hat{g}(k_1, k_2) &= \frac{i}{k_2 D} \sum_{i=1}^{N} \exp(-ik_1 x_i) \\ &\quad \left[\exp\left(-ik_2(y_i + \frac{D}{2})\right) - \exp\left(-ik_2(y_i - \frac{D}{2})\right)\right]. \end{aligned} \tag{B.3}$$

By making use of Eulers formula for complex exponentials the exponentials can be combined:

$$\hat{g}(k_1, k_2) = \frac{\sin\left(k_2 \frac{D}{2}\right)}{k_2 \frac{D}{2}} \sum_{i=1}^{N} \exp\left(-i(k_1 x_i + k_2 y_i)\right). \tag{B.4}$$

The transfer function for the sampling of the energy spectrum $|\widehat{g}|^2$ is given by:

$$\begin{aligned} |\widehat{g}|^2 = \widehat{g}\widehat{g}^* &= \left(\frac{\sin\left(k_2 \frac{D}{2}\right)}{k_2 \frac{D}{2}}\right)^2 \left[\left(\sum_{i=1}^{N} \cos\left(k_1 x_i + k_2 y_i\right)\right)^2 + \right. \\ &\quad \left. \left(\sum_{i=1}^{N} \sin\left(k_1 x_i + k_2 y_i\right)\right)^2 \right], \end{aligned} \tag{B.5}$$

and is equal to:

$$\begin{aligned} |\widehat{g}|^2 &= \left(\frac{\sin\left(k_2 \frac{D}{2}\right)}{k_2 \frac{D}{2}}\right)^2 \left(\sum_{i=1}^{N}\sum_{j=1}^{N} \left(\cos\left(k_1 x_i + k_2 y_i\right)\cos\left(k_1 x_j + k_2 y_j\right) + \right.\right. \\ &\quad \left.\left. \sin\left(k_1 x_i + k_2 y_i\right)\sin\left(k_1 x_j + k_2 y_j\right) \right)\right). \end{aligned} \tag{B.6}$$

By making use of the trigonometric identities: $2\cos(a)\cos(b) = \cos(a-b) + \cos(a+b)$ and $2\sin(a)\sin(b) = \cos(a-b) - \cos(a+b)$, this can be simplified to:

$$\begin{aligned} |\widehat{g}(k_1, k_2)|^2 &= \left(\frac{\sin\left(k_2 \frac{D}{2}\right)}{k_2 \frac{D}{2}}\right)^2 \left(\sum_{i=1}^{N}\sum_{j=1}^{N} \cos\left(k_1\left(x_i - x_j\right) + \right.\right. \\ &\quad \left.\left. k_2\left(y_i - y_j\right)\right)\right). \end{aligned} \tag{B.7}$$

For the special case of one streamwise column of N wind turbines with spacing S_x, the sum in equation B.4 becomes the geometric series: $\sum_{n=0}^{N-1} \exp(-inS_x k_1) = (1 - \exp(-iNS_x k_1))/(1 - \exp(-iS_x k_1))$ so that:

$$\hat{g}(k_1, k_2) = \frac{\sin\left(k_2 \frac{D}{2}\right)}{k_2 \frac{D}{2}} \frac{1 - \exp(-iNS_x k_1)}{1 - \exp(-iS_x k_1)}, \tag{B.8}$$

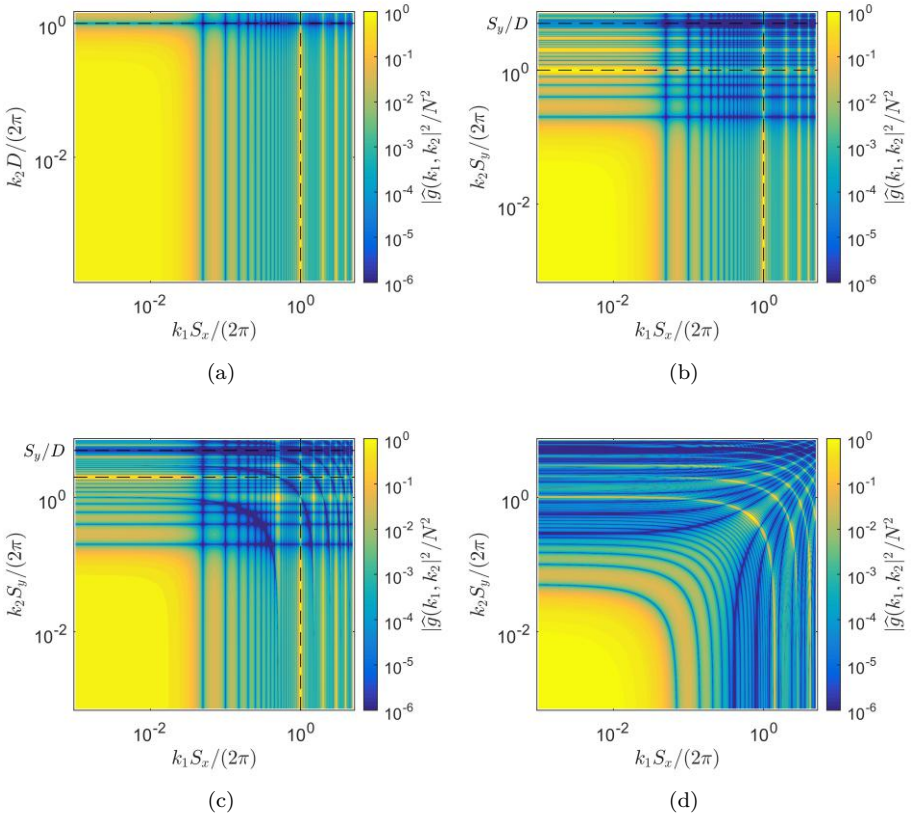

Figure B.1: The spatial sampling transfer function $|\widehat{g}(k_1, k_2)|^2/N^2$ for a single streamwise column with 20 wind turbines (a), an aligned wind farm with 20 rows and 5 columns (b), a staggered wind farm with 20 rows and 5 columns (c) and the aligned wind farm rotated 45^o with the k_1 direction (d).

and

$$|\widehat{g}(k_1,k_2)|^2 = \left(\frac{\sin\left(k_2\frac{D}{2}\right)}{k_2\frac{D}{2}}\right)^2 \left(\frac{\sin\left(\frac{k_1 S_x N}{2}\right)}{\sin\left(\frac{k_1 S_x}{2}\right)}\right)^2 . \tag{B.9}$$

Figure B.1 shows the transfer function calculated with equation B.7 for several cases that are representative for the experimental setup, as described in section 5.1. Figure B.1 (a) is for a single streamwise column with 20 wind turbines, spaced evenly with S_x. A peak at $k_1 = 2\pi/S_x$ is observed in the streamwise direction. In the spanwise direction, the box filter by the turbine diameter can be noticed. Figure B.1 (b) is for an aligned wind farm with 20 spanwise rows and 5 streamwise columns, spaced evenly in the streamwise direction with S_x and in the spanwise direction with S_y. In the spanwise direction, the filter also shows a peak at $k_2 = 2\pi/S_y$. Figure B.1 (c) considers a staggered wind farm by shifting the even rows with $S_y/2$ in the spanwise direction. The peak in the spanwise direction has now shifted to $k_2 = 4\pi/S_y$, because of the smaller apparent spanwise spacing. An extra peak is observed at $k_1 = \pi/S_x$ and $k_2 = 2\pi/S_x$, representative for the streamwise aligned wind turbines which have now a spacing of $2S_x$. Figure B.1 (d) is for the aligned wind farm, angled 45^o compared to the k_1 direction, as an example for a different wind direction.

Bibliography

Adaramola, M. and P.-Å. Krogstad
2011. Experimental investigation of wake effects on wind turbine performance. *Renewable Energy*, 36(8):2078–2086.

Aho, J., A. Buckspan, J. Laks, P. Fleming, Y. Jeong, F. Dunne, M. Churchfield, L. Pao, and K. Johnson
2012. A tutorial of wind turbine control for supporting grid frequency through active power control. In *American Control Conference (ACC), 2012*, Pp. 3120–3131. IEEE.

Allaerts, D. and J. Meyers
2017. Boundary-layer development and gravity waves in conventionally neutral wind farms. *Journal of Fluid Mechanics*, 814:95–130.

Apt, J.
2007. The spectrum of power from wind turbines. *Journal of Power Sources*, 169(2):369–374.

Archer, C. L., S. Mirzaeisefat, and S. Lee
2013. Quantifying the sensitivity of wind farm performance to array layout options using large-eddy simulation. *Geophysical Research Letters*, 40(18):4963–4970.

Aubrun, S., G. Espana, S. Loyer, P. Hayden, and P. Hancock
2012. Is the actuator disc concept sufficient to model the far-wake of a wind turbine? In *Progress in Turbulence and Wind Energy IV*, volume 141, Pp. 227–230.

Aubrun, S., S. Loyer, P. Hancock, and P. Hayden
2013. Wind turbine wake properties: Comparison between a non-rotating simplified wind turbine model and a rotating model. *Journal of Wind Engineering and Industrial Aerodynamics*, 120:1 – 8.

Bandi, M. M.
2017. Spectrum of wind power fluctuations. *Phys. Rev. Lett.*, 118:028301.

Banta, R. M., Y. L. Pichugina, W. A. Brewer, J. K. Lundquist, N. D. Kelley, S. P. Sandberg, R. J. Alvarez II, R. M. Hardesty, and A. M. Weickmann
2015. 3D volumetric analysis of wind turbine wake properties in the atmosphere using high-resolution doppler lidar. *Journal of Atmospheric and Oceanic Technology*, 32(5):904–914.

Barlas, E., S. Buckingham, and J. van Beeck
2016. Roughness effects on wind-turbine wake dynamics in a boundary-layer wind tunnel. *Boundary-layer meteorology*, 158(1):27–42.

Barthelmie, R. J., S. T. Frandsen, O. Rathmann, K. S. Hansen, E. Politis, J. Prospathopoulos, J. Schepers, K. Rados, D. Cabezón, W. Schlez, et al.
2011. Flow and wakes in large wind farms: Final report for upwind WP8. Technical report, Danmarks Tekniske Universitet, Risø Nationallaboratoriet for Bæredygtig Energi.

Barthelmie, R. J., S. Pryor, S. T. Frandsen, K. S. Hansen, J. Schepers, K. Rados, W. Schlez, A. Neubert, L. Jensen, and S. Neckelmann
2010. Quantifying the impact of wind turbine wakes on power output at offshore wind farms. *Journal of Atmospheric and Oceanic Technology*, 27(8):1302–1317.

Barthelmie, R. J., O. Rathmann, S. T. Frandsen, K. Hansen, E. Politis, J. Prospathopoulos, K. Rados, D. Cabezón, W. Schlez, J. Phillips, et al.
2007. Modelling and measurements of wakes in large wind farms. In *Journal of Physics: Conference Series*, volume 75, P. 012049. IOP Publishing.

Bartl, J., F. Pierella, and L. Sætrana
2012. Wake measurements behind an array of two model wind turbines. *Energy Procedia*, 24:305–312.

Bastankhah, M. and F. Porté-Agel
2015. A wind-tunnel investigation of wind-turbine wakes in yawed conditions. In *Journal of Physics: Conference Series*, volume 625, P. 012014. IOP Publishing.

Bastankhah, M. and F. Porté-Agel
2017. A new miniature wind turbine for wind tunnel experiments. part i: Design and performance. *Energies*, 10(7):908.

Blocken, B., T. Defraeye, E. Koninckx, J. Carmeliet, and P. Hespel
2013. Surprises in cycling aerodynamics. *Europhysics News*, 44(1):20–23.

Bokharaie, V. S., P. Bauweraerts, and J. Meyers
2016. Wind-farm layout optimisation using a hybrid Jensen-LES approach. *Wind Energy Science*, 1(2):311.

Bottasso, C. L., F. Campagnolo, and V. Petrović
2014. Wind tunnel testing of scaled wind turbine models: Beyond aerodynamics. *Journal of wind engineering and industrial aerodynamics*, 127:11–28.

Builtjes, P.
1979. *Windturbine Wake Effects*. Division of Technology for Society, Netherlands Organization for Applied Scientific Research.

Burton, T., D. Sharpe, N. Jenkins, and E. Bossanyi
2001. *Wind energy handbook*. John Wiley & Sons.

Cal, R. B., J. Lebrón, L. Castillo, H. S. Kang, and C. Meneveau
2010. Experimental study of the horizontally averaged flow structure in a model wind-turbine array boundary layer. *Journal of Renewable and Sustainable Energy*, 2(1):013106.

Calaf, M., C. Meneveau, and J. Meyers
2010. Large eddy simulation study of fully developed wind-turbine array boundary layers. *Physics of fluids*, 22(1):015110.

Camp, E. H. and R. B. Cal
2016. Mean kinetic energy transport and event classification in a model wind turbine array versus an array of porous disks: Energy budget and octant analysis. *Physical Review Fluids*, 1(4):044404.

Castro, I.
1971. Wake characteristics of two-dimensional perforated plates normal to an air-stream. *Journal of Fluid Mechanics*, 46(03):599–609.

Chamorro, L. P., R. Arndt, and F. Sotiropoulos
2012. Reynolds number dependence of turbulence statistics in the wake of wind turbines. *Wind Energy*, 15(5):733–742.

Chamorro, L. P., R. E. Arndt, and F. Sotiropoulos
2011. Turbulent flow properties around a staggered wind farm. *Boundary-layer meteorology*, 141(3):349–367.

Chamorro, L. P. and F. Porté-Agel
2010. Effects of thermal stability and incoming boundary-layer flow characteristics on wind-turbine wakes: a wind-tunnel study. *Boundary-layer meteorology*, 136(3):515–533.

Chamorro, L. P. and F. Porté-Agel
2011. Turbulent flow inside and above a wind farm: A wind-tunnel study. *Energies*, 4(11):1916.

Charmanski, K., J. Turner, and M. Wosnik
2014. Physical model study of the wind turbine array boundary layer. In *ASME 2014 4th Joint US-European Fluids Engineering Division Summer Meeting collocated with the ASME 2014 12th International Conference on Nanochannels, Microchannels, and Minichannels*, Pp. V01DT39A010–V01DT39A010. American Society of Mechanical Engineers.

Chen, Y., H. Li, K. Jin, and Q. Song
2013. Wind farm layout optimization using genetic algorithm with different hub height wind turbines. *Energy Conversion and Management*, 70:56–65.

Chowdhury, S., J. Zhang, A. Messac, and L. Castillo
2012. Unrestricted wind farm layout optimization (uwflo): Investigating key factors influencing the maximum power generation. *Renewable Energy*, 38(1):16–30.

Cook, N.
1978. Determination of the model scale factor in wind-tunnel simulations of the adiabatic atmospheric boundary layer. *Journal of Wind Engineering and Industrial Aerodynamics*, 2(4):311–321.

Corten, G. P., P. Schaak, and T. Hegberg
2004. Turbine interaction in large offshore wind farms. Wind Tunnel Measurements. *ECN report ECN-C-04-048*.

Coudou, N., S. Buckingham, and J. van Beeck
2017. Experimental study on the wind-turbine wake meandering inside a scale model wind farm placed in an atmospheric-boundary-layer wind tunnel. *Journal of Physics: Conference Series*, 854(1):012008.

Counihan, J.
1975. Adiabatic atmospheric boundary layers: a review and analysis of data from the period 1880–1972. *Atmospheric Environment (1967)*, 9(10):871–905.

Crespo, A., J. Hernández, and S. Frandsen
1999. Survey of modelling methods for wind turbine wakes and wind farms. *Wind Energy*, 2:1–24.

Dahlberg, J.-A.
2009. Assessment of the Lillgrund wind farm: power performance wake effects. *Vattenfall Vindkraft AB, 6_1 LG Pilot Report*.

De Graaff, D. B. and J. K. Eaton
2000. Reynolds-number scaling of the flat-plate turbulent boundary layer. *Journal of Fluid Mechanics*, 422:319–346.

Delport, S., M. Baelmans, and J. Meyers
2009. Constrained optimization of turbulent mixing-layer evolution. *Journal of Turbulence*, (10):N18.

Du Pont, B. L. and J. Cagan
2012. An extended pattern search approach to wind farm layout optimization. *Journal of Mechanical Design*, 134(8):081002.

Ebert, P. R. and D. H. Wood
1997. The near wake of a model horizontal-axis wind turbine - I. Experimental arrangements and initial results. *Renewable Energy*, 12:225.

ESDU
1985. Characteristics of atmospheric turbulence near the ground, Part II: single point data for strong winds (neutral atmosphere).

España, G., S. Aubrun, S. Loyer, and P. Devinant
2011. Spatial study of the wake meandering using modelled wind turbines in a wind tunnel. *Wind Energy*, 14(7):923–937.

Farr, T. and P. Hancock
2014. Torque fluctuations caused by upstream mean flow and turbulence. In *Journal of Physics: Conference Series*, volume 555, P. 012048. IOP Publishing.

Fleming, P., J. Annoni, A. Scholbrock, E. Quon, S. Dana, S. Schreck, S. Raach, F. Haizmann, and D. Schlipf
2017a. Full-scale field test of wake steering. In *Wake Conference, Visby, Sweden*.

Fleming, P., J. Annoni, A. Scholbrock, E. Quon, S. Dana, S. Schreck, S. Raach, F. Haizmann, and D. Schlipf
2017b. Full-scale field test of wake steering. *Journal of Physics: Conference Series*, 854(1):012013.

Fleming, P. A., P. M. Gebraad, S. Lee, J.-W. van Wingerden, K. Johnson, M. Churchfield, J. Michalakes, P. Spalart, and P. Moriarty
2014. Evaluating techniques for redirecting turbine wakes using SOWFA. *Renewable Energy*, 70:211–218.

Fleming, P. A., A. Ning, P. M. Gebraad, and K. Dykes
2016. Wind plant system engineering through optimization of layout and yaw control. *Wind Energy*, 19(2):329–344.

Frandsen, S.
1992. On the wind speed reduction in the center of large clusters of wind turbines. *J. of Wind Engineering & industrial aerodynamics*, 39:251–265.

Ganapathisubramani, B., N. Hutchins, W. Hambleton, E. Longmire, and I. Marusic
2005. Investigation of large-scale coherence in a turbulent boundary layer using two-point correlations. *Journal of Fluid Mechanics*, 524:57–80.

Gaumond, M., P.-E. Réthoré, S. Ott, A. Pena, A. Bechmann, and K. S. Hansen
2014. Evaluation of the wind direction uncertainty and its impact on wake modeling at the Horns Rev offshore wind farm. *Wind Energy*, 17(8):1169–1178.

Gebraad, P., F. Teeuwisse, J. Wingerden, P. A. Fleming, S. Ruben, J. Marden, and L. Pao
2016. Wind plant power optimization through yaw control using a parametric model for wake effects—a CFD simulation study. *Wind Energy*, 19(1):95–114.

Grant, A.
1986. Observations of boundary layer structure made during the 1981 kontur experiment. *Quarterly Journal of the Royal Meteorological Society*, 112(473):825–841.

Grant, I., P. Parkin, and X. Wang
1997. Optical vortex tracking studies of a horizontal axis wind turbine in yaw using laser-sheet, flow visualisation. *Experiments in Fluids*, 23(6):513–519.

Guo, J., Y. Miao, Y. Zhang, H. Liu, Z. Li, W. Zhang, J. He, M. Lou, Y. Yan, L. Bian, et al.
2016. The climatology of planetary boundary layer height in china derived from radiosonde and reanalysis data. *Atmos. Chem. Phys. Discuss., doi*, 10.

Hansen, K. S., R. J. Barthelmie, L. E. Jensen, and A. Sommer
2012. The impact of turbulence intensity and atmospheric stability on power deficits due to wind turbine wakes at Horns Rev wind farm. *Wind Energy*, 15(1):183–196.

Herges, T., D. Maniaci, B. Naughton, T. Mikkelsen, and M. Sjöholm
2017. High resolution wind turbine wake measurements with a scanning lidar. In *EWEA Wake Conference, To Be Published*.

Howland, M. F., J. Bossuyt, L. A. Martínez-Tossas, J. Meyers, and C. Meneveau
2016. Wake structure in actuator disk models of wind turbines in yaw under uniform inflow conditions. *Journal of Renewable and Sustainable Energy*, 8(4):043301.

Hutchins, N. and I. Marusic
2007. Evidence of very long meandering features in the logarithmic region of turbulent boundary layers. *Journal of Fluid Mechanics*, 579:1–28.

Hutchins, N., T. B. Nickels, I. Marusic, and M. Chong
2009. Hot-wire spatial resolution issues in wall-bounded turbulence. *Journal of Fluid Mechanics*, 635:103–136.

IEA
2016. Key world energy statistics.

Jiménez, Á., A. Crespo, and E. Migoya
2010. Application of a LES technique to characterize the wake deflection of a wind turbine in yaw. *Wind energy*, 13(6):559–572.

Kaimal, J. C., J. Wyngaard, Y. Izumi, and O. Coté
1972. Spectral characteristics of surface-layer turbulence. *Quarterly Journal of the Royal Meteorological Society*, 98(417):563–589.

Kang, H. and C. Meneveau
2010. Direct mechanical torque sensor for model wind turbines. *Meas. Sci. Technol.*, 21:105206.

Katic, I., J. Højstrup, and N. O. Jensen
1986. A simple model for cluster efficiency. In *European wind energy association conference and exhibition*, Pp. 407–410.

Katzenstein, W., E. Fertig, and J. Apt
2010. The variability of interconnected wind plants. *Energy Policy*, 38(8):4400–4410.

Kolmogorov, A. N.
1941. The local structure of turbulence in incompressible viscous fluid for very large reynolds numbers. In *Dokl. Akad. Nauk SSSR*, volume 30, Pp. 299–303.

Krogstad, P.-Å. and M. S. Adaramola
2012. Performance and near wake measurements of a model horizontal axis wind turbine. *Wind Energy*, 15(5):743–756.

Lackner, M. A. and C. N. Elkinton
2007. An analytical framework for offshore wind farm layout optimization. *Wind Engineering*, 31(1):17–31.

Larsén, X. G., S. E. Larsen, and E. L. Petersen
2016. Full-scale spectrum of boundary-layer winds. *Boundary-Layer Meteorology*, 159(2):349–371.

Lavoie, P., G. Avallone, F. De Gregorio, G. Romano, and R. Antonia
2007. Spatial resolution of PIV for the measurement of turbulence. *Experiments in Fluids*, 43(1):39–51.

Lebrón, J., R. B. Cal, H.-S. Kang, L. Castillo, and C. Meneveau
2009. Interaction between a wind turbine array and a turbulent boundary layer. *11th Americas Conference on Wind Engineering*.

Lignarolo, L., D. Ragni, C. Krishnaswami, Q. Chen, C. S. Ferreira, and G. Van Bussel
2014a. Experimental analysis of the wake of a horizontal-axis wind-turbine model. *Renewable Energy*, 70:31–46.

Lignarolo, L., D. Ragni, C. Simao Ferreira, and G. J. van Bussel
2015. Wind turbine and actuator disc wake: two experimental campaigns. In *Proceedings of the 14th International Conference on Wind Engineering, ICWE14, Porto Alegre (Brasil), June 21-26, 2015*. UFRGS.

Lignarolo, L., D. Ragni, G. van Bussel, et al.
2014b. Kinetic energy entrainment in wind turbine and actuator disc wakes: an experimental analysis. In *Journal of Physics: Conference Series*, volume 524, P. 012163. IOP Publishing.

Lignarolo, L. E., D. Mehta, R. J. Stevens, A. E. Yilmaz, G. van Kuik, S. J. Andersen, C. Meneveau, C. J. Ferreira, D. Ragni, J. Meyers, et al.
2016. Validation of four LES and a vortex model against stereo-PIV measurements in the near wake of an actuator disc and a wind turbine. *Renewable energy*, 94:510–523.

Lim, H. C., I. P. Castro, and R. P. Hoxey
2007. Bluff bodies in deep turbulent boundary layers: Reynolds-number issues. *Journal of Fluid Mechanics*, 571:97–118.

Lissaman, P.
1979. Energy effectiveness of arbitrary arrays of wind turbines. *J. Energy*, 3(6):323–328.

Maeda, T., Y. Kamada, J. Murata, S. Yonekura, T. Ito, A. Okawa, and T. Kogaki
2011. Wind tunnel study on wind and turbulence intensity profiles in wind turbine wake. *Journal of Thermal Science*, 20(2):127–132.

Maidanik, G. and D. Jorgensen
1967. Boundary wave-vector filters for the study of the pressure field in a turbulent boundary layer. *The Journal of the Acoustical Society of America*, 42(2):494–501.

Martínez-Tossas, L., M. Churchfield, and C. Meneveau
2017. Optimal smoothing length scale for actuator line models of wind turbine blades based on gaussian body force distribution. *Wind Energy*, 20(6):1083–1096.

Martínez-Tossas, L. A., M. J. Churchfield, and C. Meneveau
2015. Large eddy simulation of wind turbine wakes: detailed comparisons of two codes focusing on effects of numerics and subgrid modeling. In *Journal of Physics: Conference Series*, volume 625, P. 012024. IOP Publishing.

McTavish, S., D. Feszty, and F. Nitzsche
2014. An experimental and computational assessment of blockage effects on wind turbine wake development. *Wind Energy*, 17(10):1515–1529.

Medici, D. and P. H. Alfredsson
2006. Measurements on a wind turbine wake: 3D effects and bluff body vortex shedding. *Wind Energy*, 9(3):219–236.

Mehta, D., A. H. Van Zuijlen, B. Koren, J. G. Holierhoek, and H. Bijl
2014. Large eddy simulation of wind farm aerodynamics: A review. *J. Wind Eng. and Industrial Aerodynamics*, 133:1–17.

Meneveau, C.
2012. The top-down model of wind farm boundary layers and its applications. *Journal of Turbulence*, (13):N7.

Meyers, J. and C. Meneveau
2012. Optimal turbine spacing in fully developed wind farm boundary layers. *Wind Energy*, 15:305–317.

Meyers, J. and P. Sagaut
2007. Evaluation of smagorinsky variants in large-eddy simulations of wall-resolved plane channel flows. *Physics of Fluids*, 19(9):095105.

Mikkelsen, R.
2003. Actuator disc methods applied to wind turbines. *Technical University of Denmark*.

Milan, P., M. Wächter, and J. Peinke
2013. Turbulent character of wind energy. *Physical review letters*, 110(13):138701.

Milborrow, D.
1980. The performance of arrays of wind turbines. *Journal of Wind Engineering and Industrial Aerodynamics*, 5(3-4):403–430.

Miller, M., J. Kiefer, C. Westergaard, and M. Hultmark
2016. Model wind turbines tested at full-scale similarity. In *Journal of Physics: Conference Series*, volume 753, P. 032018. IOP Publishing.

Mohamed, M. S. and J. C. LaRue
1990. The decay power law in grid-generated turbulence. *Journal of Fluid Mechanics*, 219:195–214.

Munters, W., C. Meneveau, and J. Meyers
2016a. Shifted periodic boundary conditions for simulations of wall-bounded turbulent flows. *Physics of Fluids*, 28(2):025112.

Munters, W., C. Meneveau, and J. Meyers
2016b. Turbulent inflow precursor method with time-varying direction for large-eddy simulations and applications to wind farms. *Boundary-layer meteorology*, 159(2):305–328.

Muraca, R. J. and R. J. Guillotte
1976. Wind tunnel investigation of a 14 foot vertical axis windmill.

Nickels, T. B., I. Marusic, S. Hafez, and M. S. Chong
2005. Evidence of the $k-1$ law in a high-reynolds-number turbulent boundary layer. *Physical review letters*, 95(7):074501.

Nygaard, N. G.
2014. Wakes in very large wind farms and the effect of neighbouring wind farms. In *Journal of Physics: Conference Series*, volume 524, P. 012162. IOP Publishing.

Odemark, Y.
2012. Wakes behind wind turbines-studies on tip vortex evolution and stability.

Pena, A., P.-E. Réthoré, C. B. Hasager, and K. S. Hansen
2013. Results of wake simulations at the Horns Rev I and Lillgrund wind farms using the modified park model. Technical report, DTU Wind Energy.

Pillai, A. C., J. Chick, M. Khorasanchi, S. Barbouchi, and L. Johanning
2017. Application of an offshore wind farm layout optimization methodology at Middelgrunden wind farm. *Ocean Engineering*, 139:287–297.

Pope, S. B.
2001. Turbulent flows.

Porté-Agel, F., Y. Wu, H. Lu, and R. J. Conzemius
2011. Large-eddy simulation of atmospheric boundary layer flow through wind turbines and wind farms. *J. Wind Eng. and Industrial Aerodynamics*, 99(4):154–168.

Porté-Agel, F., Y.-T. Wu, and C.-H. Chen
2013. A numerical study of the effects of wind direction on turbine wakes and power losses in a large wind farm. *Energies*, 6(10):5297–5313.

Sanderse, B., S. P. van der Pijl, and B. Koren
2011. Review of computational fluid dynamics for wind turbine wake aerodynamics. *Wind Energy*, 14:799–819.

Schreck, S.
2002. The NREL full-scale wind tunnel experiment introduction to the special issue. *Wind Energy*, 5(2-3):77–84.

Seidel, D. J., Y. Zhang, A. Beljaars, J.-C. Golaz, A. R. Jacobson, and B. Medeiros
2012. Climatology of the planetary boundary layer over the continental united states and Europe. *Journal of Geophysical Research: Atmospheres*, 117(D17).

Shapiro, C. R., J. Meyers, C. Meneveau, and D. F. Gayme
2016. Wind farms providing secondary frequency regulation: Evaluating the performance of model-based receding horizon control. In *Journal of Physics: Conference Series*, volume 753, P. 052012. IOP Publishing.

Shen, W. Z. and J. Sørensen
2002. Numerical modeling of wind turbine wakes. *J. Fluids Eng*, 124(2):393–399.

Sørensen, P., A. D. Hansen, and P. A. C. Rosas
2002. Wind models for simulation of power fluctuations from wind farms. *Journal of wind engineering and industrial aerodynamics*, 90(12):1381–1402.

Sorensen, P. and T. Nielsen
2006. Recalibrating wind turbine wake model parameters—validating the wake model performance for large offshore wind farms. In *European Wind Energy Conference and Exhibition, EWEA*.

Stevens, R. J., D. F. Gayme, and C. Meneveau
2016a. Generalized coupled wake boundary layer model: applications and comparisons with field and LES data for two wind farms. *Wind Energy*, 19(11):2023–2040.

Stevens, R. J. A. M.
2016. Dependence of optimal wind turbine spacing on wind farm length. *Wind energy*, 19(4):651–663.

Stevens, R. J. A. M., D. Gayme, and C. Meneveau
2014. Large eddy simulation studies of the effects of alignment and wind farm length. *J. Renewable and Sustainable Energy*, 6(2):023105.

Stevens, R. J. A. M., D. F. Gayme, and C. Meneveau
2016b. Effects of turbine spacing on the power output of extended wind-farms. *Wind Energy*, 19(2):359–370.

Stevens, R. J. A. M. and C. Meneveau
2014. Temporal structure of aggregate power fluctuations in large-eddy simulations of extended wind-farms. *Journal of Renewable and Sustainable Energy*, 6(4).

Stevens, R. J. A. M. and C. Meneveau
2017. Flow structure and turbulence in wind farms. *Annual review of fluid mechanics*, 49:311–339.

Talluru, K., V. Kulandaivelu, N. Hutchins, and I. Marusic
2014. A calibration technique to correct sensor drift issues in hot-wire anemometry. *Measurement Science and Technology*, 25(10):105304.

Theunissen, R., P. Housley, C. B. Allen, and C. Carey
2015. Experimental verification of computational predictions in power generation variation with layout of offshore wind farms. *Wind Energy*, 18(10).

Thormann, A. and C. Meneveau
2014. Decay of homogeneous, nearly isotropic turbulence behind active fractal grids. *Physics of Fluids (1994-present)*, 26(2):025112.

Thormann, A. and C. Meneveau
2015. Decaying turbulence in the presence of a shearless uniform kinetic energy gradient. *Journal of Turbulence*, 16(5):442–459.

Tjernström, M. and A.-S. Smedman
1993. The vertical turbulence structure of the coastal marine atmospheric boundary layer. *Journal of Geophysical Research: Oceans*, 98(C3):4809–4826.

United Nations
2015. Paris agreement.

VDI-guideline 3783/12
2000. Environmental meteorology— physical modelling of flow and dispersion processes in the atmospheric boundary layer, applications of wind tunnels.

Vermeer, L. J., J. N. SØrensen, and A. Crespo
2003. Wind turbine wake aerodynamics. *Progress in Aerospace Sciences*, 39:467–510.

Vermeulen, P.
1978. *A Wind Tunnel Study of the Wake of a Horizontal Axis Wind Turbine: Report*. TNO.

Vestergaard, J., L. Brandstrup, and R. D. Goddard
2004. A brief history of the wind turbine industries in denmark and the united states. In *Academy of international business (Southeast USA Chapter) Conference proceedings*, Pp. 322–327. Academy of International Business.

Vigueras-Rodríguez, A., P. Sørensen, N. A. Cutululis, A. Viedma, and M. Donovan
2010. Wind model for low frequency power fluctuations in offshore wind farms. *Wind Energy*, 13(5):471–482.

Walker, K., N. Adams, B. Gribben, B. Gellatly, N. G. Nygaard, A. Henderson, M. Marchante Jiménez, S. R. Schmidt, J. Rodriguez Ruiz, D. Paredes, et al.
2016. An evaluation of the predictive accuracy of wake effects models for offshore wind farms. *Wind Energy*, 19(5):979–996.

Whale, J., C. G. Anderson, R. Bareiss, and S. Wagner
2000. An experimental and numerical study of the vortex structure in the wake of a wind turbine. *J. Wind Eng. Ind. Aerodyn.*, 84:1.

Wieringa, J.
1992. Updating the davenport roughness classification. *Journal of Wind Engineering and Industrial Aerodynamics*, 41(1-3):357–368.

Wilczek, M., R. J. A. M. Stevens, and C. Meneveau
2015a. Height-dependence of spatio-temporal spectra of wall-bounded turbulence–LES results and model predictions. *Journal of turbulence*, 16(10):937–949.

Wilczek, M., R. J. A. M. Stevens, and C. Meneveau
2015b. Spatio-temporal spectra in the logarithmic layer of wall turbulence: large-eddy simulations and simple models. *Journal of fluid mechanics*, 769.

WindEurope
2016. The european offshore wind industry - key trends and statistics.

Wu, Y. and F. Porté-Agel
2011. Large-eddy simulation of wind-turbine wakes: evaluation of turbine parametrizations. *Boundary-Layer Meteorology*, 138(3):345–366.

Wu, Y.-T. and F. Porté-Agel
2013. Simulation of turbulent flow inside and above wind farms: model validation and layout effects. *Boundary-Layer Meteorology*, Pp. 1–25.

Wyngaard, J.
1968. Measurement of small-scale turbulence structure with hot wires. *Journal of Physics E: Scientific Instruments*, 1(11):1105.

Yang, X., S. Kang, and F. Sotiropoulos
2012. Computational study and modeling of turbine spacing effects in infinite aligned wind farms. *Phys. Fluids*, 24(11):115107.

Zhang, W., C. Markfort, and F. Porté-Agel
2012. Near-wake flow structure downwind of a wind turbine in a turbulent boundary layer. *Experiments in Fluids*, 52(5).

Zhang, W., C. D. Markfort, and F. Porté-Agel
2013. Wind-turbine wakes in a convective boundary layer: a wind-tunnel study. *Boundary-layer meteorology*, Pp. 1–19.

List of publications

International peer reviewed journal articles

- Bossuyt J., Meneveau C., Meyers J. (2017). Wind farm power fluctuations and spatial sampling of turbulent boundary layers. Journal of Fluid Mechanics, 823, 329-344.
- Bossuyt J., Howland M., Meneveau C., Meyers J. (2017). Measurement of unsteady loading and power output variability in a micro wind farm model in a wind tunnel. Experiments in Fluids, 58, art.nr. 1, 1-17.
- Howland M., Bossuyt J., Martínez-Tossas L., Meyers J., Meneveau C. (2016). Wake structure in actuator disk models of wind turbines in yaw under uniform inflow conditions. Journal of Renewable and Sustainable Energy, 8, art.nr. 043301.

Papers at international scientific conferences and symposia

- Bossuyt J., Howland M., Meneveau C., Meyers J. (2016). Wind tunnel study of the power output spectrum in a micro wind farm. Journal of Physics - Conference Series: Vol. 753 (7). Torque 2016. Munich, 5-7 October 2016 (art.nr. doi:10.1088/1742-6596/753/7/072002) Institute of Physics Publishing Ltd.
- Bossuyt J., Howland M., Meneveau C., Meyers J. (2016). Measuring power output intermittency and unsteady loading in a micro wind farm model. AIAA paper 2016-1992. 34th Wind Energy Symposium, AIAA SciTech. San Diego, CA, USA, 4-8 January 2016 (pp. 1-10).

Abstracts presented at international scientific conferences and symposia

- Bossuyt J., Meneveau C., Meyers J. (2017). Relating the wind farm power fluctuation spectrum to the space-time spectral properties of a turbulent boundary layer. Wind Energy Science Conference 2017. Technical University of Denmark, Lyngby, 26-29 June 2017.
- Bossuyt J., Howland M., Meneveau C., Meyers J. (2016). Wind tunnel measurements of a large wind farm model approaching the infinite wind farm regime. 69th Annual Meeting of the APS Division of Fluid Dynamics. Portland, Oregon, 20-22 November 2016, Abstract No. H2.00008.
- Bossuyt J., Howland M., Meneveau C., Meyers J. (2016). Power output variability of a micro wind farm - a wind tunnel study. WINDFARMS 2016. The University of Texas Dallas, 23-25 May 2016.
- Bossuyt J., Howland M., Meneveau C., Meyers J. (2015). Wind tunnel measurements of the power output variability and unsteady loading in a micro wind farm model: vol. 60 (21). Annual Meeting of the APS Division of Fluid Dynamics. Boston, Massachusetts, USA, 22-24 November 2015, Abstract No. BAPS.2015.DFD.L13.11.
- Bossuyt J., Howland M., Meneveau C., Meyers J. (2015). Measuring power output variability and unsteady loading in a micro wind farm model. Windfarms 2015. Leuven, Belgium, 8-10 July 2015.
- Bossuyt J., Charles M., Meyers J. (2014). Measuring wind turbine wakes and unsteady loading in a micro wind farm model: vol. 59 (20). Annual Meeting of the APS Division of Fluid Dynamics. San Francisco, CA, USA, 23-25 November 2014, Abstract No. BAPS.2014.DFD.R26.6.

FACULTY OF ENGINEERING SCIENCE
DEPARTMENT OF MECHANICAL ENGINEERING
TURBULENT FLOW SIMULATION & OPTIMZATION
Celestijnenlaan 300 box 2402
B-3001 Leuven
Juliaan.Bossuyt@kuleuven.be
http://www.mech.kuleuven.be